Simulating Binary Inspirals in a Corotating Spherical Coordinate System

Travis Marshall Garrett

A dissertation submitted to the faculty of the University of North Carolina at Chapel Hill in partial fulfillment of the requirements for the degree of Doctor of Philosophy in the Department of Physics and Astronomy

Chapel Hill
2007

Approved by:

Charles R. Evans

Gerald N. Cecil

Wayne A. Christiansen

Jianping Lu

Y. Jack Ng

Abstract

TRAVIS GARRETT: Simulating Binary Inspirals in a Corotating Spherical Coordinate System
(Under the direction of Charles Evans)

The gravitational waves produced by the inspiral and merger of two black holes are expected to be the first detected by the newly constructed gravitational wave observatories. Accurate theoretical models that describe the generation and shape of these gravitational waves need to be constructed. These theoretical waveforms will aid in the detection of astrophysical wave sources, and will allow us to test general relativity in the strong field regime. Numerical relativity is the leading candidate for constructing accurate waveforms, and in this thesis we develop methods to help advance the field. In particular we use a corotating spherical coordinate system to simulate the evolution of a compact binary system as it produces gravitational radiation. We combine this method with both the Weak Radiation Reaction and Hydro-without-Hydro approximations to produce stable dynamical evolutions. We also utilize Nordström's conformally flat theory of gravitation as a relativistic laboratory during the development process. Additionally we perform semi-analytic calculations to determine the approximate way in which binaries decay in Nordström's theory. We find an excellent agreement between our semi-analytic calculations and the orbital evolutions produced by the code, and thus conclude that these methods form a solid basis for simulating binary inspirals and the gravitational waves they produce in general relativity.

Dedication

To my parents.

CONTENTS

LIST OF FIGURES

Chapter 1

Introduction

1.1 A New Window

Over 90 years have passed since Einstein's original 1916 prediction of gravitational waves [2] [3], and they still have not been directly observed. We will very likely observe them before the 100th anniversary however, thanks to the efforts of an international team of scientists dedicated to detecting these subtle ripples in the fabric of spacetime. The first detection will inaugurate a new field of science and open a new window onto our universe.

The long wait between the prediction and detection of gravitational waves is a reflection of the difficulty of the task. Gravitational waves are very hard to produce: giant, dense concentrations of matter need to be accelerated to very high speeds in order to generate waves of a nontrivial magnitude. Only violent astrophysical systems such as colliding black holes and neutron stars and supernova explosions are powerful enough to generate waves that we could detect. Gravitational wave observation will thus allow us to explore much more deeply into the hearts of these exotic environments, and test some of general relativity's most extreme predictions.

Even within the vast volume of a galaxy these types of events are very rare, which necessitates searching over large clusters of distant galaxies to make detection likely. The resulting faintness of the waves by the time they reach the earth necessitates building very sensitive detectors. The most promising detectors are based on the same apparatus used by Michelson and Morley to disprove the existence of the luminiferous aether. These interferometers split a laser beam in two, and direct the two beams down vacuum tubes several kilometers long. The beams reflect off of mirrors at the ends and recombine to produce an interference pattern. If a gravitational wave passes through the earth it will slightly change the distance that the laser beams travel, and thus change the interference pattern. This change will be very small however, and in general the gravitational wave signal will be buried deep within the noise inevitably produced by the detector. In order to extract the true signal out of the data generated by the interferometers, it is crucial to generate a database of theoretical waveforms. These waveforms will also allow us to compare the detected waves produced by strongly gravitating systems to the predictions of general relativity.

The goal of this thesis is to develop numerical methods that give more accurate theoretical profiles of the gravitational waves produced by a pair of compact bodies spiraling into each other. The core of our method is to use a corotating spherical reference frame to model the crucial late inspiral of a compact binary system. We develop our methods by modeling binary inspirals in Nordström's scalar theory of gravity. We find that our code produces long stable evolutions that match the analytic inspirals that we have calculated for this theory.

In the rest of the introduction we will give an overview of gravitational wave science. We will discuss the physics of gravitational waves, and then examine likely astrophysical sources of gravitational waves, which we hope to detect. This is followed with an overview of the laser interferometers. The next two chapters describe post-Newtonian calculations and numerical relativity. We will primarily develop methods for numerical relativity, and check our results with post-Newtonian analysis. Chapters four and five are the current drafts of our two papers, which contain, respectively, our work on semi-analytic calculations of binary orbit decay in Nordström's theory, and our numerical simulations of this process. The sixth chapter describes the details of the numerical implementation of our methods, and we finish with conclusions.

1.2 Nordström's 2nd Theory

After the Einstein's discovery of special relativity in 1905 it was clear that Newton's theory of gravitation could no longer be absolutely correct. Consider for instance the gravitational field Φ as found from the Poisson equation:

$$\nabla^2\Phi = 4\pi\rho \tag{1.1}$$

If the matter source ρ begins to accelerate then the Newtonian potential Φ instantly responds at all points in space. If true, this would allow for signals to be sent faster than the speed of light, and thus cause a breakdown of causality (although see [4] for an interesting discussion).

A simple solution is suggested by the transition from electrostatics to electrodynamics: let the Laplacian operator change to the d'Alembertian wave operator: $\nabla^2\Phi \to \Box\Phi$. In this case an accelerating source would generate waves that spread out at the speed of light, restoring causality. Additional modifications could then be sought so that the new theory has both relativistic force laws and matches Newton's theory in the appropriate limit. This was the path taken by Gunnar Nordström in 1913 during the development of his 2nd theory of gravitation. Einstein was impressed with the theory, and he and Fokker showed that by using a conformally flat metric $g_{\mu\nu} = \psi^2\eta_{\mu\nu}$ that the main equations could be written in a geometric form:

$$R = 24\pi T \tag{1.2}$$

i.e. the Ricci scalar is equal to the trace of the stress energy tensor. Later Weyl introduced the Weyl curvature tensor $C_{\alpha\beta\gamma\delta}$ which measures how a metric deviates from conformal flatness. Thus

$$C_{\alpha\beta\gamma\delta} = 0. \tag{1.3}$$

can be combined with (1.2) to completely describe the theory.

Nordström's theory is not the one utilized by nature, as it disagrees with many experimental tests: it predicts no bending of light, and it predicts the wrong rate of precession for Mercury. However, we find that it is a very useful theory for building numerical tools to be used in the modeling of binary inspirals in general relativity, as we will describe in this thesis.

1.3 Gravitational Waves

Einstein took a somewhat different path in his search for a relativistic theory of gravitation. Instead of explicitly searching for a wave-like version of Newtonian gravity, Einstein was guided by two theoretical principles towards his famous theory (see e.g. [5]). The first is the principle of equivalence: the acceleration of a body in a gravitational field is independent of the bodies' internal structure. The second is Mach's principle: the structure of spacetime should be influenced by the distribution of matter in it. Einstein used these principles – along with the mathematics of curved manifolds as developed by Riemann, the fact that small local volumes of spacetime should be approximately Lorentzian, and the necessity to match Newtonian gravitation for weak fields – to develop general relativity. In general relativity it is the curvature of spacetime that generates gravitational effects. The curvature is in turn generated by the distribution of mass-energy throughout spacetime as described by the Einstein equations:

$$G_{\mu\nu} = 8\pi T_{\mu\nu} \tag{1.4}$$

While not explicitly founded on the idea of gravitational waves like Nordström's theory, it quickly turned out that general relativity also includes them (although the physicality of the waves was debated for decades - see [6], [7], and for general references on gravity waves see [8], [9], [10]). In order to demonstrate that general relativity contains Newtonian gravitation as a weak field limit, one splits the physical metric $g_{\mu\nu}$ up into a flat background metric $\eta_{\mu\nu}$ and a small perturbation $h_{\mu\nu}$ (with $|h| << 1$ and thus ignoring higher order corrections):

$$g_{\mu\nu} = \eta_{\mu\nu} + h_{\mu\nu} \tag{1.5}$$

One can show that the connection coefficients derived from $h_{\mu\nu}$ lead to the same accelerations as one finds in Newtonian theory. The same perturbation procedure also allows us to investigate gravitational waves (see e.g. [11]). We take equation (1.5) and plug it into the Einstein equation (1.4), and discard terms of order $|h|^2$ and higher to get:

$$\begin{aligned} \partial^\gamma \partial_\mu h_{\nu\gamma} + \partial^\gamma \partial_\nu h_{\mu\gamma} - \partial^\gamma \partial_\gamma h_{\mu\nu} - \partial_\mu \partial_\nu h \\ -\eta_{\mu\nu}(\partial^\gamma \partial^\delta h_{\gamma\delta} - \partial^\gamma \partial_\gamma h) = 16\pi T_{\mu\nu} \end{aligned} \tag{1.6}$$

where the background metric is used to raise indices: $\partial^\mu = \eta^{\mu\gamma}\partial_\gamma$, $h = \eta^{\gamma\delta}h_{\gamma\delta}$. This equation can be simplified by defining:

$$\bar{h}_{\mu\nu} = h_{\mu\nu} - \frac{1}{2}\eta_{\mu\nu}h \tag{1.7}$$

which reduces (1.6) to:

$$\begin{aligned} \partial^\gamma \partial_\mu \bar{h}_{\nu\gamma} + \partial^\gamma \partial_\nu \bar{h}_{\mu\gamma} - \eta_{\mu\nu}\partial^\gamma \partial^\delta h_{\gamma\delta} \\ -\partial^\gamma \partial_\gamma \bar{h}_{\mu\nu} = 16\pi T_{\mu\nu} \end{aligned} \tag{1.8}$$

This is still somewhat complicated but one can show that by choosing an appropriate infinitesimal coordinate transformation ($x^{\mu\prime} = x^\mu + \epsilon^\mu$) that the following gauge choice is possible:

$$\partial^\gamma \bar{h}_{\mu\gamma} = 0 \tag{1.9}$$

This is similar to the Lorentz gauge choice $\partial_\gamma A^\gamma = 0$ used in electrodynamics. This thus reduces (1.8) to:

$$\partial^\gamma \partial_\gamma \bar{h}_{\mu\nu} = -16\pi T_{\mu\nu} \tag{1.10}$$

which includes the vacuum case:

$$\Box \bar{h}_{\mu\nu} = 0 \tag{1.11}$$

As predicted Einstein's theory includes gravitational waves, so that if the source $T_{\mu\nu}$

accelerates waves will propagate out at the speed of light and inform the rest of spacetime.

1.3.1 Weak Gravitational Waves

We will next investigate the properties of the waves given by (1.11). In order to do so consider bodies that are initially both at rest in a local Lorentz reference frame. Position body A at the origin, and body B at a position ξ. We thus want to see how body B moves with respect to A in response to a gravitational wave moving through their volume. To do so we use the equation of geodesic deviation:

$$u^\gamma \nabla_\gamma (u^\delta \nabla_\delta \xi^j) = -R^j_{\alpha\mu\beta} u^\alpha u^\beta \xi^\mu \tag{1.12}$$

To lowest order the 4-velocities of the bodies are $u^0 = 1$ and $u^i = 0$, and we can also set up the position of body B as its initial position plus a small time dependent perturbation: $\xi = \xi_0 + \delta\xi(t)$. Thus equation (1.12) simplifies to:

$$\partial_t^2 \delta\xi^j = -R^j_{0k0} \xi_0^k \tag{1.13}$$

In the previous section we made use of the Lorentz-type gauge condition (1.9) to reduce the equation of motion for the metric perturbation to a wave equation (1.11). We have additional gauge freedom since a further transformation of the type $\partial^\gamma \partial_\gamma \epsilon^\mu = 0$ won't change the validity of (1.9). We can use this to transform the metric perturbation into Transverse-Traceless form $h^{TT}_{\mu\nu}$, which is related to the Riemann tensor via:

$$R_{j0k0} = -\frac{1}{2} \partial_t^2 h^{TT}_{jk} \tag{1.14}$$

We can then integrate (1.13) directly and find that the perturbation in body B's motion as the gravitational wave passes is:

$$\delta\xi^j = \frac{1}{2} h_{jk}^{TT} \xi_0^k \tag{1.15}$$

We note from (1.15) that the amount by which the test body B's position is perturbed (from the vantage point of A) is proportional both to the total separation between A and B and the magnitude of the gravitational wave. This will be important later for the functioning of the interferometers. Furthermore the metric perturbation $h_{\mu\nu}^{TT}$ only distorts spatial distances that are perpendicular to its direction of propagation (transverse), and its trace is zero (traceless) (this is due to the wave equation and gauge choices we have made).

Let the test bodies A and B be oriented in the x-y plane, and let the gravitational wave propagate along the z axis. The only nonzero components are $h_{xx}^{TT} = -h_{yy}^{TT}$ and $h_{xy}^{TT} = h_{yx}^{TT}$, so we have two degrees of freedom, corresponding to two polarizations. Designate the two polarizations by the amplitudes of the waves: $h_+ = |h_{xx}^{TT}|$ and $h_\times = |h_{xy}^{TT}|$. Consider a h_+ polarized wave passing by the test bodies at a point in time. With the phase of the wave currently equal to zero, the x component of the distance will be larger by:

$$\delta\xi^x = \frac{1}{2} h_+ \xi_0^x \tag{1.16}$$

and the y component will be smaller:

$$\delta\xi^y = -\frac{1}{2} h_+ \xi_0^y \tag{1.17}$$

In general a circle of test particles arranged around A will form an oscillating ring, while a $h_\times$ polarized wave will form a similar oscillating ring only rotated by 45 degrees. It is also possible to combine the h_+ and $h_\times$ polarizations to form right handed and left handed circularly polarized waves, as can be done for electromagnetic waves. For instance, consider the waves emitted by a standard binary in quasi-circular orbit. In the plane of the binary the waves will be purely h_+ polarized, while the waves emitted in the polar directions will be purely circularly polarized, with a smooth transition for intermediate angles.

Note also that these two polarizations are the simplest solutions to the vacuum case of equation (1.11):

$$h_{xx}^{TT} = -h_{yy}^{TT} = \mathbb{R}\{h_+ e^{-i\omega(t-z)}\} \tag{1.18}$$

and

$$h_{xy}^{TT} = h_{yx}^{TT} = \mathbb{R}\{h_\times e^{-i\omega(t-z)}\} \tag{1.19}$$

A general solution can be formed from a superposition of these monochromatic waves.

If we consider a rotation of our coordinate system about the z axis through the angle θ we find that the waves in the new coordinates are related to the old by: $h'_+ = h_+ \cos(2\theta) + h_\times \sin(2\theta)$ and $h'_\times = -h_+ \sin(2\theta) + h_\times \cos(2\theta)$. Thus a rotation of 180 degrees gives waves symmetric to the original. This is why quantized gravitational waves would be spin 2 particles, as a spin s wave requires a rotation through an angle of $360/s$ degrees to return it to its original orientation.

1.3.2 Gravitational Waves Traveling Through the Universe

So far the discussion has assumed a flat background. Realistically the waves we will detect will have traveled through a background of other gravitational effects: the gravitational fields of galaxies and dark matter halos, and the overall curvature of the universe. The commonly made analogy is to compare the gravitational waves to water waves traveling over the ocean. At small distance scales the ocean looks flat and the waves propagate much as they would in an infinite flat sea. At a planetary scale however we see the curvature of the earth, which the ocean waves slowly track, perhaps gradually focusing or diverging. Much the same for gravitational waves as they travel from their sources to the solar system.

To make this idea more concrete we can take the overall Riemann tensor which describes the overall gravitational state in the universe, and split it into a curved background and the waves which propagate over it. First take the average of the Riemann tensor, integrating over a distance much longer than the wavelengths of the waves: $|R_{\alpha\beta\delta\gamma}|$. This gives the curvature of the background gravitational fields. The gravitational wave Riemann tensor $R^{(GW)}_{\alpha\beta\delta\gamma}$ is then the difference between the overall Riemann tensor and its average:

$$R^{(GW)}_{\alpha\beta\delta\gamma} = R_{\alpha\beta\delta\gamma} - |R_{\alpha\beta\delta\gamma}| \tag{1.20}$$

This is a valid procedure in our universe, where the curvature of the waves $h/\lambda^2 \sim 10^{-22}/(10^9 cm)^2$ is much greater than the curvature of the universe: $\sim 1/10^{56} cm^2$.

The wave equation then also needs to include covariant derivatives that are with respect only to the background curvature (as signified with a | instead of ;):

$$\bar{h}_{\mu\nu|\gamma}{}^{\gamma} = 0 \tag{1.21}$$

Higher order terms are also needed for completeness, although they are usually very small for realistic situations and can be dropped. The waves can thus be considered perturbations about the background curvature.

Suppose that the waves have traveled far enough from their source to be approximately planar. This then allows for the eikonal or geometric optics approximation to be made. Using the previous arguments the wave can be put in the form:

$$h_{\alpha\beta} = Re[A_{\alpha\beta} e^{i\phi}] \tag{1.22}$$

where $\phi = \omega(z-t)$, $\phi_{|\mu} = k_\mu$, and ${h_{\alpha\beta}}^{|\beta} \rightarrow A_{\alpha\beta}k^\beta = 0$, that is the waves are transverse, the propagation vector is null $k_\beta k^\beta = 0$ and the waves are parallel propagated along null geodesics $A_{\alpha\beta|\mu}k^\mu = 0$. Since the waves propagate along null geodesics of the background curvature, they can undergo gravitational lensing and redshifting, in the same way as electromagnetic waves do.

1.3.3 Generation of Weak Gravitational Waves

We will now consider the generation of gravitational waves by sources that have negligible self gravity. The negligible self gravity stipulation allows us to use equation (1.10), as the first order perturbative expansion will not be sufficient for sources with appreciable self gravity. It turns out, as we will see later, that sources with strong gravitational self fields give rise to similar waves. The Green's function solution to (1.10) is:

$$\bar{h}_{\mu\nu}(t,x) = 4\int \frac{T_{\mu\nu}(t-|x-x'|,x')}{|x-x'|}d^3x' \tag{1.23}$$

This will generally not be in the transverse traceless gauge, but it can be subsequently cast into it by only keeping the components of h perpendicular to the direction of propagation and subtracting off the trace.

Several more assumptions are made to reduce this to a useful expression. Generally we are interested in the waves far from their source, and thus the $|x-x'|$ term in the denominator of (4.46) can be approximated by r, the distance from the measurement point to the center of the wave source, and shifted outside the integral. We can furthermore show that T^{jk} can be transformed (by using integration by parts and ${T^{\mu\nu}}_{,\nu} = 0$) into ${T^{00}}_{,00}x^jx^k$, which transforms (4.46) to:

$$h^{TT}_{jk} = \left[\frac{4}{r}\partial_t^2\int T^{00}x^{j\prime}x^{k\prime}d^3x'\right]^{TT} \tag{1.24}$$

The waves are thus proportional to the second time derivative of the quadrupole moment of the mass-energy T^{00} (to leading order).

When it is necessary to include sources with appreciable self-gravity (as will usually be the case), then it will be useful to construct a pseudotensor $\tau^{\mu\nu}$ such that $(T^{\mu\nu} + \tau^{\mu\nu})_{,\nu} = 0$ [12]. This allows us to construct:

$$\bar{h}_{\mu\nu}(t, x) = 4 \int \frac{(T_{\mu\nu} + \tau_{\mu\nu})^{ret}}{|x - x'|} d^3x' \tag{1.25}$$

and we can proceed as before, under suitable restrictive assumptions. This procedure will be considered in more detail in the post-Newtonian methods chapter.

1.4 Astrophysical Sources

With the general characteristics of gravitational waves now in hand, we next consider the possible astrophysical sources that we may hear with the new observatories (note that we will often use "hear" in place of "detect" as in many ways gravitational waves are analogous to sound waves, thus complementing the electromagnetic light that we see – see e.g. [13], and for more source overviews see [1] and [14]). There is a wide variety of possible sources, but the most likely to be initially detected are pairs of compact bodies in tightly bound orbits, so we will focus in this section on these objects. Rapidly evolving Neutron Star (NS) and Black Hole (BH) binaries are the most likely candidates to be heard first by the ground based detectors and slowly evolving White Dwarf (WD) binaries are all but guaranteed to be detected by a space based detector (see [15] for detailed descriptions of these objects). These binaries have very small separations and have orbital velocities that are a substantial percentage of the speed of light, and are thus producing copious gravitational waves. The energy and angular momentum carried away by the waves causes the binary system to decay until the compact bodies merge in a final burst of gravitational radiation.

The tight NS and BH binaries are expected to be very rare however, so we need to do a careful analysis to see if it is reasonable to expect that we will hear any waves from these systems during the lifetime of operation of the detectors. We thus need to combine astronomical observations and theoretical considerations to form models that describe how galaxies are populated with different types of star systems.

1.4.1 Stellar Populations

To begin the description we zoom all the way out to the beginning of the universe. Several hundred thousand years after the big bang the universe had cooled sufficiently for the protons and electrons to combine and form a neutral hydrogen gas, thus releasing the photons that had previously been trapped within the plasma. These photons have traveled freely since then, and have now appear to us as microwave radiation, having since been redshifted by about a factor of thousand. This gives us the Cosmic Microwave Background (CMB), as originally discovered by Penzias and Wilson [16], [17].

Recent geometric investigations of the slight inhomogeneities in the CMB show that the universe is very nearly flat and thus the average density of the universe is very close to the critical value of $\rho_{crit} = 1.17 \times 10^{11} M_{\odot}/Mpc^3$. The inhomogeneities were at level of one part in 10^5 during the formation of CMB, and went on to seed the birth of galaxies and star formation as the universe expanded. Only a small percentage of the mass energy in the universe is contained in stars. Some 70 percent in the current epoch takes the form of dark energy, and another 27.5 percent is contained in dark matter, leaving only 2.5 percent in "regular" baryonic matter. Only 10 percent of the baryonic matter is contained in stars, the rest is gas. This leaves a density of stars in the universe of approximately:

$$\rho_{crit} = 2.9 \times 10^8 M_{\odot}/Mpc^3 \tag{1.26}$$

We then need to estimate the fraction of these stars that are the compact bodies we are interested in. First we need to know the rate at which stars of different masses are produced. The current overall Star Formation Rate (SFR) is estimated to be about one solar mass star per year in a 100 cubic Megaparsec volume [18]:

$$SFR = 0.013^{+0.007}_{-0.005} \frac{M_\odot}{yr Mpc^3} \tag{1.27}$$

(note that this is averaged over large enough volumes such the universe is homogeneous). The current SFR is lower now than it has been in the past. Since star formation began after the big bang it has been decreasing in rate roughly exponentially:

$$SFR \propto e^{-t/\tau} \tag{1.28}$$

where $\tau = 6$ Gyr [19].

With the rate star formation in hand, we now need to know the Initial Mass Function, which gives the fraction of stars formed at a particular mass [20], [21]. Fitting to observational data gives the fraction of stars $\xi(m)$ within dm of mass m as:

$$\xi(m)dm = \frac{SFR(M_\odot yr^{-1})}{0.92 M_\odot^2} \times (M/0.5M_\odot)^{-1.3} \tag{1.29}$$

for $M < 0.5M_\odot$ and

$$\xi(m)dm = \frac{SFR(M_\odot yr^{-1})}{0.92 M_\odot^2} \times (M/0.5M_\odot)^{-2.3} \tag{1.30}$$

for $M > 0.5M_\odot$. Thus most stars produced are less massive than the sun.

We next need to consider stellar evolution as a function of mass, as this determines which stars evolve into the compact bodies we are interested in, and also provides a mechanism to draw the compact bodies into tight enough orbits such that they produce gravitational waves that could be detected. The luminosity L of a star with mass M is approximately:

$$L \simeq L_\odot \left(\frac{M}{M_\odot}\right)^{3.5} \tag{1.31}$$

This reflects that stars more massive than the sun consume their fuel at a much more rapid rate. In a hot dense plasma only nucleons in the upper tail of the thermodynamic distribution will have sufficient kinetic energy to overcome the electrostatic potential and fuse. The fusion rate is increased by quantum tunneling, which is exponentially suppressed by the magnitude of the potential barrier being tunneled through. These effects combine to give the steepness in equation (1.31). The rapidity of burning determines an approximate life span T_{MS} for main sequence stars as a function of their mass:

$$T_{MS} \simeq 13 \times 10^9 \left(\frac{M}{M_\odot}\right)^{-2.5} yr \tag{1.32}$$

Among all the stars that have been born since the big bang, those less massive than the sun are almost all still on the main sequence, while most of those more than about $2M_\odot$ have completed their life cycle and are now either a WD, NS, or BH. We can thus compute that out of the density of stars in the universe (1.26), about 76 percent are luminous main sequence stars, and the rest are compact remnants, with about 18 percent white dwarfs, 2 percent in neutron stars, and the final 3 percent in black holes.

1.4.2 Stellar Evolution

As a main sequence star with mass $M \gtrsim M_\odot$ ages it burns through the supply of hydrogen in its core, leaving helium behind. At first it is not yet hot enough to burn the remaining helium, so energy production and the thermal pressure in the core decrease and the core shrinks, while hydrogen burning migrates to a shell outside of the core. The denser conditions leads to a greater rate of burning, greatly increasing the luminosity of the star, and expanding the outer radius into the range of an astronomical unit. This is the red giant phase of a star, with examples ranging from the approximately solar mass Arcturus to the $\sim 15M_{\odot}$ Antares. This late phase of the star's evolution will turn out to be very important later, as it can lead to mass transfer in a binary star system, and a corresponding decrease in the binary separation.

The final fate of the star as it evolves through the red giant stage depends on the mass of the star. For stars less than about $2.5M_{\odot}$ the helium in the core is held up mainly by degeneracy pressure. Thus as the star burns more hydrogen in the outer shell, and the temperature rises to 3×10^8K, the helium can burn explosively in a process known as the helium flash (which generally does not release enough energy to blow apart the star). In heavier stars the helium core is supported by thermal pressure and begins burning more smoothly. As the helium burning in the center finishes, leaving behind carbon and oxygen, and begins to burn helium in outer shells the star enters the Asymptotic Giant Branch (AGB). Stars less than about $8M_{\odot}$ will not go on to burn the carbon and oxygen in their cores, and instead blow off a large percentage of their mass, producing a planetary nebula and leaving behind a carbon-oxygen WD. For stars that are between $8M_{\odot}$ and $10M_{\odot}$ the carbon-oxygen core can detonate in a manner similar to the helium flash, but it is not clear at this time whether this will blow the star apart or not.

For stars greater than about $10M_{\odot}$ the carbon-oxygen core will burn non-explosively, and will continue to fuse elements in successive shells leading to iron. Fusion of iron and higher elements is now endothermic as opposed to exothermic, so a mass of iron plasma builds in the core, supported by electron degeneracy pressure. When the energy level of the electrons becomes relativistic the equation of state changes and degeneracy pressure can no longer keep the core from collapsing. The collapse squeezes electrons into protons forming neutrons, which then produce neutron degeneracy pressure which halts the collapse. This forms a neutron star at the center of the star. Neutrinos carry away most of the gravitational potential energy, and a small percentage of these interact with the rest of the star, blowing it apart in a type II supernova. A classic example is supernova SN1054, which left the Crab Nebula and a pulsar behind. A problem with supernovae, in terms of producing binary NS systems, is that the supernova explosion generally ejects the new neutron star at considerable speed. This is due to asymmetry in the collapse process, as an asymmetry of 1 percent would be sufficient to explain the neutron star kicks that are observed. This will generally disrupt a binary system, and perhaps only one in a hundred neutron stars will remain in a binary system after a supernova.

If the star is massive enough, around $M > 25M_\odot$ then the core collapse is too massive to be halted by the formation of a neutron star, and it collapses directly into a black hole. A massive accretion disk can then form around the new black hole, producing polar jets that punch through the star. These are hypernovae, and are leading candidates as the causes of long duration Gamma Ray Bursts (GRBs).

These processes give us compact bodies that can produce loud gravitational waves, but they furthermore need to be produced in tight binary orbits, with separations on the order of a light second, so that gravitational radiation can then cause them to spiral in and merge within the age of the universe. Binary star systems are very common, accounting for perhaps half of all the stars in a galaxy. Their Keplerian parameters are log-normal distributed, so that binary systems with separations of one AU and 10 AU have the same probability of being formed.

The red-giant phase of stellar evolution, discussed earlier, then provides a mechanism to tighten the orbits of binaries. When one star in a binary swells its outer layers can pass beyond its Roche lobe, and thus begin to accrete on the other star [22] [23]. A famous system is Algol [24], where the more massive star in a binary system is not as far along in its evolution as its companion, which has entered the subgiant stage. As the stars would have formed at the same time, this is explained by the subgiant star having formerly been the most massive, but then having transferred much of its mass to its companion upon expansion. Another famous example is Cygnus X-1 [25] [26], where an O-B supergiant is feeding the accretion disk of its black hole companion, and producing bright X-rays. Supernova explosions are another possible result of accretion processes: if a white dwarf accretes enough matter from a red giant companion to reach the Chandrasekhar mass, it will usually detonate the carbon and oxygen in a type Ia supernova, as in supernova SN1572 [27].

The transfer of material from one star in a binary to the other via the Roche lobe can also cause the binary stars to spiral into each other. For instance it is thought that AM CVn binaries (see e.g. [28], [29],[30]) are the product of several cycles of accretion and inspirals, resulting in a tight enough orbit to emit gravitational waves (GWs) observable by LISA. It is thus an important pathway to bring binaries close enough together so that gravitational radiation can then cause an inspiral and merger within the lifetime of the universe (generally NS-NS need to have separations on the order of the radius of the sun in order to spiral in quickly enough).

1.4.3 Expected Compact Binary Detection Rates

In order to estimate the number of sources that the interferometers can be expected to hear, all of these factors can be combined in massive Monte Carlo simulations of millions of binary systems in order to see what percentage evolve into the tight compact binaries we need. For detection purposes we also need to consider the amplitude and the frequency of the waves produced. The amplitude is crucial as this determines the volume of space in which we would be able to detect the GW source. The frequency is likewise crucial as the detectors are only sensitive to GWs within a certain bandwidth. Compiling the theoretical models and observational data we find the following expected detection rates for NS-NS, NS-BH, and BH-BH binaries:

- NS-NS: By modifying the inspiral calculations that we will perform later in the post-Newtonian calculations, we can show that the amount of time t_{merge} that a binary has left before it merges can be related to the binary's frequency and the rate of change of the frequency: $t_{merge} \propto f/\dot{f}$. We thus hear about the last 3 minutes of a NS-NS inspiral in LIGO. We thus need to estimate the rate at which NS binaries are entering the final phase of their inspirals in the local region of the universe.

Neutron star binaries are the systems we have the best observational data for. In 1974 Hulse and Taylor discovered the pulsar in PSR1913+16 which was determined to be orbiting another neutron star (see e.g. [31]). The binary was tight enough that the orbital parameters could be observed to evolve over the years due to the emission of gravitational radiation, in precise agreement with the predictions of general relativity. PSR1913+16 has about 300 millions years until the stars merge and their waves enter the LIGO frequency band. Since this discovery several other binary pulsar systems have been located. Compiling the observational data, Phinney derived an expected NS-NS merger rate of 10^{-6} per year in the Milky Way [32], which subsequent studies have tended to reproduce. However the recent discoveries of new binary pulsar systems, including PSR J0737-3039 in which both neutron stars are pulsars and which has only 80 million years left until merger, somewhat increases the expected merger rate: [33], [34].

LIGO I is sensitive enough to detect GWs from NS-NS binaries out to about 20 Mpc. In order to extrapolate the expected NS-NS merger rate in the Milky Way to other galaxies, we observe their brightness in the blue-light bands as this light is produced by the massive, short lived stars that can evolve into NS-NS systems. Compiling the models from pessimistic to optimistic we get merger rates of 0.001 to 1 per year. Advanced LIGO will be able to see out to 300 Mpc, which will boost the detection rate by about a factor of 1000.

In addition to the binary pulsar systems that have been directly discovered, it is also suggested that short gamma ray bursts (GRB) may be due to the merger of binary neutron star systems: [35], [36], [37]. If true this information could affect the expected hit rate. However, alternative hypotheses are offered for the progenitors of short GRBs - for instance they may also originate from erupting magnetic fields on neutron stars: [38].

- NS-BH: Unlike binary NS systems there are currently no known NS-BH binaries in the Milky Way, (although there are examples of systems such as Cygnus X-1 that have the potential to evolve into one). It is possible however that some of the gamma ray bursts detected at large distances are due to NS-BH systems where the NS has grown close enough to the BH to be tidally disrupted, thus forming an accretion ring about the BH and generating relativistic polar jets. In general the uncertainty in merger rate is greater, and plausible estimates need to rely much more on population synthesis models. Initial LIGO will be able to see these systems out to about 40 Mpc, and the estimated detection rate is similar to that for NS-NS systems – somewhere from 0.001 to 1 events per year. As before, LIGO II will observe over a thousand times the volume, and the hit rate will go up accordingly.

- BH-BH: As with NS-BH binaries, there are no known $\sim 10 M_{\odot}$ black holes binaries, and we need to use population synthesis studies to give expected formation rates. While these studies suggest that the rate of formation of these per galaxy is lower than NS-NS binaries, they can be heard out to about 100 Mpc with LIGO I, and thus are the most likely systems to be first detected, with event rates estimates ranging from 0.05 to 1 a year [39] .

  In addition to black holes binaries that have been formed in the main body of galaxies, solar mass black holes can also be produced in globular clusters.

Globular Clusters are old, dense groups of stars – sometimes 10^6 stars within a radius of 10 pc – that are found orbiting many galaxies including our own. Due to the density of stars, there is considerable interaction between the stars, and in general heavier objects like black holes will migrate towards the centers of the globular clusters, where further interactions can cause black hole binaries to form that are tight enough to merge within the lifetime of the universe. Statistical models of these systems indicate that observable mergers of these cluster black holes may occur at the same rate as those in the galactic field [39].

1.4.4 Other Gravitational Wave Sources

In addition to neutron star and black holes binaries (which are the first objects we expect ground based detectors to hear) there are other interesting possible systems that we may detect. We will likely have to wait for advanced LIGO or LISA (depending on the frequencies in which they radiate) to hear them. For instance there are so many tight WD-WD binaries in the Milky Way that their waves will combine to form a region of noise within a section of LISA's sensitive range (see e.g. [40]). We might also hear a neutron star - white dwarf binary like J141-6545 NS-WD which has a pulsar that is one million years old (indicating a reasonably high formation rate). Simulations of the evolutions of NS-WD systems like these can be found in [41]. On the other hand we can have extremely massive binaries: LISA may hear the gravitational waves produced by the inspiral of supermassive black hole binaries. These are expected to be quite rare, but we can essentially hear them across the visible universe. Successive mergers are also a possible formation pathway for the creation of these massive black holes (see e.g. [42]).

Gravitational waves from objects other than binaries are also possible: supernovae and hypernovae can also produce strong gravitational waves if the collapse process is asymmetric – see [43], [44] for instance. Rapidly rotating neutron stars that have small "mountains" in their crust are another possible detectable source. The very strong gravitational fields on the surface will act to flatten the mountains, but there are plausible scenarios where they could still be produced. For instance they could be created if the neutron star accretes material from a companion on a different axis than it is revolving on, or is heated nonuniformly. Low Mass X-ray Binaries (LMXB) give an example of this, and LIGO 2 will be able to adapt its sensitivity profile to search for the waves from these objects: [45], [46]. Another interesting possible source is the stochastic GW background created during the big bang – see [47] for instance. Perhaps the most exciting possibility is that we will discover waves from a new, surprising source, as has often happened in the past when we have opened new windows onto the universe.

1.5 Interferometers

The age of experimental gravitational wave science began with Weber and the construction of resonant bar detectors [48]. Centered around large rods of metal, these detectors are designed so that a passing gravitational wave of the right frequency will stimulate a harmonic vibration in the rod. Weber believed that he detected the presence of gravitational waves, although this was later attributed to noise. The best current resonant bar detectors have sensitivities of about $h \sim 4 \times 10^{-19}$ [49], although they are only sensitive in a small frequency band.

Modern GW detector design is based on interferometry (see [50], [51] for overviews). Weiss showed 1972 that it should be possible to construct a laser interferometer that is sensitive enough to detect the distortions in space-time due to a gravitational wave passing through the earth [52]. Later in the 70s Forward built the first prototypes [53], with sensitivities of about $h \sim 10^{-16}$. Research since then has resulted in the current batch of large ground based detectors: LIGO [54], VIRGO [55], GEO600 [56], TAMA300 [57], which have sensitivities of about $h \sim 10^{-22}$, thus making the detection of gravitational waves plausible. Advanced LIGO [58] will increase the sensitivity to $h \sim 10^{-23}$, which will then make detection quite likely. Plots of the sensitivity as a function of frequency for both LIGO I and LIGO II, along with the gravitational wave signatures of some standard sources, is given in figure (1.2) The space based detector LISA [59] is being planned which will operate at a lower frequency band than the ground based detectors, and is also quite likely to detect GWs. A plot of LISA's sensitivity profile and some standard sources is given in figure (1.3).

A general schematic of a laser interferometer is given in figure (1.1). A laser beam is produced by the laser at (L) and passes through a Power Recycler (PR) to the Beam Splitter (BS), which splits the beam into two. These two beams then travel down orthogonal vacuum tube arms A1 and A2, reflect off of the mirrors M12 and M22 at ends of each, and are then recombined at the PhotoDetector (PD). The laser beams combine to form an interference pattern at (PD), and thus if a GW passes through the detector it will slightly change the arm lengths A1 and A2 and thus perturb the interference pattern. The trick is to then sufficiently reduce the noise in the detector so that perturbations in spacetime of the order $h \sim 10^{-22}$ can be detected.

There many sources of noise in laser interferometers, but here we will only discuss a few of the primary ones. Ground based detectors are most sensitive to waves in the 50 to 500 Hz range. The main source of error in the higher frequency range is the inherent quantum fuzziness in the laser light, referred to as "shot noise", while sensitivity at lower frequencies is limited by vibrations in the earth.

1.5.1 Detector Reference Frames

Consider a laser beam that travels a distance L between mirrors in an interferometer. We want to calculate the phase shift in the beam due to a passing GW with amplitude $h \sim 10^{-22}$ and wavelength λ. First we need to consider the reference frame

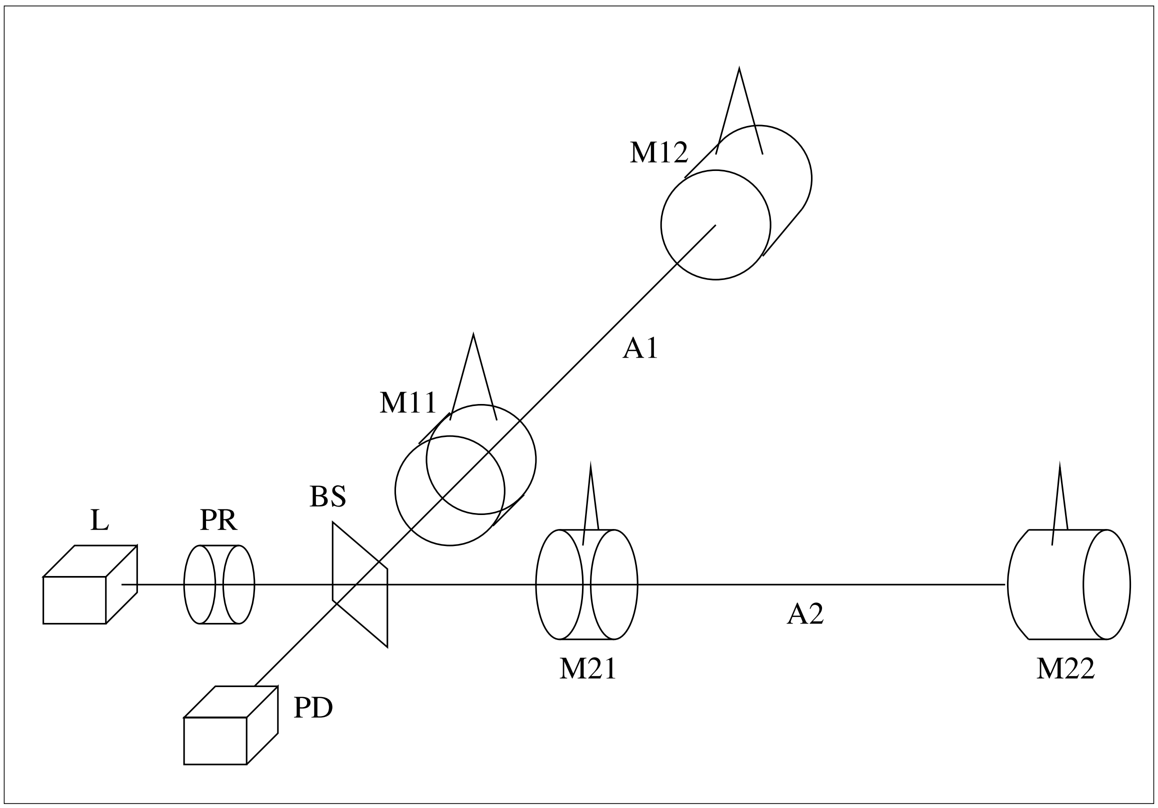

Figure 1.1: Interferometer Layout. L : Laser , PR: Power Recycler, BS: Beam Splitter, PD: Photo-Detector, M11-A1-M12: Mirror 1 and 2 on arm A1, M21-A2-M22: Mirror 1 and 2 on arm A2

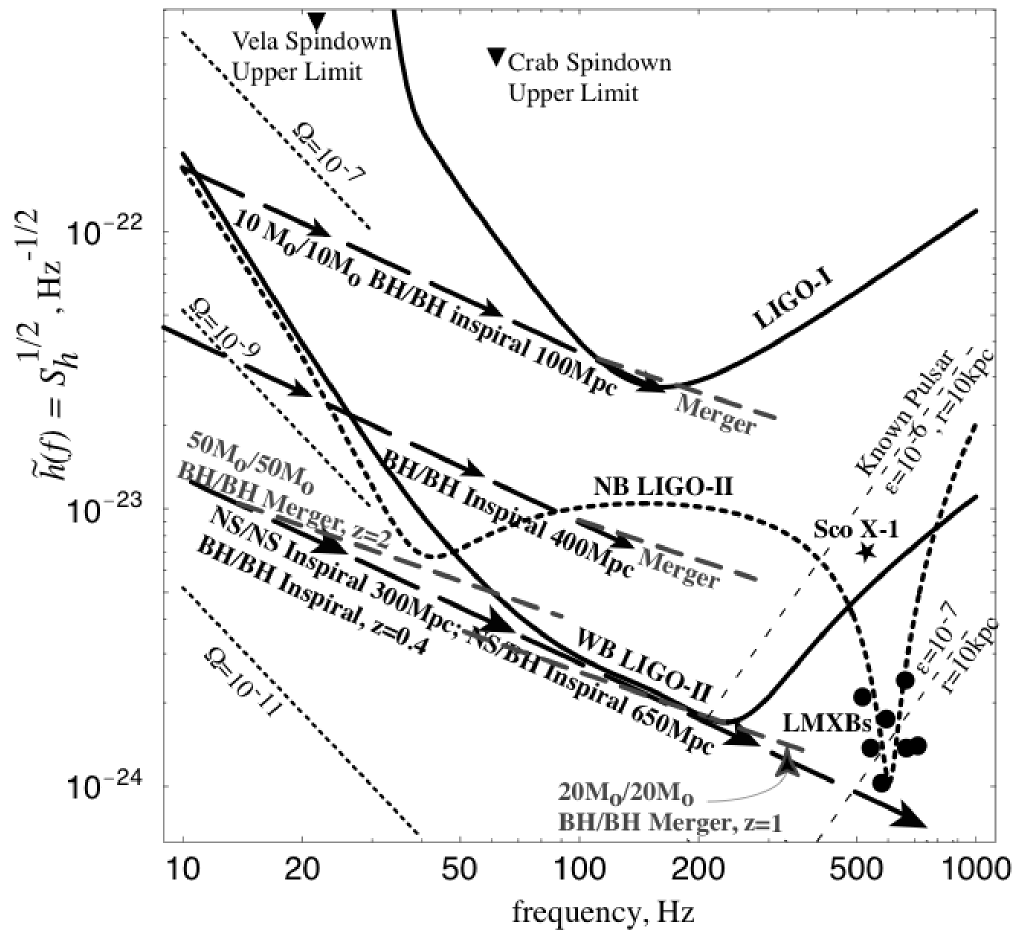

Figure 1.2: LIGO I and II frequency profiles (from [1])

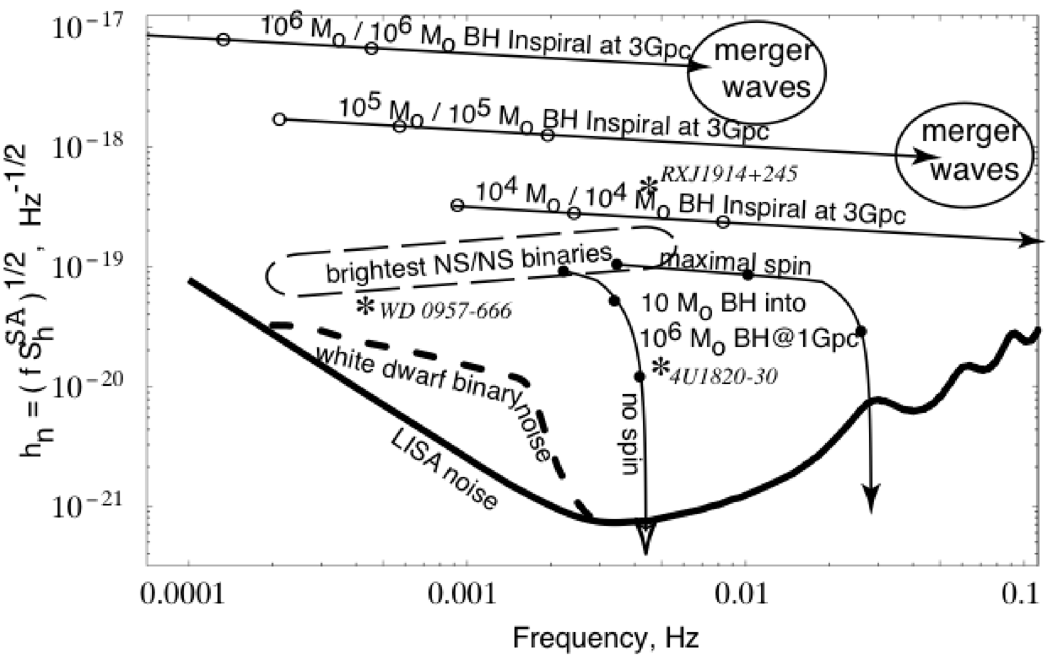

Figure 1.3: LISA frequency profiles (from [1])

that we will base our measurements in. In the Local Lorentz Frame (LLF) gauge the metric is equal to the flat space metric $\eta_{\alpha\beta}$ plus corrections that are on order of the Riemann tensor $|R_{\mu\nu\delta\gamma}|$ times the square of the displacement from the origin L. The Riemann tensor in turn is proportional to the amplitude of the gravitational waves divided by the square of their wavelength. We thus find:

$$g_{\alpha\beta} = \eta_{\alpha\beta} + \mathcal{O}(|R_{\mu\nu\delta\gamma}|L^2) = \eta_{\alpha\beta} + \left(\frac{L}{\lambda}\right)^2 h \tag{1.33}$$

This forms a simple coordinate system to work in, as many of the subtleties of general relativity can be ignored. Note that the ground based detectors are not in Lorentz frames however, since they remain stationary with respect to the ground instead of being in free fall. We thus need to accelerate the LLF by g, giving us the Proper Reference Frame of the interferometer. An example metric would be:

$$ds^2 = -(1 + 2gz)dt^2 + (1 + h_+(t - x))dx^2 + (1 - h_+(t - x))dy^2 + dz^2 \tag{1.34}$$

for h_+ polarized GWs propagating perpendicular to the surface of the earth.

Note also that the LLF gauge is only valid for distances less than the length of the gravitational wave: $L < \lambda$, as the approximation does not converge for larger distances. This is a valid approximation for LIGO where the gravity waves are several thousand kilometers long, but not for LISA. For LISA the calculations need to be done in the Transverse Traceless (TT) gauge, which converges globally for weak waves:

$$g_{\alpha\beta} = \eta_{\alpha\beta} + h^{TT}_{\alpha\beta} \tag{1.35}$$

In the TT gauge the distance L does not change at lowest order – instead the laser beam is modified by the metric perturbation as it propagates, resulting in the same phase shift as the LLF gauge when it is valid.

1.5.2 The Shot Noise Limit

Choosing an appropriate reference frame, we re-derive equation (1.15), and find that the change ΔL in the length L of one of the interferometer arms is:

$$\Delta L \sim hL \tag{1.36}$$

The change in length of $+\Delta L$ in one arm and $-\Delta L$ in the other combine to give a total phase shift of

$$\Delta\phi = \frac{4\pi L h}{\lambda_e} \tag{1.37}$$

at the photodetector (PD), where λ_e is the wavelength of the laser light used. In order to make the phase shift as large as possible, we would like to set the length of the arm equal to the wave length of the gravitational wave $L \sim \lambda$, but the ground based detectors have arms several kilometers long, while the gravitational waves have wavelengths from about 10^3 to 10^4 km. To make up for this the beams are reflected back and forth several hundred times along the arms before being recombined to form the interference pattern. In figure (1.1) this is accomplished by constructing Fabry-Perot cavities between mirrors $M11$ and $M12$ on arm $A1$ and likewise between mirrors $M21$ and $M22$ on arm $A2$. With a number of bounces B the total phase shift becomes:

$$\Delta\phi = \frac{4\pi BLh}{\lambda_e} \tag{1.38}$$

The laser light used is in the visible spectrum, so the phase shift is about $\Delta\phi \sim 10^{-9}$.

We thus need to see if it is possible to distinguish phase shifts of this magnitude with a laser. We find that there is an upper bound to the accuracy given by quantum mechanical uncertainty relations. While not as simple to derive as the position-momentum uncertainty relation, one can generally show that the uncertainty in energy and time in a system follow $\Delta t\Delta E \gtrsim \hbar$. The uncertainty in the measurement time is related to the uncertainty in the phase by $\omega_e\Delta t = \Delta\phi$, where ω_e is the frequency of the laser light.

The energy collected is equal to the energy of each photon $\omega_e\hbar$ times the total number collected N_γ where the collection time is half the period of the gravitational wave $T_{GW}/2 = 1/(2f)$ with frequencies of about $f \sim 100$ Hz. For a coherent light source like a laser, the uncertainty in the number of photons is equal to its square root: $\Delta N_\gamma = \sqrt{N_\gamma}$ – this is the shot noise. This gives an uncertainty in the energy: $\Delta E = \Delta N_\gamma \hbar\omega_e$, and thus the uncertainty in the phase is related to the number of photons received (per half period T_{GW}):

$$\Delta\phi \gtrsim \frac{1}{\sqrt{N_\gamma}} \tag{1.39}$$

For phase uncertainty of about $\Delta\phi \sim 10^{-9}$, this corresponds to about $10^{18}N_\gamma$ per T_{GW}. For lasers emitting in the visible spectrum this corresponds to about 100 watts of power, which has been difficult to achieve with high accuracy lasers such as

Nd:YAG. A work around is to design the interferometer such that the photodetector sits at an interference minimum, and thus most of the laser light leaving the arms heads back towards the laser. We then place a power recycler (PR in figure (1.1)) between the laser and the beam splitter which reflects this light back into the arms (see e.g. [60], which also covers laser frequency stabilization). This multiplies the total laser power, so that a 5 watt laser gives rise to a 100 watt beam in the arms, sufficient to detect GWs at the desired accuracy. We also note that the shot noise increases as gravitational wave frequency increases, and thus higher power lasers are needed to increase the sensitivity to high frequency waves.

The upper limit imposed by shot noise is theoretical in nature (although see [61], [62]), and a lot of careful interferometer design is needed to saturate that bound. We discuss briefly a few additional aspects of the design here.

1.5.3 Gaussian Beams

We mentioned earlier that Fabry-Perot cavities are used to bounce the laser beam down the arms several hundred times, thus greatly increasing the effective arm length and sensitivity. In general the laser beam will diffract as it propagates, and without careful control almost all of the laser beam power would be lost into the side walls of the arms after hundreds of reflections. By careful consideration of the way in which the light diffracts we can control the beam so that it maintains the same shape after each reflection, so that all of the power is available to reveal phase shifts. This is done by the use of Gaussian wave profiles.

Let the beam propagate in the $\hat{z}$ direction of an arm. We thus want to minimize the size of the beam in the transverse $\hat{y}$ and $\hat{x}$ directions. An uncertainty relation gives us $\Delta p_y \gtrsim \hbar/(2\Delta y)$. A Gaussian beam satisfies the equality, and thus spreads as little as possible. Additionally the phase fronts are spherical, so if we construct spherical mirrors at either end of the cavity with the same curvature then the beam will be reflected back in such a way that it preserves its shape. The beam has a thin waist shape, with the smallest spread halfway down the arm length, and symmetric spherical wave fronts expanding off to each side.

We give a few more of the mathematical properties of Gaussian waves here. Again situate the beam such that it propagates in the z direction (with the $z = 0$ at the halfway point in the arm and the mirrors at $z = \pm L/2$), with the electric and magnetic fields oscillating in the transverse directions: say $E_x(t-z)$ and $B_y(t-z)$ for a polarized wave. Using ψ as a shorthand for the electromagnetic fields: $\psi(t-z) = E_x(t-z)$, so we have $\Box\psi = 0$. The Gaussian solution to this is:

$$\psi_{z=0} = e^{-\bar{\omega}^2/\sigma_0^2} \tag{1.40}$$

with $\bar{\omega} = \sqrt{x^2 + y^2}$, so that σ_0 is the radius by which ψ falls off by $1/e$. Going a distance z down the arm (in either direction) and the spread in the beam increases to $\sigma_z = \sigma_0(1 + z^2/z_0^2)^{1/2}$ with z_0 being the characteristic distance such that $\sigma_z = \sqrt{2}\sigma_0$. We can find that the beam spreads out at an angle $\beta = \lambda_e/(\pi\sigma_0)$, and thus solve for $z_0 = \pi\sigma_0^2/\lambda_e$. A small waist gives rise to a lot of spread on either end, and a large waist only has a small amount of spread, but starts off large. We can optimize and thus get the minimal size for the mirrors at each end: $\sigma_{min} = \sqrt{2}\sigma_0 = \sqrt{(L\lambda_e/\pi)}$. The radius of curvature is $R = z + (\pi\sigma_0^2/\lambda_e)/z$ which determines the processing of the mirrors to preserve the beam shape. Many additional adjustments are needed to fine tune and stabilize the geometry of the beam, such as the use of mode cleaning cavities – see [63] for more.

1.5.4 Additional Noise Considerations

There are many additional technical issues to address and noise sources to minimize in the building a laser interferometer. A primary source of noise is seismic vibrations (see [64], [65]), which are the dominant road block at the low frequency end of the spectrum. These vibrations need to be dampened substantially for the interferometer to work. Another primary source is thermal noise that exists within the components of the interferometer itself: noise from the pendulum oscillations of the suspended mirrors and other components, the violin-like vibrations in the suspension wires, and the internal normal modes of the mirrors themselves (see e.g. [66], [67], [68]). The thermal motions of the constituent atoms themselves is much larger than the variation in path length due to the GW, but the statistical average of their motion makes this manageable.

To minimize thermal noise we need to know its spectral shape. The power spectral density of thermal motion at a particular wavelength ω is given in terms of the resonant frequency ω_0, temperature T and the intrinsic loss $\phi(\omega)$:

$$\tilde{x}^2(\omega) = \frac{4k_B T\omega_0^2\phi(\omega)}{\omega m[(\omega_0^2 - \omega^2)^2 + \omega_0^4\phi(\omega)^2]} \tag{1.41}$$

(see e.g. [69]). We see that here is a large peak around the resonant frequency, so we want to construct the detector such that ω_0 is very different from the frequencies the interferometer is interested in. We also want to choose materials with a small intrinsic loss $\phi(\omega)$. This is only one quality that the mirrors need – in addition they need to be super-polishable (to within an angstrom) have low absorption losses (otherwise the beam power will be seriously reduced after several hundred reflections), and have low refractive index variations (if the laser beam passes through them). High-quality synthetic fused silica products are available that meet these needs.

We additionally need to eliminate seismic noise as much as possible. We do this by designing the pendulum suspension systems such that their lowest order harmonic f_0 is widely removed from the gravitational wave frequencies f. This gives an isolation factor of f_0^2/f^2 for $f > f_0$: such that seismic noise at 100 Hz is reduced by a factor of 10^4 for $f_0 = 1$Hz. These can then be stacked successively to get the noise down to required level. Additional subtleties arise since the arm lengths are long enough such that the suspended systems at either end are not quite parallel, but rather both point towards the center of the Earth. This necessitates vertical stabilization as well. LIGO I uses a four stage isolation stack to reach its target sensitivity. LIGO II will increase the number of isolation stacks to improve sensitivity at low frequencies, it will use more expensive materials to reduce thermal vibrations, and it will use a higher power laser to increase sensitivity at high frequencies.

1.5.5 Signal Extraction with Matched Filters

Despite the sensitivity of the interferometers that have now been built, the amplitudes of gravitational waves from plausible astrophysical sources are so faint that the waveforms will still generally be buried in the noise. However we can extract the signal from the noise by the use of matched filters. The matched filter is based on an expected waveform template $u(t)$, which is divided through by a spectral profile of the interferometer's noise distribution $S_h(f)$. We take the inner product $\langle h, u\rangle$ of the template $u(t)$ and interferometer data $h(t) = n(t) + A \times s(t)$ where $n(t)$ is the noise and the signal is given by an overall amplitude A and waveform $s(t)$ (note also that the inner product is with respect to the Fourier transforms of these quantities, and weighted by $S_h(f)$.). If a signal exists within the raw data $h(t)$ that matches the expected waveform $u(t)$ then they will combine coherently, thus increasing the signal to noise ratio:

$$\frac{S}{N} \equiv \frac{\langle h, u\rangle}{rms\langle n, u\rangle} \tag{1.42}$$

It can be shown that matched filters are the best known method for extracting sinusoidal signals with known profiles from noise that is stationary and Gaussian (see e.g. [70]). The longer that the template $u(t)$ can be made to match the buried signal the better the signal to noise ratio becomes. Signals that have amplitudes A that are only one percent of the noise can be distinguished if the template matches it for thousands of cycles. It is thus very important for the operation of the interferometers to calculate accurate theoretical waveforms.

However, there are many complications. First the precise shape of the gravitational waves is not known, in part due to many parameters that describe the GW, relating to the structure of the source, and its orientation and position in the sky. This can be dealt with by creating banks of templates that cover the parameter space likely to be seen by the interferometers [71]. Additionally the assumption that the interferometer noise is stationary and Gaussian is overly simplistic, and a more realistic model of the noise needs to be computed and figured into matched filter. Algorithms such as FINDCHIRP [72] have been created to address these issues and thus dependably extract signals from the interferometer data.

1.6 Modeling Binary Evolutions

As discussed in the previous section, accurate theoretical models of the shapes of gravitational waves produced by astrophysically realistic sources are needed to help extract signals from modern interferometers. The most important sources for LIGO are compact binaries formed from neutron stars and black holes. We will discuss the general scheme for modeling black holes binaries here, although much of the scheme also applies to NS-NS and NS-BH binaries. Initially the two black holes are produced with a fairly large separation and so the binary will radiate weak GWs and the BHs will slowly spiral into one another (PSR B1913+16 is an example of a NS-NS system currently in this slow inspiral phase). Over time the separation will decrease, the binary will radiate more powerfully, and the BHs will inspiral more quickly. This progresses to the late inspiral, where the orbital parameters are changing considerably each period, which quickly leads to the plunge (near the Innermost Stable Circular Orbit (ISCO) point for a single BH) and merger of the BHs. The final resultant BH then quickly finishes radiating GWs during the ringdown phase and settles into its stationary state. These three phases of a binary evolution – the early to mid inspiral phase, the late inspiral, plunge and merger phase, and the final ringdown phase – require different theoretical methods to be accurately modeled.

The early inspiral phase is best investigated by post-Newtonian methods. As before for the study of gravitational waves, the metric is perturbatively split into a flat background $\eta_{\mu\nu}$ and successive corrections ${}^{(n)}h_{\mu\nu}$. It is not obvious that this perturbative technique is valid for the motions of black holes, the quintessential strong field objects. It is valid because general relativity obeys the Strong Equivalence Principle (SEP). In general relativity one always has the freedom to pick a local reference frame such that the black holes are in free fall. This thus means that the black holes move on geodesics of the background spacetime, just as a test body would. This is demonstrated by the successful use of post-Newtonian techniques to model the slow inspiral of binary pulsar PSR B1913+16, where, despite the strong gravity of the neutron stars the adherence to the SEP allows the motion to be treated as point like. We will use post-Newtonian techniques to verify the results of our numerical simulation of the late inspiral of a Nordström binary. In the next chapter we discuss the first order post-Newtonian corrections to the Keplerian motion of a Nordström binary. In chapter 4 we then calculate the energy and angular momentum radiated by a Nordström Binary.

The late inspiral, plunge and merger of a BH binary is perhaps the most important phase of the evolution. The strongest gravitational waves are produced during this phase, and they are in the sweet spot of the ground based detectors (see [73], [74], [75]). It is also one of the most interesting phases, with many strong field effects present, and thus also one of the hardest to model. The post-Newtonian perturbative expansion fails to converge due to these strong fields effects. This necessitates the use of full numerical relativity to model the evolution of the spacetime. Developing numerical techniques to model the late inspiral of a binary system is the goal of this thesis. An overview of numerical relativity techniques is given in a later chapter, and the results of our numerical investigation are given in chapter 5. By checking our results against post-Newtonian calculations (where both are in their domain of validity) we find that our techniques allow for long and stable binary evolutions of the late inspiral leading up to the plunge and merger of the bodies.

After the black holes have merged, forming a common event horizon, the rest of the evolution can again be modeled with perturbative techniques. In this case however, the background metric which the perturbations are expanded around is the isolated Schwarzschild or Kerr black hole metric instead of the flat space metric. One can show that during this ringdown phase that gravitational waves exponentially diminish the perturbations, leaving behind a stationary black hole [76],[77].

Chapter 2

Post-Newtonian Calculations

2.1 Introduction

Einstein's equations are a complex set of coupled nonlinear second order partial differential equations. They are thus very hard to solve analytically, and analytic solutions only exist for scenarios with a high amount of symmetry. A standard line of attack in math and physics for solving systems like this is to make a simplifying assumption that allows for a perturbative expansion to be used. In the case of general relativity we assume that the metric is close to being Lorentzian, and then solve for the weak field perturbations to the metric caused by the presence of matter (although expansion about other background metrics can also be useful, for instance calculating corrections to a black hole spacetime). As noted in the Introduction, the first level of the expansion gives Newtonian theory, as it must. A post-Newtonian analysis then continues the expansion and calculates the higher order effects.

In addition to making a weak field assumption, traditional post-Newtonian calculations also assume slow motion, with the velocity v of the objects being much less than the speed of light: $v \ll 1$ (having set $c = G = 1$). This is the case when the motion is generated by the weak fields: $v^2 \sim M/d$ (for a system of mass M and average separation d). We thus use powers of v as the expansion parameter, with Newtonian theory coming in at order v^2, the first post-Newtonian (1PN) level corrections appearing at order v^4 (no terms of order v^3 appear), and in general the nPN corrections give the v^{2+2n} order components of the metric (for instance radiation reaction effects enter at 2.5PN order, or at v^7).

The first calculation of post-Newtonian effects was performed by Einstein in the same year as the discovery of general relativity: he gave an explanation of the anomalous precession of the perihelion of Mercury [78]. Other early post-Newtonian calculations include Lorentz and Droste [79], and Einstein, Infeld, and Hoffmann's famous treatment: [80]. Later Chandrasekhar and his colleagues worked out the post-Newtonian equations of motion for massive fluid bodies (instead of approximating each body as a point mass and then considering its effect on its neighbors): [81], [82], [83], [84].

Chandrasekhars fluid body 2.5PN calculation [84] gives the same rate of energy loss due to gravitational waves as the point body versions of the calculation (such as Peters and Mathews [85], [86]). This is thus corroborating evidence for the Strong Equivalence Principle in general relativity. Recent research continues to uphold the SEP for general relativity, see e.g.: [87].

Nordström's 2nd theory forms the laboratory in which we will develop our techniques for numerical relativity. In order to check the accuracy of our techniques we need precise predictions for the character and evolution of binary orbits in Nordström's theory. We thus develop a post-Newtonian analysis for Nordström's theory. The analytic expressions for the post-Newtonian fields are additionally useful in that they can also be integrated up numerically and thus compared with the fields produced by the primary numerical code. In the first section we calculate the changes to a Keplerian Nordström binary due to 1PN effects. In the following section we calculate the decay of a Nordström binary due to radiation reaction.

2.2 Conserved Density

Before we delve into the details of the post-Newtonian analysis, it is first helpful to define the conserved density ρ^*. We first note that the contracted covariant derivative of a vector can be written without connection coefficients:

$$A^{\mu}_{;\mu} = (-g)^{-1/2}[(-g)^{1/2}A^{\mu}]_{,\mu} \tag{2.1}$$

In flat space we have conservation of rest mass given by $(\rho u^{\mu})_{,\mu}$, where ρ is the rest mass density (thus equal to $m_0 n$ with n particles in a small volume element dV, each with rest mass m_0), and u^{μ} is the four-velocity. This becomes $(\rho u^{\mu})_{;\mu}$ in a curved spacetime by following the "comma-goes-to-semicolon" rule.

We can then follow Will [88] and use (2.1) to define a conserved density:

$$\rho^* = \rho\sqrt{-g}u^0 \tag{2.2}$$

We can show that the conserved density has an "Eulerian" continuity equation:

$$\partial_t \rho^* = -\partial_i(\rho^* v^i) \tag{2.3}$$

The lack of connection coefficients lets us construct the general equation:

$$\frac{d}{dt}\int_V \rho^* f d^3x = \int_V \rho^* \frac{df}{dt} d^3x \tag{2.4}$$

with the special case of $f = 1$ giving the total rest mass of the system:

$$m = \int_V \rho^* d^3x, \qquad \frac{dm}{dt} = 0 \tag{2.5}$$

The useful properties of ρ^* will later appear repeatedly.

For instance, one can define a center of mass for the a'th body to be:

$$\mathbf{x}_a = \frac{1}{m_a}\int_a \rho^* \mathbf{x} d^3x \tag{2.6}$$

We then apply equation (4.40) two times to find that the acceleration $\mathbf{a}_a$ of the center of mass is equal to the weighted sum of the local coordinate accelerations:

$$\frac{dv_a^j}{dt} = \frac{1}{m_a}\int_a \rho^* \frac{dv^j}{dt} d^3x \tag{2.7}$$

2.3 Geodesic Motion to 1PN

We now turn to the issue of constructing a 1PN version of the metric for Nordström's theory. We first consider the geodesic motion of a test body in order to determine how far different metric components need to be expanded. We begin with the equation for geodesic motion:

$$\frac{du^\alpha}{d\tau} = -\Gamma^\alpha_{\beta\gamma} u^\beta u^\gamma \tag{2.8}$$

We can then transform the proper time τ derivatives to those in terms of the coordinate time t:

$$\frac{d^2x^i}{dt^2} = -\Gamma^i_{\beta\gamma} v^\beta v^\gamma + v^i \left[\Gamma^0_{\mu\nu} v^\mu v^\nu\right] \tag{2.9}$$

with $v^0 = 1$.

To Newtonian order we only need $-\Gamma^i_{00} = -\partial_i \Phi \sim v^2/d$. To go out to 1PN we thus need to compute Γ^i_{00} to $\sim v^4/d$, and, by examining (2.9) we see that in general we need:

$$\begin{aligned} &\Gamma^i_{00} \sim v^4/d; \qquad \Gamma^i_{0j} \sim v^3/d; \qquad \Gamma^i_{jk} \sim v^2/d; \\ &\Gamma^0_{00} \sim v^3/d; \qquad \Gamma^0_{0j} \sim v^2/d; \qquad \Gamma^0_{jk} \sim v/d \end{aligned} \tag{2.10}$$

For compactness the power of v that these correspond to will be indicated by a leading superscript, so that the Newtonian component of Γ^i_{00} is ${}^2\Gamma^i_{00}$, the 1PN of Γ^i_{00} is ${}^4\Gamma^i_{00}$ and so forth.

The components of the metric are then expected to be:

$$g_{00} = -1 + {}^2h_{00} + {}^4h_{00} + ... \tag{2.11}$$

$$g_{0i} = {}^3h_{0i} + {}^5h_{0i} + ... \tag{2.12}$$

$$g_{ij} = \delta_{ij} + {}^2h_{ij} + {}^4h_{ij} + ... \tag{2.13}$$

By using $g^{\alpha\beta}g_{\beta\gamma} = \delta^{\alpha}_{\gamma}$ we find for the raised indices metric, component by component,

$${}^2h^{00} = -{}^2h_{00} \tag{2.14}$$

$${}^4h^{00} = -{}^4h_{00} - ({}^2h_{00})^2 \tag{2.15}$$

$${}^3h^{0i} = {}^3h_{0i} \tag{2.16}$$

$${}^5h^{0i} = {}^5h_{0i} - {}^2h_{00}{}^3h_{0i} - {}^3h_{0j}{}^2h_{ji} \tag{2.17}$$

$${}^2h^{ij} = -{}^2h_{ij} \tag{2.18}$$

$${}^4h^{ij} = -{}^4h_{ij} + {}^2h_{ik}{}^2h_{kj} \tag{2.19}$$

Plugging these into

$$\Gamma^{\mu}_{\alpha\beta} = \frac{1}{2}g^{\mu\nu}[\partial_\beta g_{\nu\alpha} + \partial_\alpha g_{\beta\nu} - \partial_\nu g_{\alpha\beta}] \tag{2.20}$$

and keeping terms out to level specified in (2.10) tells us that we need to evaluate the following terms in the metric:

$${}^2h_{00}; \qquad {}^4h_{00}; \qquad {}^3h_{0i}; \qquad {}^2h_{ij} \tag{2.21}$$

2.4 Nordström's Post Newtonian Parameters

We now need to evaluate the metric components to the order given in (2.21) for Nordström's 2nd theory. The main equations for this theory are given by:

$$g_{\mu\nu} = (1+\varphi)^2 \eta_{\mu\nu} \tag{2.22}$$

and

$$R = 24\pi T \tag{2.23}$$

Equation (2.23) can be expanded by computing the Ricci scalar of (2.22) and by taking the trace of the perfect fluid stress energy tensor:

$$T^{\mu\nu} = (\rho + \rho\varepsilon + p/\rho)u^\mu u^\nu + pg^{\mu\nu} \tag{2.24}$$

where ρ is the rest mass density, ε is the internal energy, p is the pressure, and u^μ is the four velocity. For future reference we note that the internal energy ε and p/ρ are both the same order of magnitude as the square of the characteristic velocity: $\varepsilon \sim p/\rho \sim v^2$. We find:

$$\Box\varphi = 4\pi(1+\varphi)^3(\rho(1+\varepsilon) - 3p) \tag{2.25}$$

First consider (2.25). Split φ into pieces that go as the second and fourth powers of the velocity $\varphi = \varphi^{(2)} + \varphi^{(4)}$ (we don't consider higher order corrections). Equation (2.25) then splits into

$$\nabla^2\varphi^{(2)} = 4\pi\rho \tag{2.26}$$

and

$$-\partial_t^2\varphi^{(2)} + \nabla^2\varphi^{(4)} = 4\pi(3\varphi^{(2)}\rho + \rho\varepsilon - 3P) \tag{2.27}$$

Equation (2.26) has the solution

$$\varphi^{(2)} = -\int_V \frac{\rho(\mathbf{x}', t)}{|\mathbf{x} - \mathbf{x}'|} d^3x' = -U \tag{2.28}$$

where we use Will's definition of Newtonian gravitational potential U.

To solve equation (2.27) first introduce the superpotential χ:

$$\chi = -\int_V \rho(\mathbf{x}', t)|\mathbf{x} - \mathbf{x}'| d^3x' \tag{2.29}$$

the Laplacian of which is related to U:

$$\nabla^2 \chi = -2U \tag{2.30}$$

We thus find a solution for $\varphi^{(4)}$:

$$\varphi^{(4)} = \frac{1}{2}\partial_t^2 \chi + 3\Phi_2 - \Phi_3 + 3\Phi_4 \tag{2.31}$$

where

$$\Phi_2 = \int \frac{\rho' U'}{|\mathbf{x} - \mathbf{x}'|} d^3x' \tag{2.32}$$

$$\Phi_3 = \int \frac{\rho' \Pi'}{|\mathbf{x} - \mathbf{x}'|} d^3x' \tag{2.33}$$

$$\Phi_4 = \int \frac{p'}{|\mathbf{x} - \mathbf{x}'|} d^3x' \tag{2.34}$$

We can also expand out $\partial_t^2 \chi$:

$$\partial_t^2 \chi = A + B - \Phi_1 \tag{2.35}$$

where

$$A = \int \frac{\rho'}{|\mathbf{x}-\mathbf{x}'|^3}(\mathbf{v}'\cdot(\mathbf{x}-\mathbf{x}'))^2 d^3x' \tag{2.36}$$

$$B = \int \frac{\rho'}{|\mathbf{x}-\mathbf{x}'|}(\mathbf{x}-\mathbf{x}')\cdot\frac{d\mathbf{v}'}{dt} d^3x' \tag{2.37}$$

$$\Phi_1 = \int \frac{\rho' v'^2}{|\mathbf{x}-\mathbf{x}'|} d^3x' \tag{2.38}$$

We use these pieces to evaluate (2.22) to 1PN order. We find:

$$g_{00} = -1 + 2U - U^2 - A - B + \Phi_1 \tag{2.39}$$

$$-6\Phi_2 + 2\Phi_3 - 6\Phi_4$$

$$g_{0i} = 0 \tag{2.40}$$

$$g_{ij} = \delta_{ij}(1-2U) \tag{2.41}$$

If we follow Will and transform into the Standard Post Newtonian gauge (with $\lambda_1 = -1/2$ and $\lambda_2 = 0$), we find:

$$g_{00} = -1 + 2U - U^2 - 6\Phi_2 + 2\Phi_3 - 6\Phi_4 \tag{2.42}$$

$$g_{0i} = g_{i0} = 1/2(V_i - W_i) \tag{2.43}$$

$$g_{ij} = \delta_{ij}(1-2U) \tag{2.44}$$

where V_i and W_i are defined to be:

$$V_i = \int \frac{\rho' v_i'}{|\mathbf{x}-\mathbf{x}'|} d^3x' \tag{2.45}$$

$$W_i = \int \frac{\rho'\mathbf{v}'\cdot(\mathbf{x}-\mathbf{x}')(x-x')_i}{|\mathbf{x}-\mathbf{x}'|^3} d^3x' \tag{2.46}$$

By comparing to the PPN metric in [88] we find that Nordström's theory has post-Newtonian parameters $\gamma = -1, \beta = 1/2$ and all others are zero: $\xi = \alpha_1 = \alpha_2 = \alpha_3 =$

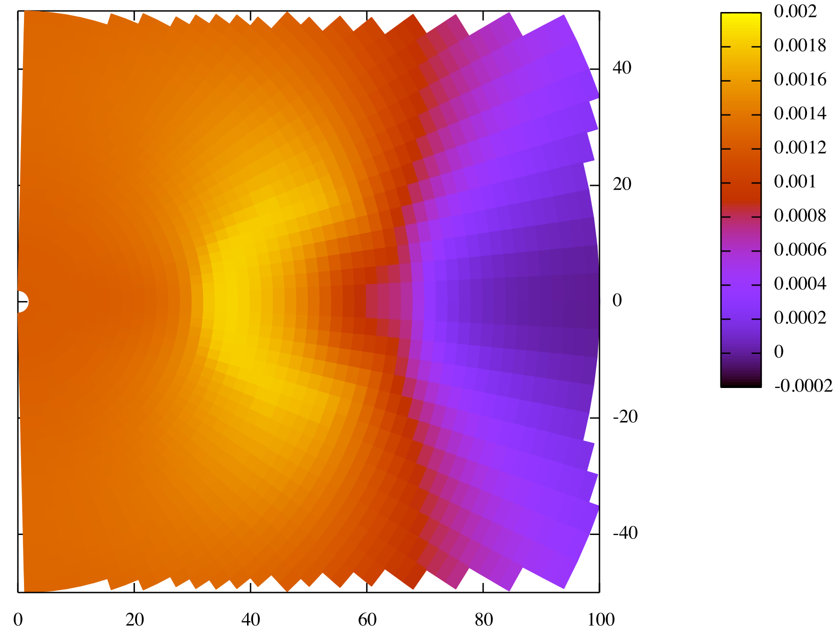

Figure 2.1: Diagram of the 1PN fields as generated by the main program (in spherical coordinates).

$\zeta_1 = \zeta_2 = \zeta_3 = \zeta_4 = 0$.

A side bonus of calculating the functional form of the 1PN fields is that they can also be integrated numerically and compared to the fields generated in the primary code. Figure (2.1) shows the primary codes' numerical solution for the scalar field φ in an equatorial slice near the star (having already subtracted off the Newtonian fields in order to emphasize the 1PN fields, although higher terms are carried along as well). Figure (2.2) shows the 1PN fields as directly integrated in equation (2.31) for a binary set up in the same fashion. This provides another check that the primary code is solving for φ accurately.

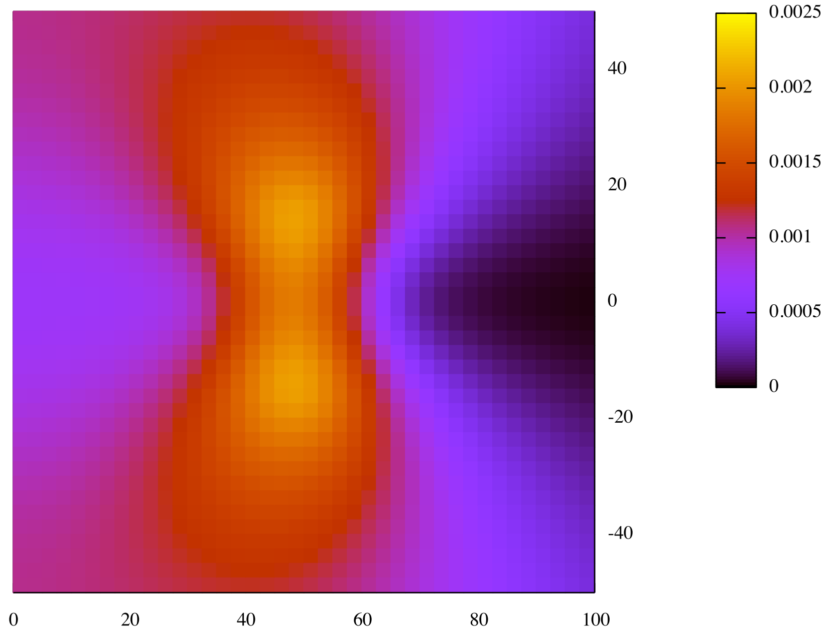

Figure 2.2: Diagram of the 1PN fields given by directly integrating equation (2.31).

2.5 Connection Coefficients

With the metric now in hand we can compute all of the connection coefficients needed as given in equation (2.10). We find:

$$^2\Gamma^i_{00} = -\partial_i U \tag{2.47}$$

$$^4\Gamma^i_{00} = -U\partial_i U + 3\partial_i\Phi_2 - \partial_i\Phi_3 + 3\partial_i\Phi_4 + (1/2)\partial_t(V_i - W_i) \tag{2.48}$$

$$^3\Gamma^i_{0j} = -\delta_{ij}\partial_t U \tag{2.49}$$

$$^2\Gamma^i_{jk} = -\delta_{ij}\partial_k U - \delta_{ik}\partial_j U + \delta_{jk}\partial_i U \tag{2.50}$$

$$^3\Gamma^0_{00} = -\partial_t U \tag{2.51}$$

$$^2\Gamma^0_{0j} = -\partial_j U \tag{2.52}$$

$$^1\Gamma^0_{jk} = 0 \tag{2.53}$$

Note that

$$^3\Gamma^i_{0j} = -\delta_{ij}\partial_t U \tag{2.54}$$

since $V_{[i,j]} - W_{[i,j]} = 0$

2.6 Acceleration Volume Integrals

In the previous subsection on the conserved density ρ^* we derived a quick expression for the acceleration of the center of mass (2.7). As we will see later, at lowest order the acceleration of star a is given by Newtonian inverse square law: $\ddot{x}_a = -m_b/d^2$, where m_b is the gravitational mass of star b, which is the same as its inertial mass (for theories that follow the SEP). To 1PN order the gravitational mass is given by:

$$m_b = \int_b \rho^*(1 + (1/2)\bar{v}^2 - (1/2)\bar{U} + \Pi)d^3x \tag{2.55}$$

with $\bar{\mathbf{v}} = \mathbf{v} - \mathbf{v}_{b(0)}$ being the relative velocity with respect to the velocity of the center of mass $\mathbf{v}_{b(0)}$:

$$\mathbf{v}_{b(0)} = \int_b \rho^* \mathbf{v} d^3x \tag{2.56}$$

and $\bar{U}$ is the self gravitational field:

$$\bar{U} = \int_b \rho(\mathbf{x}', t)|\mathbf{x} - \mathbf{x}'|^{-1} d^3x' \tag{2.57}$$

In general for star a, m_a is conserved $(dm_a/dt = 0)$ since:

$$\int_a \rho^* \frac{d}{dt}(1 + (1/2)\bar{v}^2 - (1/2)\bar{U} + \Pi) d^3x = 0 \tag{2.58}$$

Will uses the gravitational mass density instead of the conserved mass density to define a center of mass:

$$\mathbf{x}_a = m_a^{-1} \int_a \rho^*(1 + (1/2)\bar{v}^2 - (1/2)\bar{U} + \Pi)\mathbf{x} d^3x \tag{2.59}$$

Taking the time derivative of this gives the velocity of the center of mass:

$$\begin{aligned} \mathbf{v}_a = m_a^{-1} &\int_a \rho^*(1 + (1/2)\bar{v}^2 - (1/2)\bar{U} + \Pi)\mathbf{v} d^3x \\ &+ m_a^{-1} \int_a p\bar{\mathbf{v}} - (1/2)\rho^* \bar{\mathbf{W}} d^3x \end{aligned} \tag{2.60}$$

with

$$\bar{W}_i = \int_a \rho' \frac{\bar{\mathbf{v}}' \cdot (\mathbf{x} - \mathbf{x}')(x_i - x_i')}{|\mathbf{x} - \mathbf{x}'|^3} \tag{2.61}$$

since

$$-m_a^{-1} \int_a x^i \partial_j (p\bar{v}^j) d^3x = m_a^{-1} \int_a p\bar{v}^i d^3x \tag{2.62}$$

and

$$m_a^{-1} \int_a \rho^*(v^j \partial_j U - \partial_t U) x^i d^3x = -m_a^{-1} \int_a \rho^* \bar{W}_i d^3x \tag{2.63}$$

By taking one more time derivative we find the acceleration of the center of mass $\mathbf{a}_a = d\mathbf{v}_a/dt$:

$$\begin{aligned} \mathbf{a}_a = m_a^{-1} \int_a \rho^*(1 + (1/2)\bar{v}^2 - (1/2)\bar{U} + \Pi) \frac{d\mathbf{v}}{dt} d^3x \\ + m_a^{-1} \left[v_a^j \int_a p_{,j} \bar{\mathbf{v}} d^3x + \int_a [p_{,0}\bar{\mathbf{v}} - (p/\rho^*)\nabla p] d^3x \right] \\ + m_a^{-1} \left[-\frac{1}{2}\frac{d}{dt} \int_a \rho^* \bar{\mathbf{W}} d^3x + \frac{1}{2}\mathcal{T}_a - \frac{1}{2}\mathcal{T}_a^* + \mathcal{P}_a \right] \end{aligned} \tag{2.64}$$

with

$$\mathcal{T}_a^j = \int_a \frac{\rho^* \rho^{*\prime} \bar{v}^{\prime j} \bar{\mathbf{v}}' \cdot (\mathbf{x} - \mathbf{x}')}{|\mathbf{x} - \mathbf{x}'|^3} d^3x d^3x' \tag{2.65}$$

and

$$\mathcal{T}_a^{*j} = \int_a \frac{\rho^* \rho^{*\prime} \bar{v}^{j} \bar{\mathbf{v}}' \cdot (\mathbf{x} - \mathbf{x}')}{|\mathbf{x} - \mathbf{x}'|^3} d^3x d^3x' \tag{2.66}$$

and

$$\mathcal{P}_a^j = \int_a \frac{\rho^* p' (x - x')^j}{|\mathbf{x} - \mathbf{x}'|^3} d^3x d^3x' = - \int_a \rho^* \Phi_{4a,j} d^3x \tag{2.67}$$

Will then uses this expression to derive the acceleration of a fluid body to first post-Newtonian order (see [88]). However we will make use of the hydro-without-hydro approximation (see [89]), which simplifies or eliminates many of these terms. In fact the same final acceleration is found by integrating over the conserved density ρ^* as in (2.7), so we will use this simpler and equivalent equation.

2.7 Expanding $T^{\mu\nu}{}_{;\nu} = 0$

We now need to derive an expression, accurate to 1PN, for the local coordinate acceleration that a fluid element undergoes. We find this by expanding the divergence of the stress-energy tensor $T^{\mu\nu}{}_{;\nu} = 0$, and acting on it with the projection operator $Q^\alpha_\mu = u^\alpha u_\mu + \delta^\alpha_\mu$. We find that

$$Q^j_\mu T^{\mu\nu}{}_{;\nu} = 0 \tag{2.68}$$

reduces to:

$$\rho h u^\nu u^j{}_{;\nu} + Q^{j\nu} p_{,\nu} = 0 \tag{2.69}$$

where h is the enthalpy: $h = 1 + \varepsilon + p/\rho$. We can then expand this, solving for the local coordinate acceleration, and get:

$$\begin{aligned}\rho^* \frac{dv^j}{dt} = -\rho^* \Gamma^j_{\alpha\beta} v^\alpha v^\beta - (u^0)^{-1} \rho^* v^j \frac{du^0}{dt} \\ -(u^0)^{-2} \frac{\rho^*}{\rho h} Q^{j\nu} p_{,\nu}\end{aligned} \tag{2.70}$$

We now go through (2.70) and keep only the terms that contribute to the 1PN acceleration. We first examine:

$$\begin{aligned}-\rho^* \Gamma^j_{\alpha\beta} v^\alpha v^\beta = -\rho^* [{}^2\Gamma^j_{00} + {}^4\Gamma^j_{00}] \\ -\rho^* [2 {}^3\Gamma^j_{k0} v^k + {}^2\Gamma^j_{kl} v^k v^l]\end{aligned} \tag{2.71}$$

The first term on the Right Hand Side (RHS) gives:

$$\begin{aligned}-\rho^* [{}^2\Gamma^j_{00} + {}^4\Gamma^j_{00}] = \rho^* [U_{,j} + U U_{,j} - 3\Phi_{2,j} \\ +\Phi_{3,j} - 3\Phi_{4,j} - (1/2)(V_j - W_j)_{,0}]\end{aligned} \tag{2.72}$$

while the second term on the RHS becomes

$$-\rho^* [2 {}^3\Gamma^j_{k0} v^k + {}^2\Gamma^j_{kl} v^k v^l] = \rho^* \left[2 v^j \frac{dU}{dt} - v^2 U_{,j} \right] \tag{2.73}$$

to 1PN order.

With $u^0 = 1 + (1/2) v^2 + U + \mathcal{O}(v^4)$ the second term on the RHS of (2.70) becomes:

$$-(u^0)^{-1} \rho^* v^j \frac{du^0}{dt} = -\rho^* v^j \left[v^k \frac{dv^k}{dt} + \frac{dU}{dt} \right] \tag{2.74}$$

We then combine equations (2.73) and (2.74), and use $dv^k/dt = U_{,k} - (1/\rho)p_{,k}$ and $dU/dt = U_{,t} + v^k U_{,k}$ to get:

$$-\rho^*[2^3\Gamma^j_{k0}v^k + {}^2\Gamma^j_{kl}v^k v^l] - (u^0)^{-1}\rho^* v^j \frac{du^0}{dt} = \rho^*[v^j U_{,0} - v^2 U_j + v^j v^k p_{,k}] \quad (2.75)$$

Finally we have:

$$-\frac{1}{(u^0)^2}\frac{\rho^*}{\rho h}Q^{j\nu}p_{,\nu} = -\frac{\rho^*}{\rho h}[v^j p_{,0} + v^j v^k p_{,k}] - \frac{1}{(u^0)^2}\frac{\rho^*}{\rho h}[g^{j0}p_{,0} + g^{jk}p_{,k}] \quad (2.76)$$

Dropping terms smaller than $\mathcal{O}(v^4)$ we find:

$$\frac{-1}{(u^0)^2}\frac{\rho^*}{\rho h}Q^{j\nu}p_{,\nu} = -[v^j p_{,0} + v^j v^k p_{,k}] + (-1 + (1/2)v^2 + 3U + \Pi + p/\rho)p_{,j} \quad (2.77)$$

The two $v^j v^k p_{,k}$ terms cancel.

After canceling out all of the relevant terms we find that $T^{\mu\nu}_{;\nu} = 0$ reduces to:

$$\rho^*\frac{dv^j}{dt} = \rho^* U_{,j}[1 - v^2 + U] + p_{,j}(-1 + 3U + \frac{1}{2}v^2 + \Pi + p/\rho^*) - \frac{1}{2}\rho^*(V^j - W^j)_{,0} + v^j(\rho^* U_{,0} - p_{,0}) + \rho^*[-3\Phi_{2,j} + \Phi_{3,j} - 3\Phi_{4,j}] \quad (2.78)$$

This is essentially the same expression given in Will's book (6.29 - filling in $\beta = 1/2$ and $\gamma = -1$), although note that two $3pU_{,j}$ terms from the equation in Will's book have also already been canceled.

2.8 1PN Acceleration

We now have almost all of the pieces we need to crank through the calculation and find the acceleration to 1PN. First we need to find the time derivatives of V_i and W_i. Expanding out we get:

$$\partial_t V_i = \int \frac{[\partial_t \rho(x', t)] v_i'}{|\mathbf{x} - \mathbf{x}'|} d^3x' + \int \frac{\rho' [\partial_t v_i(x', t)]}{|\mathbf{x} - \mathbf{x}'|} d^3x' \tag{2.79}$$

We use the continuity equation $\partial_t \rho = -\partial_j (v^j \rho)$, and then integration by parts to transform the first integral:

$$\int \frac{[\partial_t \rho'] v_i'}{|\mathbf{x} - \mathbf{x}'|} d^3x' = \int \rho' v'^j \frac{\partial}{\partial x'^j} \left[\frac{v_i'}{|\mathbf{x} - \mathbf{x}'|} \right] d^3x' \tag{2.80}$$

We thus find for V_i:

$$\partial_t V_i = \int \frac{\rho'}{|\mathbf{x} - \mathbf{x}'|} \frac{dv_i'}{dt} d^3x' + \int \frac{\rho' v_i' \mathbf{v}' \cdot (\mathbf{x} - \mathbf{x}')}{|\mathbf{x} - \mathbf{x}'|^3} d^3x' \tag{2.81}$$

Likewise for W_i we have:

$$\begin{aligned} \partial_t W_i = \int \frac{\rho'(x_i - x_i')}{|\mathbf{x} - \mathbf{x}'|^3} (\mathbf{x} - \mathbf{x}') \cdot \frac{d\mathbf{v}'}{dt} d^3x' \\ + \int \rho' v'^j v'^k \frac{\partial}{\partial x'^k} \left[\frac{(x_i - x_i')(x_j - x_j')}{|\mathbf{x} - \mathbf{x}'|^3} \right] d^3x' \end{aligned} \tag{2.82}$$

Distributing the derivatives we get the final expression for W_i:

$$\begin{aligned} \partial_t W_i = \int \frac{\rho'(x_i - x_i')}{|\mathbf{x} - \mathbf{x}'|^3} (\mathbf{x} - \mathbf{x}') \cdot \frac{d\mathbf{v}'}{dt} d^3x' \\ - \int \frac{\rho' \mathbf{v}' \cdot (\mathbf{x} - \mathbf{x}') v_i'}{|\mathbf{x} - \mathbf{x}'|^3} d^3x' - \int \frac{\rho' v'^2 (x_i - x_i')}{|\mathbf{x} - \mathbf{x}'|^3} d^3x' \\ + 3 \int \frac{\rho' [\mathbf{v}' \cdot (\mathbf{x} - \mathbf{x}')]^2 (x_i - x_i')}{|\mathbf{x} - \mathbf{x}'|^5} d^3x' \end{aligned} \tag{2.83}$$

Let's convert all the ρ terms to ρ^* terms in (2.78). We have $\rho = \rho^*(1-(1/2)v^2+3U)$ to 1PN order – we will swap this into the first term $\rho^* U_{,j}$, and directly substitute ρ^* for ρ in all of the other order v^4 post-Newtonian terms. We get:

$$U^* = \int_a \frac{\rho^{*\prime}}{|\mathbf{x}-\mathbf{x}'|} d^3x' + \int_b \frac{\rho^{*\prime}}{|\mathbf{x}-\mathbf{x}'|} d^3x' = U_a^* + U_b^* \tag{2.84}$$

And

$$U = U^* - (1/2)\Phi_1 + 3\Phi_2 \tag{2.85}$$

We won't bother adding an asterisk to all the other terms (such as V^j), but they are now understood to be integrals over ρ^*.

For our present purposes we wish to show that Nordström's theory has no lowest order Nordtvedt effect, so we will make the simplifying assumption that we are in circular orbit, so that $\mathbf{v} \cdot (\mathbf{x} - \mathbf{x}') \sim 0$. We will state the more general case valid for eccentric orbits at the end. We will also make the objects irrotational so that $\bar{\mathbf{v}} = 0$. V^j and W^j then simplify to:

$$\partial_t V^j = \int \frac{\rho^{*\prime}}{|\mathbf{x}-\mathbf{x}'|} \frac{dv'^j}{dt} d^3x' \tag{2.86}$$

$$\partial_t W^j = \int \frac{\rho^{*\prime}(x-x')^j}{|\mathbf{x}-\mathbf{x}'|^3} (\mathbf{x}-\mathbf{x}') \cdot \frac{d\mathbf{v}'}{dt} d^3x' + \Phi_{1,j} \tag{2.87}$$

The $(1/2)\Phi_{1,j}$ terms from the $W^j_{,t}$ and $\rho^* U_{,j}$ terms cancel, as do the two $3\Phi_{2,j}$ terms.

Let's now substitute out dv^j/dt in (2.86) and (2.87). To the order we are considering we can use the Newtonian solution and thus we have $dv^j/dt = U_{,j} - (1/\rho)p_{,j}$. In the region of star a we can split this up into:

$$dv^j/dt = U^*_{b,j} \tag{2.88}$$

$$p_{,j} = \rho^* U^*_{a,j} \tag{2.89}$$

to order v^2. In other words, the local potential field U_a is balanced by the pressure, and the acceleration is due to the field from the b star: U_b. $V^j_{,t}$ thus becomes:

$$\partial_t V^j = \int_a \frac{\rho^{*\prime}}{|\mathbf{x}-\mathbf{x}'|} U^{*\prime}_{b\,,j} d^3x' + \int_b \frac{\rho^{*\prime}}{|\mathbf{x}-\mathbf{x}'|} U^{*\prime}_{a\,,j} d^3x' \tag{2.90}$$

We will then integrate this over the volume of the a star: $-(1/2)\int_a \rho^* \partial_t V^j d^3x$, and for a large separation the b integral in $\partial_t V^j$ will drop out, leaving:

$$-\frac{1}{2}\int_a \rho^* \partial_t V^j d^3x = -\frac{1}{2}\int_a \rho^* \int_a \frac{\rho^{*\prime}}{|\mathbf{x}-\mathbf{x}'|} U^{*\prime}_{b\,,j} d^3x' d^3x \tag{2.91}$$

For large separations, $U^*_{b\,,j}$ will be about constant in the volume of a, and can thus be moved through the d^3x' integral, giving:

$$-\frac{1}{2}\int_a \rho^* \partial_t V^j d^3x = -\frac{1}{2}\int_a \rho^* U^*_a U^*_{b\,,j} d^3x \tag{2.92}$$

Likewise $W^j_{,t}$ becomes (having already canceled the $(1/2)\Phi_{1,j}$ term...):

$$W^j_{,t} = U^*_{b\,,j} \int_a \frac{\rho^{*\prime}((x-x')^j)^2}{|\mathbf{x}-\mathbf{x}'|^3} d^3x' = \frac{1}{3} U^*_{b\,,j} U^*_a \tag{2.93}$$

Thus

$$\frac{1}{2}\int_a \rho^* \partial_t W^j d^3x = \frac{1}{6}\int_a \rho^* U^*_a U^*_{b\,,j} d^3x \tag{2.94}$$

Let's next address the $p_{,j}(-1 + 3U^* + (1/2)v^2 + \Pi + p/\rho^*)$ term in equation (70). Use $p_{,j} = \rho^* U^*_{a,j}$ and the only term that survives is:

$$\int_a p_{,j} 3U^*_b d^3x = 3\int_a \rho^* U^*_{a,j} U^*_b d^3x \tag{2.95}$$

This is derived assuming that the separation is sufficient that tidal forces are not in play, and thus $p_{,j}$ is antisymmetric in volume a, while all the other fields except for

U_b^* are symmetric in a, and thus all integrate up to zero. We can switch the derivative on U_a^* onto U_b^* and thus pick up a numerical factor of $-1/6$:

$$\int_a p_{,j} 3U_b^* d^3x = -\frac{1}{2}\int_a \rho^* U_a^* U_{b,j}^* d^3x \tag{2.96}$$

Next we address the $\rho^*\Phi_{3,j}$ term in equation (70). We have

$$\Phi_3 = \int_a \frac{\rho^{*\prime}\Pi'}{|\mathbf{x}-\mathbf{x}'|} d^3x' + \int_b \frac{\rho^{*\prime}\Pi'}{|\mathbf{x}-\mathbf{x}'|} d^3x' = \Phi_{3a} + \Phi_{3b} \tag{2.97}$$

The integral over a is antisymmetric so only $\rho^*\Phi_{3b,j}$ remains (this leads to a final term).

Next we have $-3\rho^*\Phi_{4,j} = -3\rho^*\Phi_{4a,j} - 3\rho^*\Phi_{4b,j}$, where again only the Φ_{4b} term survives. We have:

$$\Phi_{4b,j} = \frac{\partial}{\partial x^j}\int_b \frac{p'}{|\mathbf{x}-\mathbf{x}'|} d^3x' = \int_b \frac{1}{|\mathbf{x}-\mathbf{x}'|}\frac{\partial p'}{\partial x^{j\prime}} d^3x' \tag{2.98}$$

Thus:

$$\begin{aligned} -3\int_a \rho^*\Phi_{4b,j} d^3x &= -3\int_a \rho^* \int_b \frac{1}{|\mathbf{x}-\mathbf{x}'|}\rho^{*\prime} U_{b\ ,j}^{*\prime} d^3x' d^3x \\ &= -3\int_b U_a^{*\prime}\rho^{*\prime} U_{b\ ,j}^{*\prime} d^3x' = \frac{1}{2}\int_b U_{a,j}^{*\ \prime}\rho^{*\prime} U_b^{*\prime} d^3x' \end{aligned} \tag{2.99}$$

The $-\rho^* U_{,j}^* v^2$ is essentially already a final term, becoming $-\int_a \rho^* U_{b,j}^* v^2 d^3x$. This leaves finally the $\rho^* U_{,j}^* U^*$ term. We have:

$$\begin{aligned} \int_a \rho^* U_{,j}^* U^* d^3x &= \int_a \rho^* U_{a,j}^* U_b^* d^3x \\ + \int_a \rho^* U_{b,j}^* U_a^* d^3x &+ \int_a \rho^* U_{b,j}^* U_b^* d^3x \end{aligned} \tag{2.100}$$

The first term on the RHS is canceled by the $(1/2)W_{,t}^j$ term and the second term is canceled by the combination of the $-(1/2)V^j_{,t}$ and $3p_{,j}U$ terms, leaving only $\int_a \rho^* U^*_{b,j} U^*_b d^3x$.

The terms we are left with are:

$$m_a^{-1} \int_a \rho^*(1 - (1/2)\bar{U} + \Pi) U^*_{b,j} d^3x \tag{2.101}$$

$$m_a^{-1} \int_a \rho^* \Phi^*_{3b,j} d^3x \tag{2.102}$$

$$m_a^{-1} \frac{1}{2} \int_b U^*_{a,j}{}' \rho^{*\prime} U^{*\prime}_b d^3x' \tag{2.103}$$

$$m_a^{-1} \int_a \rho^* U^*_{b,j} U^*_b d^3x \tag{2.104}$$

$$-m_a^{-1} \int_a \rho^* U^*_{b,j} v^2 d^3x \tag{2.105}$$

For large separations terms like $U^*_{b,j}$ will essentially be constant in the volume of the a star and can be pulled through the integrals. Everything combines to give an acceleration of:

$$a^j_a = m_b \frac{-x^j_{ab}}{(r_{ab})^3} \left[1 + \frac{m_b}{r_{ab}} - v_a^2\right] \tag{2.106}$$

There is thus no Nordtvedt effect as star a accelerates with respect to the m_b mass (modulated by the n-body effects m_b/r_{ab} and $-v_a^2$)

In general when the orbits are eccentric (to lowest order) we can't make the simplifying assumption $\mathbf{v} \cdot \mathbf{x}_{ab} \sim 0$. If the binary is instantaneously oriented such the separation vector $\mathbf{x}_{ab}$ is aligned along the $\hat{x}$ axis, with most of the velocity in the $\hat{y}$ direction, then we can solve for the acceleration in the $\hat{x}$ direction:

$$\ddot{x}_a = -\frac{M_b}{d^2} \left(1 + \frac{M_b}{d} - v_a^2 - \frac{3}{2}(v^x_b)^2 - (v^x_a - v^x_b) v^x_b\right) \tag{2.107}$$

and $\hat{y}$ direction:

$$\ddot{y}_a = \frac{M_b (v^y_a - v^y_b) v^x_b}{d^2} \tag{2.108}$$

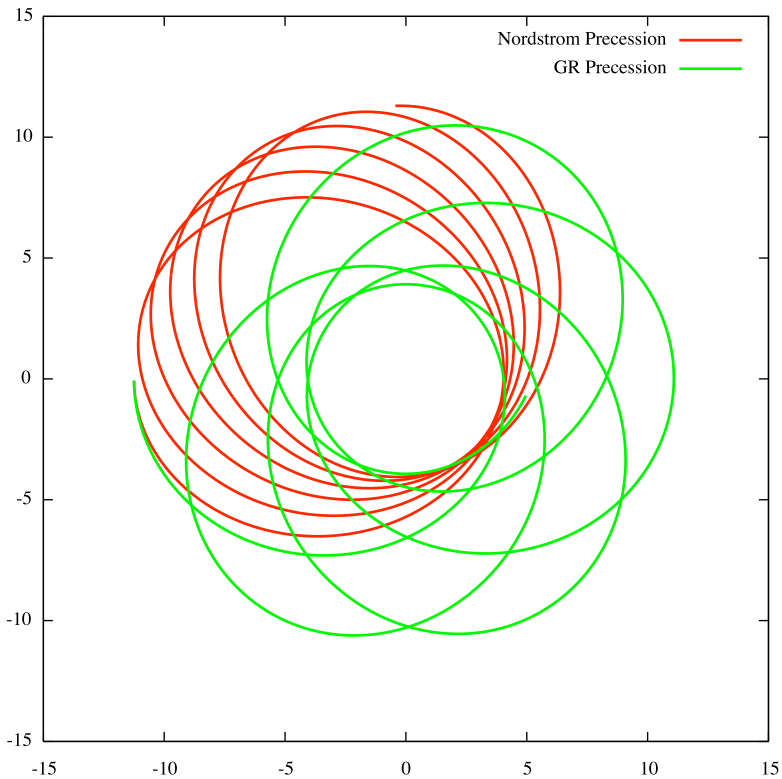

Figure 2.3: Diagram of a binaries precession in both Nordström's theory and general relativity

The primary effect of these 1PN corrections is to give rise to a precession of binary orbit. The precession is $-1/6$ of the rate found for general relativity (see [88]):

$$\Delta\tilde{\omega} = -\frac{\pi M}{d} \tag{2.109}$$

An example of the precession of a tight binary for both Nordström's theory and general relativity is given in figure (2.3). As we later see however, (2.109) is only valid for Nordstrom's in the limit that the stars are not compact. For compact stars there are deviations from (2.109) even at large separations since Nordström's theory violates the Strong Equivalence Principle at 2PN and higher orders (as most likely all metric theories do other than general relativity). Nordström's theory is somewhat special among alternative theories of gravitation in that it doesn't violate the SEP at 1PN order order and thus does not give rise to Nordtvedt effects at that order.

2.9 Energy Loss Due to GWs in GR

In chapter 4 we calculate the energy and angular momentum radiated by a binary in Nordström's theory. This radiation causes the binary to inspiral much in the same way as binaries do in general relativity. We thus give here the classical derivation of gravitational wave radiation in general relativity, as we will use it for guidance in reproducing the calculation in Nordström's theory.

In order to compute the energy loss due to gravitational waves in a radiating system we first need an expression for the energy of the gravitational wave. We will use Isaacson's shortwave formalism as described in MTW [11]. The waves are assumed to be propagating in a vacuum background spacetime that has a typical curvature of $\Re$. Since the waves are a perturbation on the background, we have that the amplitude of the wave A is much less than the average magnitude of the metric: $A \ll 1$, and the wavelength λ is much shorter than the background curvature: $\lambda \ll \Re$. The general metric can then be split up into a background metric $g^{(B)}$ and a perturbation h:

$$g_{\mu\nu} = g_{\mu\nu}^{(B)} + h_{\mu\nu} \tag{2.110}$$

The Ricci tensor then splits into:

$$R_{\mu\nu} = R_{\mu\nu}^{(B)} + R_{\mu\nu}^{(1)}(h) + R_{\mu\nu}^{(2)}(h) \tag{2.111}$$

with $R^{(1)}$ of order A/λ^2, $R^{(2)}$ of order A^2/λ^2, and $R^{(B)}$ as yet undetermined. In vacuum we have $R_{\mu\nu} = 0$ which must cancel order-by-order in A. If we assume that the background curvature $R^{(B)}$ is due to the energy of the gravitational waves, then it will higher order in A than $R^{(1)}$, thus giving:

$$R_{\mu\nu}^{(1)}(h) = 0 \tag{2.112}$$

and

$$R_{\mu\nu}^{(B)} + \langle R_{\mu\nu}^{(2)}(h) \rangle = 0 \tag{2.113}$$

Equation (2.112) gives the equations of motion for the perturbation $h_{\mu\nu}$. Equation (2.113) can be rewritten by constructing a stress energy tensor from the gravitational waves:

$$G_{\mu\nu}^{(B)} \equiv R_{\mu\nu}^{(B)} - \frac{1}{2} R^{(B)} g_{\mu\nu}^{(B)} = 8\pi T_{\mu\nu}^{(GW)} \tag{2.114}$$

with

$$T_{\mu\nu}^{(GW)} = -\frac{1}{8\pi} \left[\langle R_{\mu\nu}^{(2)}(h) \rangle - \frac{1}{2} g_{\mu\nu}^{(B)} \langle R^{(2)}(h) \rangle \right] \tag{2.115}$$

Further calculations can reduce $T_{\mu\nu}^{(GW)}$ into the following form:

$$T_{\mu\nu}^{(GW)} = \frac{1}{32\pi} \langle \bar{h}_{ij,\mu}^{TT} \bar{h}_{ij,\nu}^{TT} \rangle \tag{2.116}$$

which is generally what we would expect for the energy, i.e. the square of the first derivatives of the potential, just as for electromagnetic fields (the brackets indicate averaging over several wavelengths, since the energy can not be localized precisely).

$T_{\mu\nu}^{(GW)}$ also obeys

$$T^{(GW)\mu\nu}{}_{,\nu} = 0 \tag{2.117}$$

so if we integrate equation (2.116) over the volume of a sphere, and apply the divergence theorem we get:

$$\int T_{00,0}^{(GW)} d^3x = \frac{dE}{dt} = \int T_{0i,i}^{(GW)} d^3x = \int T_{0i}^{(GW)} n^i dS \tag{2.118}$$

The perturbations h are waves so one can convert a spatial derivative to one in time: $\bar{h}_{\mu\nu,i} = -n^i \bar{h}_{\mu\nu,0}$ (with $n^{i2} = 1$) thus transforming (2.118) into

$$\frac{dE}{dt} = -\int T_{00}^{(GW)} r^2 d\Omega \tag{2.119}$$

We now need to determine the form of the waves $\bar{h}_{ij}^{TT}$, which will be generated by some matter source. By going through the discussion given in the Introduction section on gravitational waves we find:

$$\Box \bar{h}_{\mu\nu} = -16\pi (T_{\mu\nu} + t_{\mu\nu}) \tag{2.120}$$

where $T_{\mu\nu}$ is the stress energy tensor for the matter, while $t_{\mu\nu}$ is a re-expression of $R_{\mu\nu}^{(2)}(h)$ (this source is called $X_{\mu\nu}$ in Peters [86]). The solution to this is given by:

$$\bar{h}^{\mu\nu}(t, x^j) = 4 \int \frac{[T^{\mu\nu} + t^{\mu\nu}]_{ret}}{|x - x'|} d^3x' \tag{2.121}$$

where the subscript "ret" indicates it is to be evaluated at the retarded time $t' = t - |x - x'|$. For the observation point at x much larger than the spatial integration variable x': $|x| >> |x'|$ $1/|x-x'|$ can be sufficiently approximated by $1/r$. The dependence of $T^{\mu\nu}$ on t' can be expanded out by using:

$$\begin{aligned} &T^{\mu\nu}(t-|x-x'|, x'^j) = \\ \sum_{n=0}^{\infty}\frac{1}{n!}&\left[\frac{\partial^n}{\partial t^n}T^{\mu\nu}(t-r, x'^j)\right](r-|x-x'|)^n \end{aligned} \tag{2.122}$$

and the expansion for $(r-|x-x'|)$ is

$$r-|x-x'| = x^j\frac{x'^j}{r}+\frac{1}{2}\frac{x^jx^k}{r}\left(\frac{x'^jx'^k-r'^2\delta_{jk}}{r^2}\right)+... \tag{2.123}$$

where we will only keep the leading term. A similar expansion is performed for $t^{\mu\nu}$. For brevity, set $T^{\mu\nu}+t^{\mu\nu} = S^{\mu\nu}$. We find:

$$\begin{aligned} \bar{h}^{\mu\nu}(t,x) = \frac{4}{r}\int[&S^{\mu\nu}+(\partial_t S^{\mu\nu})\frac{x^j}{r}x'^j \\ &+(\partial_t^2 S^{\mu\nu})\frac{x^jx^k}{r^2}x'^jx'^k+...]d^3x' \end{aligned} \tag{2.124}$$

which is reorganized into:

$$\begin{aligned} \bar{h}^{\mu\nu}(t,x) = \frac{4}{r}&\left[\int S^{\mu\nu}d^3x'+\frac{x^j}{r}\partial_t\int S^{\mu\nu}x'^jd^3x'\right] \\ &+\frac{4}{r}\left[\frac{x^jx^k}{r^2}\partial_t^2\int S^{\mu\nu}x'^jx'^kd^3x'\right] \end{aligned} \tag{2.125}$$

The dominate term in this expansion is $4/r\int S^{ij}d^3x'$, so dropping the higher order terms we are left with

$$\bar{h}^{ij}(t,x) = \frac{4}{r}\int S^{ij}d^3x' \tag{2.126}$$

We need to convert (2.126) into a more useful form. Given that the divergence of the source is zero we can find:

$$S^{\mu\nu}{}_{,\nu} = 0 \rightarrow S^{00}{}_{,00} = -S^{0l}{}_{,l0} = +S^{ml}{}_{,ml} \tag{2.127}$$

and thus

$$[S^{00}x^j x^k]_{,00} = S^{00}_{,00}x^j x^k = S^{ml}_{,ml}x^j x^k \tag{2.128}$$

since $\partial x^j/\partial x^0 = \delta^j_0 = 0$. Likewise we can find:

$$[S^{ml}x^j x^k]_{,ml} = S^{ml}_{,ml}x^j x^k + 2[S^{mj}x^k + S^{mk}x^j]_{,m} - 2S^{jk} \tag{2.129}$$

Therefore the term $\int S^{ij}d^3x'$ in equation (2.126) can be expressed as:

$$\int S^{ij}d^3x' = \frac{1}{2}(d^2 I_{jk}/dt^2) \tag{2.130}$$

with

$$I_{jk}(t) = \int S^{00}x'^j x'^k d^3x' \tag{2.131}$$

We thus have for h_{ij} (resuming bar notation...):

$$\bar{h}_{ij}(t,x) = \frac{2}{r}\frac{d^2 I_{jk}(t-r)}{dt^2} \tag{2.132}$$

We now want to extract the transverse traceless component, $\bar{h}^{TT}_{jk}$. We first put I_{jk} in traceless form with $\tilde{I}_{jk} = I_{jk} - 1/3\delta_{jk}I_{ll}$. The projection operators:

$$P_{lm} = \delta_{lm} - n_l n_m; n_l = x^l/r \tag{2.133}$$

can then be used to place it in transverse traceless form:

$$\tilde{I}^{TT}_{jk} = P_{jl}\tilde{I}_{lm}P_{mk} - \frac{1}{2}P_{jk}(P_{lm}\tilde{I}_{lm}) \tag{2.134}$$

We now have:

$$\bar{h}_{ij}^{TT}(t,x) = \frac{2}{r}\frac{d^2\tilde{I}_{ij}^{TT}(t-r)}{dt^2} \tag{2.135}$$

We will need the square of $\tilde{I}_{ij}^{TT}$:

$$\begin{aligned}(\tilde{I}_{ij}^{TT})^2 = P_{ik}\tilde{I}_{kl}P_{lj}P_{im}\tilde{I}_{mn}P_{nj} - \frac{1}{2}P_{ik}\tilde{I}_{kl}P_{lj}P_{ij}(P_{mn}\tilde{I}_{mn}) \\ -\frac{1}{2}P_{im}\tilde{I}_{mn}P_{nj}P_{ij}(P_{kl}\tilde{I}_{kl}) + \frac{1}{4}P_{ij}(P_{kl}\tilde{I}_{kl})P_{ij}(P_{mn}\tilde{I}_{mn})\end{aligned} \tag{2.136}$$

P_{ij} has the properties:

$$P_{ij}P_{jk} = P_{ik}; \qquad P_{ij}n_j = 0; \qquad P_{ii} = 2 \tag{2.137}$$

The first term in (2.136) becomes:

$$P_{km}P_{nl}\tilde{I}_{kl}\tilde{I}_{mn} = \tilde{I}_{nk}^2 - 2n_l n_n \tilde{I}_{nk}\tilde{I}_{kl} + n_k n_l n_m n_n \tilde{I}_{kl}\tilde{I}_{mn} \tag{2.138}$$

Likewise the next two terms combine to form:

$$P_{kl}P_{mn}\tilde{I}_{kl}\tilde{I}_{mn} = -n_k n_l n_m n_n \tilde{I}_{kl}\tilde{I}_{mn} \tag{2.139}$$

and the final terms give:

$$\frac{1}{2}P_{kl}P_{mn}\tilde{I}_{kl}\tilde{I}_{mn} = \frac{1}{2}n_k n_l n_m n_n \tilde{I}_{kl}\tilde{I}_{mn} \tag{2.140}$$

We thus transform (2.136) into:

$$\tilde{I}_{ij}^{TT2} = \tilde{I}_{ij}^2 - 2n_i n_k \tilde{I}_{ij}\tilde{I}_{jk} + \frac{1}{2}(n_i n_j \tilde{I}_{ij})^2 \tag{2.141}$$

In order to integrate equation (2.119) over the surface of a sphere, we need the identities:

$$\int n_i n_j d\Omega = \frac{4\pi}{3}\delta^i_j; \qquad \int n_i n_j n_k n_l d\Omega = \frac{4\pi}{15}[\delta^i_j\delta^k_l + \delta^i_k\delta^j_l + \delta^i_l\delta^j_k] \tag{2.142}$$

We thus find that the energy loss due to gravitational waves goes as the square of the third time derivative of the quadrupole moment tensor (to leading order - see [11]):

$$\begin{aligned}\dot{E} &= -\frac{1}{32\pi}\int \langle \bar{h}^{TT}_{ij,t}\bar{h}^{TT}_{ij,t}\rangle r^2 d\Omega \\ &= -\frac{1}{8\pi}\int \langle \partial^3_t \tilde{I}^{TT}_{ij}\partial^3_t \tilde{I}^{TT}_{ij}\rangle d\Omega \\ &= -\frac{1}{5}\langle \dddot{\tilde{I}}_{ij}\dddot{\tilde{I}}_{ij}\rangle \end{aligned} \tag{2.143}$$

2.10 Angular Momentum Loss Due to GWs in GR

For a binary in circular orbit the energy loss equation is enough to determine its secular decay (to lowest order), but if the binary retains some eccentricity then we also need to calculate the rate at which angular momentum is lost due to the gravitational waves. Following Peters [86], we can also use equation (2.117) to derive:

$$\frac{dL_i}{dt} = -\frac{d}{dt}\epsilon_{ijk}\int x_j S_{0k} dV = -\epsilon_{ijk}\int x_j S_{kl} n^l r^2 d\Omega \tag{2.144}$$

where at large r $S_{\alpha\beta}$ is only composed of $t_{\mu\nu}$, i.e. the products of the derivatives of the metric perturbation h. We can't use the $t_{\mu\nu}$ evaluated to the same order as before since this gives:

$$-\epsilon_{ijk}\int \frac{x_j x_l x_k x_m}{r^3} h_{\alpha\beta,4}\bar{h}_{\alpha\beta,4} r^2 d\Omega \tag{2.145}$$

which equals zero due to the antisymmetry of ϵ_{ijk}.

Peters [86] calculates the higher order terms in $t_{\mu\nu}$, giving:

$$\frac{dL_i}{dt} = -\frac{\epsilon_{ijk}}{32\pi G}\int d\Omega_m x_j[h_{\alpha\beta,k}\bar{h}_{\alpha\beta,m}$$
$$-2\bar{h}_{\alpha\beta,k}\bar{h}_{m\alpha,\beta} - 2\bar{h}_{\alpha\beta,m}\bar{h}_{k\alpha,\beta}] \tag{2.146}$$

He then evaluates the derivatives of h out to order $1/r^2$:

$$\begin{aligned}
\bar{h}_{\mu\nu,k} &= -\frac{x_k}{r}\bar{h}_{\mu\nu,0} - \frac{x_k}{r^2}\bar{h}_{\mu\nu} \\
\bar{h}_{0m,k} &= -\frac{n_k}{r}\bar{h}_{0m} - n_k\bar{h}_{0m,0} - \frac{1}{r}\bar{h}_{mk} + \frac{n_m n_j}{r}\bar{h}_{jk} \\
\bar{h}_{00,k} &= -\frac{n_k}{r}\bar{h}_{00} - n_k\bar{h}_{00,0} - \frac{n_k n_m n_q}{r}\bar{h}_{mq} \\
&\quad + \frac{n_k n_m}{r}\bar{h}_{om} - \frac{1}{r}\bar{h}_{0k} + \frac{n_m}{r}\bar{h}_{mk}
\end{aligned} \tag{2.147}$$

Using these expressions we can transform (2.144) into:

$$\frac{dL_i}{dt} = \frac{\epsilon_{ijk}}{8\pi}\int d\Omega\left[6n_j n_p\frac{d^2Q_{mk}}{dt^2}\frac{d^3Q_{mp}}{dt^3}\right]$$
$$+\left[-9n_j n_m n_p n_q\frac{d^2Q_{mk}}{dt^2}\frac{d^3Q_{pq}}{dt^3} + 4n_j n_m\frac{d^2Q_{mk}}{dt^2}\frac{d^3Q_{pp}}{dt^3}\right] \tag{2.148}$$

If we use the same surface integrals introduced in the previous section then this reduces to (transforming from Q to $\bar{I}$ notation):

$$\frac{dL_i}{dt} = -\frac{2}{5}\epsilon_{ijk}\langle\partial_t^2\tilde{I}_{mj}\partial_t^3\tilde{I}_{mk}\rangle \tag{2.149}$$

See [11] for further details.

Equations (2.143) and (2.149) can be evaluated for a binary that is in Keplerian orbit (to lowest order), with masses m_1 and m_2 and semi-major axis a and eccentricity e. The details of this calculation are given in the similar case of Nordström's theory in chapter 4. Peters and Mathews (see [85] and [86]) found the averaged rate of energy loss in general relativity is:

$$\langle \dot{E} \rangle = -\frac{32 m_1^2 m_2^2 (m_1 + m_2)}{5a^5 (1 - e^2)^{7/2}} \left[1 + \frac{73}{24} e^2 + \frac{37}{96} e^4 \right] \tag{2.150}$$

and the rate of angular momentum loss is:

$$\langle \dot{L}_z \rangle = -\frac{32 m_1^2 m_2^2 (m_1 + m_2)^{1/2}}{5a^{7/2} (1 - e^2)^2} \left[1 + \frac{7}{8} e^2 \right] \tag{2.151}$$

We now have a general framework for calculating the rate of energy and angular momentum loss in Nordström's theory. We first need to construct an energy-momentum complex that follows a flat space conservation law. In the case of general relativity we need to build a stress energy pseudotensor $t^{\mu\nu}_{,\nu}$ which follows $t^{\mu\nu}_{,\nu} = 0$. We use this instead of the regular stress energy tensor, since it obeys $T^{\mu\nu}_{;\nu} = 0$ which involves connection coefficients which spoil the conservation laws. For Nordström's theory we use the total stress energy tensor, made available by the flat background geometry.

The divergence of the appropriate stress energy tensor can be used to express the rate of loss of energy and momentum on a shell S^2 at large radius (in the radiation zone). This expression will generally depend on the square of the derivatives of the field. We will then need an expression for the field, which we find by using Green's functions which are then split up in a multipole expansion. One needs to determine the lowest order multipoles that radiate by taking into consideration conservation laws, and then integrate the field derivative terms over S^2, giving the total energy and angular momentum loss.

One can then apply the derived formulas for a binary in Keplerian orbit. As it turns out, alternative theories of gravitation don't necessarily reduce to Keplerian orbits when the stars are compact due to the presence of Nordtvedt effects. Indeed, this is one of the main reasons we chose to use Nordström's theory, as it has no lowest order Nordtvedt effect, and thus even very compact bodies move on Keplerian orbits to lowest order. Having confirmed this in calculation, we then apply expressions equivalent to (2.143) and (2.149) (as derived for Nordström's theory) to a binary, and find the rate at which its orbit decays. The functional form we find for the inspiral is quite similar to the expression we derive in general relativity, differing only in the constants. This calculation is described in chapter 4.

Chapter 3

Numerical Relativity

3.1 Introduction

Numerical relativity is a crucial technique for allowing us to understand the consequences of general relativity. It allows us to study the behavior of complex astrophysical environments, where the lack of symmetry precludes analytic solutions and the strong gravitational fields prevent the convergence of perturbative techniques.

The field arose in the 1960s and 70s as computers powerful enough to make it possible became available. Some of the pioneers are Hahn and Lindquist [90], Smarr [91], Eppley [92] who studied black hole spacetimes, and Wilson [93] who applied numerical techniques to neutron stars. The field has grown considerably since then, with discoveries being made in a wide range of sub fields, from critical behavior in general relativity ([94] [95]), to elucidations of the structure of singularities [96], and accurate models of colliding neutron stars [97].

We will focus here on applying numerical relativity to the two body problem. It is first necessary to rewrite Einstein's equations in a form that can be implemented on a computer. We use the Arnowitt-Deser-Misner (ADM) decomposition to this end, as described in the next section. The ADM equations then need to be modified into a form that gives accurate initial data for a Cauchy evolution, and then configured to be stable during the evolution. Effective modifications to these ends are described in the following sections. Many good reviews of numerical relativity are available – for general reviews see [98], [99], [100], [101], for in depth discussion of initial data see Cook: [102], methods for numerical hydrodynamics in both special and general relativity are given in: [103] [104], early binary neutron star coalescence work can be found in [105], and a review of hyperbolic methods is given by [106]. Note that numerical relativity is a quickly moving field, and we will discuss recent advancements such as the moving punctures method which is not included in these reviews.

3.2 ADM 3+1

The general prescription for numerically solving for the structure of spacetime was developed by Arnowitt, Deser and Misner (see [107], and also [11], [108], [109], [110]). In general relativity the structure of spacetime is contained in a 4 dimensional manifold $\mathcal{M}$ which can be described by a metric $g_{\mu\nu}$. Any one metric is not unique, as one can use many different coordinate systems and metrics to describe the same spacetime manifold $\mathcal{M}$. One of the advantages of the ADM scheme is that it neatly compartmentalizes this coordinate freedom. Following the ADM scheme we split the general 4 dimensional spacetime metric $g_{\mu\nu}$ into a stack of 3 dimensional spacelike hypersurfaces γ_{ij} and a timelike coordinate vectors n^{μ} that connects them. This allows us to numerically simulate the spacetime: we first generate an initial 3 dimensional spatial hypersurface, subject to some constraints, on a discrete volume grid in the computer. The geometry of this hypersurface will then be evolved forward in time.

The 3 dimensional hypersurface slices need to be spacelike – so that two events on any of the slices will have a spacelike separation: $ds^2 > 0$. Each slice will thus be labeled by a time parameter t, and the collection of slices $\{\Sigma_t\}$ is a foliation of the spacetime. The distance from one slice Σ_t to a nearby slice Σ_{t+dt} is described by the one form $\Omega = dt$, with the norm length defined as:

$$\|\Omega\|^2 \equiv g^{\mu\nu}\Omega_\mu\Omega_\nu \equiv -\alpha^{-2} \tag{3.1}$$

The positive function α is the lapse, and encapsulates one of the four coordinate degrees of freedom. It can then be used to define a unit-normalized one form n_μ

$$n_\mu = -\alpha\Omega_\mu \tag{3.2}$$

which can then be used to define a spatial projection operator:

$$\perp^{\mu}{}_{\nu} \equiv \delta^{\mu}{}_{\nu} + n^{\mu} n_{\nu} \tag{3.3}$$

In general a four-dimensional tensor **X** can be projected into a spacelike hypersurface via this operator, by using one projection operator per index of **X** . The shorthand notation for this is to place the index-less projection operator to the left of the tensor:

$$\perp X^{\alpha,\cdots}_{\beta,\cdots} = \perp^{\alpha}_{\gamma} \perp^{\delta}_{\beta} \cdots X^{\gamma,\cdots}_{\delta,\cdots} \tag{3.4}$$

For instance, $\perp n_{\nu} = \perp^{\mu}{}_{\nu} n_{\mu} = \delta^{\mu}{}_{\nu} n_{\mu} + n^{\mu} n_{\nu} n_{\mu} = n_{\nu} - n_{\nu} = 0$, so n^{μ} is orthogonal to the spatial slices, as expected. The projection of the $g_{\mu\nu}$ is the spatial metric $\gamma_{\mu\nu}$:

$$\begin{aligned} \gamma_{\mu\nu} \equiv \perp g_{\mu\nu} &= \perp^{\alpha}{}_{\mu} \perp^{\beta}{}_{\nu} g_{\alpha\beta} = \perp^{\alpha}{}_{\mu} (\delta^{\beta}{}_{\nu} g_{\alpha\beta} + n^{\beta} n_{\nu} g_{\alpha\beta}) \\ &= \perp^{\alpha}{}_{\mu} (g_{\alpha\nu} + n_{\alpha} n_{\nu}) = g_{\mu\nu} + n_{\mu} n_{\nu} \end{aligned} \tag{3.5}$$

and we have $n^{\mu}\gamma_{\mu\nu} = n^{\nu}\gamma_{\mu\nu} = 0$. We can also project out the timelike component of a tensor with the projection operator

$$N^{\alpha}_{\beta} = -n^{\alpha} n_{\beta} \tag{3.6}$$

We then define a spatial 3-covariant derivative D_{α} compatible with the spatial metric $\gamma_{\mu\nu}$ (so that we have $D_{\alpha}\gamma_{\mu\nu} = 0$, in analogy with the action of the regular covariant derivative on $g_{\mu\nu}$). For instance, acting on a spatial vector V^{μ}, D_{α} would be:

$$D_{\alpha} V^{\mu} \equiv \perp \nabla_{\alpha} V^{\mu} = \perp^{\beta}{}_{\alpha} \perp^{\mu}{}_{\nu} \nabla_{\beta} V^{\nu} = \perp^{\beta}{}_{\alpha} \perp^{\mu}{}_{\nu} V^{\nu}{}_{;\beta} \tag{3.7}$$

We next define the extrinsic curvature tensor:

$$K_{\mu\nu} = - \perp \nabla_\mu n_\nu \tag{3.8}$$

which effectively describes the velocities of the components of the spatial metric $\gamma_{\mu\nu}$. $K_{\mu\nu}$ and $\gamma_{\mu\nu}$ can be considered position and momentum conjugates in a Hamiltonian framework, and we need to specify both initially to evolve the second-order-in-time Einstein equations.

One constructs the initial data by first expressing the projections of Riemann tensor in terms of $K_{\mu\nu}$ and $\gamma_{\mu\nu}$, giving the Gauss equation:

$$\perp R_{\alpha\beta\gamma\delta} = {}^{(3)}R_{\alpha\beta\gamma\delta} + K_{\delta\beta}K_{\gamma\alpha} - K_{\gamma\beta}K_{\delta\alpha} \tag{3.9}$$

and the Codazzi equation:

$$\perp R_{\alpha\beta\gamma\hat{n}} = \perp R_{\alpha\beta\gamma\mu}n^\mu = D_\beta K_{\alpha\gamma} - D_\alpha K_{\beta\gamma} \tag{3.10}$$

where ${}^{(3)}R_{\alpha\beta\gamma\delta}$ is the Riemann tensor constructed from the spatial metric $\gamma_{\mu\nu}$, and we are using York's notation for contraction: $W_{\hat{n}} = W_\mu n^\mu, W^{\hat{n}} = -W^\mu n_\mu$. We then likewise define a density and current by projecting the stress energy tensor:

$$\rho_H = T_{\hat{n}\hat{n}} = T_{\mu\nu}n^\mu n^\nu \tag{3.11}$$

$$j^\mu = \perp T^{\mu\hat{n}} = - \perp (T^{\mu\nu}n_\nu) \tag{3.12}$$

These projections, along with contractions of the Gauss and Codazzi equations, allow us to derive the Hamiltonian constraint:

$${}^{(3)}R + K^2 - K_{ij}K^{ij} = 16\pi\rho_H \tag{3.13}$$

and the momentum constraint:

$$D_j K^{ij} - D^i K = 8\pi j^i \tag{3.14}$$

where ${}^{(3)}R$ is the 3-dimensional Ricci scalar, and $K \equiv \gamma_{ij} K^{ij}$ is the trace of K_{ij}. Equations (3.13) and (3.14) contain no time derivatives, and are thus constraints on the spatial slices $\gamma_{\mu\nu}$. The first equation is called the Hamiltonian constraint, and the second is the momentum constraint.

So far we have used one coordinate degree of freedom in specifying the lapse function α. In general when moving from one slice Σ_t to the next Σ_{t+dt} we can also have a spatial shift in the coordinate labeling, as would occur in a rotating coordinate system for instance. This coordinate freedom is contained in the shift vector β^μ. Thus an observer who is at rest in the coordinate system will move along a world line with a tangent vector given by:

$$t^\mu = \alpha n^\mu + \beta^\mu \tag{3.15}$$

with $\beta^\mu n_\mu = 0$.

We need to define a derivative along the tangent vector given in (3.15). The Lie derivative allows us to do this, where in general taking the Lie derivative of a tensor X^α_β along a vector field V^μ gives:

$$\mathcal{L}_V X^\alpha_\beta = V^\gamma \nabla_\gamma X^\alpha_\beta + X^\alpha_\gamma \nabla_\beta V^\gamma - X^\gamma_\beta \nabla_\gamma V^\alpha \tag{3.16}$$

with natural generalization to more indices.

Taking the Lie derivative along (3.15) allows us to produce an evolution equation for γ_{ij}:

$$\mathcal{L}_t \gamma_{ij} = -2\alpha K_{ij} + D_i \beta_j + D_j \beta_i \tag{3.17}$$

With the further projections of the stress energy tensor:

$$S_{\mu\nu} \equiv \perp T_{\mu\nu} \tag{3.18}$$

and

$$S \equiv \gamma^{ij} S_{ij} \tag{3.19}$$

we can also evolve the extrinsic curvature along (3.15):

$$\begin{aligned} \mathcal{L}_t K_{ij} = -D_i D_j \alpha + \beta^k D_k K_{ij} + K_{ik} D_j \beta^k \\ +K_{kj} D_i \beta^k + \alpha \left[{}^{(3)}R_{ij} - 2K_{ik} K^k{}_j + K_{ij} K \right] \\ -8\pi\alpha \left[S_{ij} - \frac{1}{2}\gamma_{ij}(S - \rho) \right] \end{aligned} \tag{3.20}$$

We next need to make some choices about our coordinate system, which will put the metric in the standard form and simplify the previous equations. We pick three spatial vectors e_i to form the basis of the spatial slice Σ, and the fourth basis vector to be equal to t^μ. Using these choices the metric can be put into form:

$$g_{\mu\nu} = \begin{pmatrix} -\alpha^2 + \beta_k \beta^k & \beta_i \\ \beta_j & \gamma_{ij} \end{pmatrix} \tag{3.21}$$

Raising the indices gives us:

$$g^{\mu\nu} = \begin{pmatrix} -\alpha^{-2} & \alpha^{-2}\beta^i \\ \alpha^{-2}\beta^j & \gamma^{ij} - \alpha^{-2}\beta^i\beta^j \end{pmatrix} \tag{3.22}$$

In addition the Lie derivative along t^μ becomes a simple partial derivative, so that (3.17) and (3.20) become:

$$\partial_t \gamma_{ij} = -2\alpha K_{ij} + D_i \beta_j + D_j \beta_i \tag{3.23}$$

and

$$\partial_t K_{ij} = -D_i D_j \alpha + \beta^k D_k K_{ij} + K_{ik} D_j \beta^k \tag{3.24}$$
$$+K_{kj} D_i \beta^k + \alpha \left[{}^{(3)}R_{ij} - 2K_{ik}K^k{}_j + K_{ij}K\right]$$
$$-8\pi\alpha \left[S_{ij} - \frac{1}{2}\gamma_{ij}(S - \rho)\right]$$

We now have the standard ADM equations and metric in hand, and we must solve them for a physically interesting system. In order to generate an evolution we must first solve for the initial data (3.13) and (3.14). This is described in the next sections, where modifications are made to clarify physical degrees of freedom in the equations. We must then evolve our spatial metric and extrinsic curvature forward in time, which requires a careful choice of lapse and shift, in addition to rewriting (3.23) and (3.24) in more stable forms. As we will need to consider the evolution of black hole spacetimes, we will also need to consider methods for dealing with horizons and singularities.

3.3 Einstein-Rosen Bridges

Before we construct further modifications of the ADM equations, we need to discuss the geometry of a black hole. Examining the Schwarzschild metric:

$$ds^2 = -\left(1 - \frac{2M}{R}\right) dt^2 + \left(1 - \frac{2M}{R}\right)^{-1} dR^2 + R^2(d\theta^2 + \sin^2\theta d\phi^2) \tag{3.25}$$

it first appears that a black hole has two regions: an external region (I) which extends from the horizon out to infinity $2M < R < \infty$ where it is asymptotically flat, and an internal region (II) between the singularity and the event horizon $0 < R < 2M$.

It turns out that eternal black holes are more complex than this however. Consider

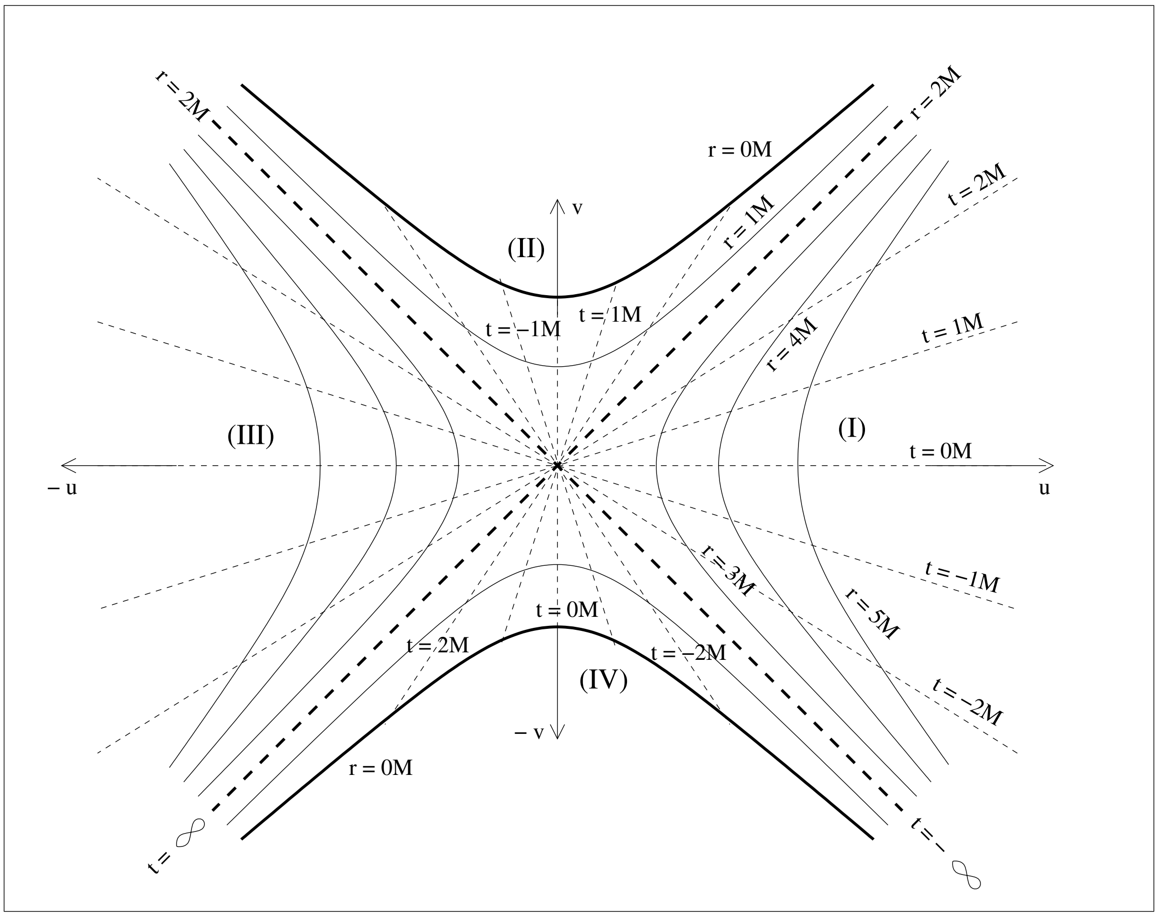

Figure 3.1: Kruskal-Szekeres mapping of a Schwarzschild Black Hole.

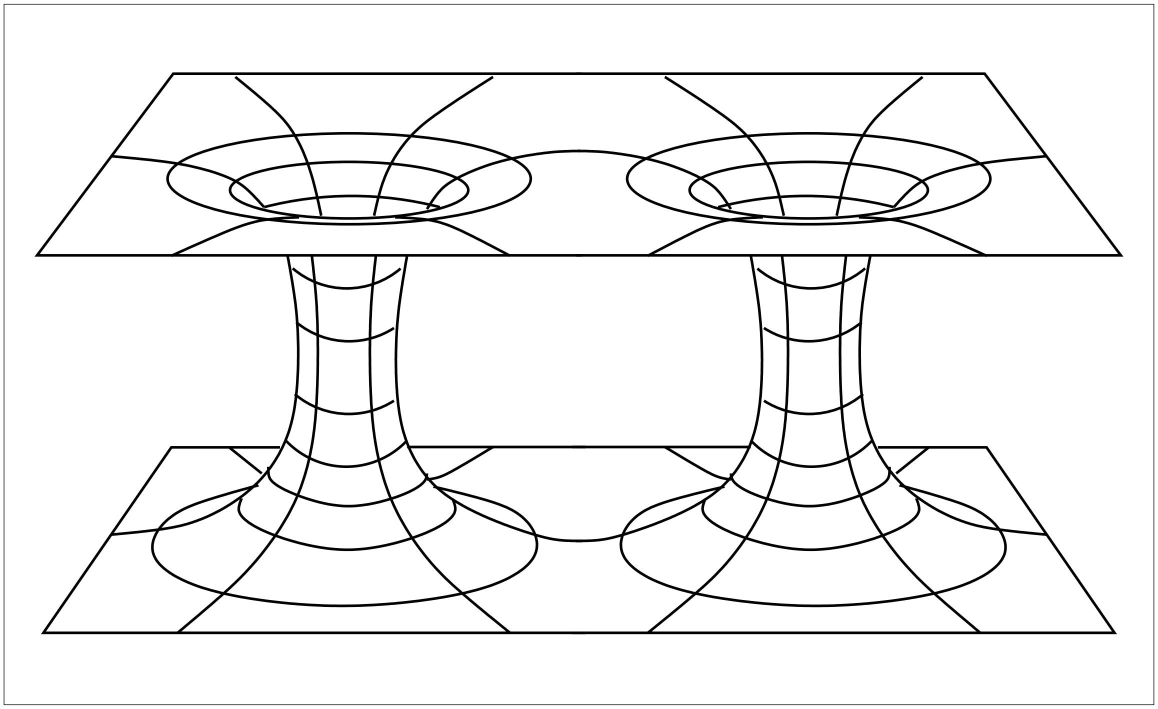

Figure 3.2: Wormholes connecting to the same second asymptotically flat universe.

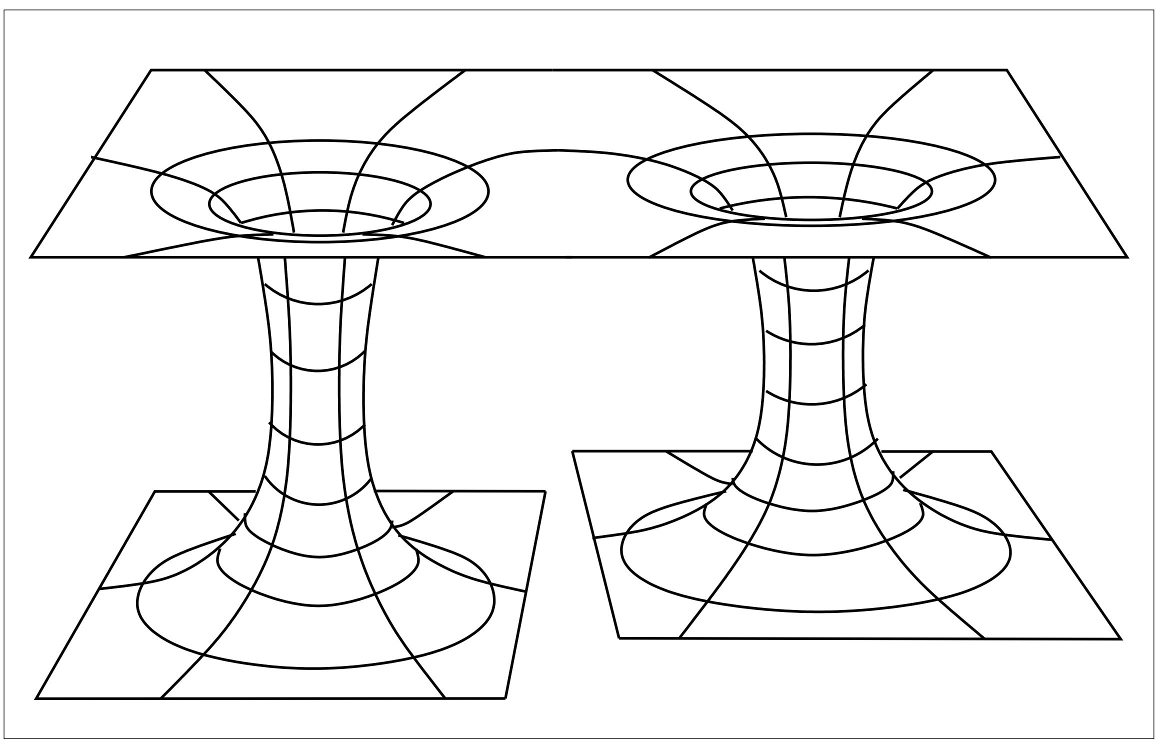

Figure 3.3: Wormholes connecting to different asymptotically flat universes.

the coordinate transformation to the Kruskal-Szekeres metric:

$$u = \pm \left(\frac{R}{2M} - 1 \right)^{1/2} e^{R/4M} \cosh\left(\frac{t}{4M}\right) \tag{3.26}$$

$$v = \pm \left(\frac{R}{2M} - 1 \right)^{1/2} e^{R/4M} \sinh\left(\frac{t}{4M}\right) \tag{3.27}$$

for $2M < R < \infty$, and

$$u = \pm \left(1 - \frac{R}{2M} \right)^{1/2} e^{R/4M} \sinh\left(\frac{t}{4M}\right) \tag{3.28}$$

$$v = \pm \left(1 - \frac{R}{2M} \right)^{1/2} e^{R/4M} \cosh\left(\frac{t}{4M}\right) \tag{3.29}$$

for $0 < R < 2M$. The $\pm$ signs correspond to two different regions in the resulting Kruskal-Szekeres – i.e. the eternal black hole spacetime contains two copies of the two regions (I) and (II) discussed before. The Kruskal-Szekeres metric is given by:

$$ds^2 = -\frac{32M^3}{R} e^{-R/2M}(dv^2 - du^2) + R^2 d\Omega^2 \tag{3.30}$$

where R is a function of u and v:

$$v^2 - u^2 = \left(1 - \frac{R}{2M}\right) e^{R/2M} \tag{3.31}$$

A diagram of the spacetime (suppressing angular directions) is given in figure (3.1) where u runs in the horizontal direction and v is vertical. Constant lines of R and t are plotted, and light rays travel on 45 degree lines. We again have region (I), the external, asymptotically flat region, and region (II), the internal region of the black hole, but there are two more regions: region (III), a second asymptotically flat universe which can also feed objects into (II), and region (IV), a white hole in the infinite past, from which objects can emerge into either (I) or (III) but never return.

Eternal Schwarzschild black holes thus have the very interesting feature in that they connect two asymptotically flat universes. Note that one can not travel between these two universes however as one is restricted to motion within the light cone, and thus all trajectories that cross the event horizon between regions (I) and (II) will be trapped in (II) and will hit the singularity at $R = 0$. However, we can make use of the bridge structure when we solve for the initial spatial metric Σ_0 and completely avoid the physical singularities while not excising any region of the spatial slice. We will do this by setting the initial data to be along the Einstein-Rosen bridge at $t = v = 0$ in figure (3.1). In fact we can set up several black holes in this same state, giving the Brill-Lindquist wormhole topology: [111]. We can furthermore configure the initial data such that the black holes have realistic momentum. We can thus put two black holes into a binary orbit, and in general create initial data for an arbitrary number of boosted black holes: [112]. Figure (3.2) shows the topology of a two black hole system where the black holes share the same second asymptotically flat universe, and figure (3.3) shows two black holes connecting to different asymptotically flat universes – both types can be constructed in the initial data. Furthermore we will show in the evolution section that we can pick lapse and shift conditions so that when the spatial metric and extrinsic curvature are evolved forward in time that they continue to avoid the central singularity.

As a demonstration we can transform the Schwarzschild metric into the ADM form given in (3.21), such that the Einstein-Rosen bridge is manifest. We make the coordinate transformation $R = \psi^2 r$ with

$$\psi = 1 + \frac{M}{2r} \tag{3.32}$$

and thus transform the metric into isotropic coordinates:

$$ds^2 = -\left(\frac{1 - \frac{M}{2r}}{1 + \frac{M}{2r}}\right)^2 dt^2 + \left(1 + \frac{M}{2r}\right)^4 (dr^2 + r^2 d\Omega^2) \tag{3.33}$$

This corresponds to (3.21) with lapse $\alpha = (1 - M/2r)(1 + M/2r)$, shift $\beta^i = 0$, and a conformally flat spatial metric $\gamma_{ij} = (1 + M/2r)^4 \eta_{ij}$. The event horizon occurs at $r = M/2$, so that $M/2 < r < \infty$ corresponds to universe (I) and $0 < r < M/2$ corresponds to universe (III). Thus the point $r = 0$ is a coordinate singularity and not a physical singularity, since this corresponds to distances infinitely far away from the throat at $r = M/2$ in region (III).

3.4 Initial Data

With our two wormhole goal in mind, we now need to solve the constraint equations (3.13) and (3.14). A common technique [113], [114], [115] involves splitting off a conformal component of the spatial metric:

$$\gamma_{ij} = \psi^4 \bar{\gamma}_{ij} \tag{3.34}$$

The power of 4 for the conformal field simplifies later equations, although other powers can be useful. In some cases it will be useful to assume conformal flatness, i.e.

$$\gamma_{ij} = \psi^4 \eta_{ij} \tag{3.35}$$

as was the case for the black hole described in isotropic coordinates.

We find that the spatial connection coefficients split into:

$$\Gamma^i_{jk} = \bar{\Gamma}^i_{jk} + 2(\delta^i_j \partial_k \ln \psi + \delta^i_k \partial_j \ln \psi - \bar{\gamma}_{jk} \bar{\gamma}^{il} \partial_l \ln \psi) \tag{3.36}$$

which gives us $\bar{D}_k\bar{\gamma}_{ij} = 0$ as for the general metric. The Ricci tensor splits into:

$$R_{ij} = \bar{R}_{ij} - 2(\bar{D}_i\bar{D}_j \ln\psi + \bar{\gamma}_{ij}\bar{\gamma}^{lm}\bar{D}_l\bar{D}_m \ln\psi) \tag{3.37}$$
$$+4((\bar{D}_i \ln\psi)(\bar{D}_j \ln\psi) - \bar{\gamma}_{ij}\bar{\gamma}^{lm}(\bar{D}_l \ln\psi)(\bar{D}_m \ln\psi))$$

and the Ricci scalar becomes:

$$R = \psi^{-4}\bar{R} - 8\psi^{-5}\bar{D}^2\psi \tag{3.38}$$

where $\bar{D}^2$ is the covariant Laplace operator:

$$\bar{D}^2 = \bar{\gamma}^{ij}\bar{D}_i\bar{D}_j \tag{3.39}$$

We also split the extrinsic curvature K_{ij} into its trace K and a traceless part A_{ij}:

$$K_{ij} = A_{ij} + \frac{1}{3}\gamma_{ij}K \tag{3.40}$$

Further modifications then give us either the transverse-traceless or thin-sandwich decompositions, which we can solve to get the initial data. In the transverse-traceless method we specify the spatial metric and the extrinsic curvature on an initial foliation Σ_0. In the thin-sandwich decomposition we instead (and physically equivalently) specify the spatial metric on two nearby slices Σ_0 and Σ_{0+dt}, and also combine the lapse α and shift β^j in to the constraint equations.

3.4.1 Conformal Transverse-Traceless Decomposition

Continuing with the transverse-traceless decomposition, we split off a conformal part of A^{ij}:

$$A^{ij} = \psi^{-10}\bar{A}^{ij} \tag{3.41}$$

which also gives $A_{ij} = \psi^{-2}\bar{A}_{ij}$

$\bar{A}^{ij}$ can be further split into its transverse-traceless and longitudinal components:

$$\bar{A}^{ij} = \bar{A}^{ij}_{TT} + \bar{A}^{ij}_{L} \tag{3.42}$$

with the transverse component being divergenceless:

$$\bar{D}_j \bar{A}^{ij}_{TT} = 0 \tag{3.43}$$

and the longitudinal component $\bar{A}^{ij}_{L}$ being derivable from a vector potential W^i:

$$\bar{A}^{ij}_{L} = \bar{D}^i W^j + \bar{D}^j W^i - \frac{2}{3}\bar{\gamma}^{ij}\bar{D}_k W^k \equiv (\bar{L}W)^{ij} \tag{3.44}$$

Using these new definitions the Hamiltonian constraint becomes:

$$8\bar{D}^2\psi - \psi\bar{R} - \frac{2}{3}\psi^5 K^2 + \psi^{-7}\bar{A}_{ij}\bar{A}^{ij} = -16\pi\psi^5\rho_H \tag{3.45}$$

and the momentum constraint is rewritten in terms of the vector potential W^i and vector Laplacian $\bar{\Delta}_L$:

$$(\bar{\Delta}_L W)^i - \frac{2}{3}\psi^6\bar{\gamma}^{ij}\bar{D}_j K = 8\pi\psi^{10} j^i \tag{3.46}$$

We need to choose $\bar{\gamma}_{ij}$, K, and $\bar{A}^{ij}_{TT}$ in order to solve for ψ in (3.45) and $\bar{A}^{ij}_{L}$ (via W^i) in (3.46). The equations will thus be highly simplified by picking a conformally flat background $\bar{\gamma}_{ij} = \eta_{ij}$, maximal slicing $K = 0$, and $\bar{A}^{ij}_{L} = 0$. If one solves for a black hole spacetime, then $\rho_H = j^i = 0$ as well. In fact if we further set the solution to be time symmetric so that $K_{ij} = -K_{ji} = 0$ then (3.45) reduces all the way to

$$\Delta^{flat}\psi = 0 \tag{3.47}$$

We can thus solve for ψ and find the same value as we did in isotropic coordinates (3.32): $\psi = 1 + M/2r$. Indeed, as (3.47) is linear, we can modify (3.32) to include more than one black hole:

$$\psi = 1 + \frac{M_1}{2|x^i - C_1^i|} + \frac{M_2}{2|x^i - C_2^i|} + \cdots \tag{3.48}$$

where C_n^i is the location of the n'th black hole. These black holes can be constructed to connect to the same asymptotically flat universes through their throats, or to separate ones as in figures (3.2) and (3.3).

In order to generate a binary system with two black holes in orbit we need to drop the time symmetric simplification $K_{ij} = -K_{ji} = 0$. $\bar{A}^{ij}$ will be nonzero in this case, so instead of solving for ψ we will first solve the momentum constraint (3.46). The Bowen-York approach still assumes maximal slicing and conformal flatness, and thus

$$(\bar{\Delta}_L^{flat} W)^i = 0 \tag{3.49}$$

can be solved by terms of the form:

$$W_{CP}^i = -\frac{1}{4r_c}(7P^i + n_C^i n_C^j P_j) \tag{3.50}$$

with $n_C^i = (x^i - C^i)/r$. We then solve for the extrinsic curvature and find:

$$\bar{A}_{CP}^{ij} = \frac{3}{2r_c^2}(P^i n_C^j + P^j n_C^i + (\eta^{ij} + n_C^i n_C^j) P_k n_C^k) \tag{3.51}$$

By plugging this solution into (3.53) we see that P^i in the linear momentum of the black hole. Then, since (3.49) is linear we can combine two terms of the form (3.50) to construct a binary black hole system. With the solution for $\bar{A}^{ij}$ in hand we can then go back and solve the Hamiltonian constraint (3.45).

On a side note, we need to define parameters such as the mass and momentum that describe our will binary, but these quantities are not well defined in the strong field region. We thus need to move out into the asymptotically flat region where the gravitational fields are slight perturbations in order to read off these quantities. We have the total (ADM) mass-energy:

$$M = -\frac{1}{2\pi} \oint_{\infty} \bar{D}^i \psi d^2 S_i \tag{3.52}$$

the linear momentum:

$$P^i = \frac{1}{8\pi} \oint_{\infty} \bar{K}^{ij} d^2 S_j \tag{3.53}$$

and the angular momentum (using Cartesian coordinates):

$$J_i = \frac{\epsilon_{ijk}}{8\pi} \oint_{\infty} x^j K^{kl} d^2 S_l \tag{3.54}$$

3.4.2 Thin Sandwich Decomposition

The conformal transverse-traceless decomposition gives the initial data for the spatial metric γ_{ij} and extrinsic curvature K_{ij} on one foliation Σ of the spacetime. The thin-sandwich decomposition (see e.g. [116]) gives an interesting alternative, as it specifies the spatial metric on two roughly close and parallel foliations. As opposed to the conformal transverse traceless decomposition, it also integrates conditions for the lapse and shift into the main equations. The main equations are given by:

$$\Delta^{flat}\psi = -\frac{1}{8}\psi^{-7}\bar{A}_{ij}\bar{A}^{ij} - 2\pi\psi^5\rho_H \tag{3.55}$$

$$(\Delta_L^{flat}\beta)^i = 2\bar{A}^{ij}\bar{D}_j(\alpha\psi^{-6}) + 16\pi\alpha\psi^4 j^i \tag{3.56}$$

$$\Delta^{flat}(\alpha\psi) = \alpha\psi\left(\frac{7}{8}\psi^{-8}\bar{A}_{ij}\bar{A}^{ij} + 2\pi\psi^4(\rho + 2S)\right) \tag{3.57}$$

The Laplacian and vector Laplacian are taken with respect to flat space. We thus have the Hamiltonian constraint for the conformal field ψ, a maximal slicing condition for the lapse α, and a minimal distortion condition for the shift β^i. We will discuss the maximal slicing and minimal distortion gauge choices more in the next section. We will likely include both of these gauge conditions into our code when we simulate binary inspirals in general relativity, and we already make use of a flat background in Nordström's theory, so this will be a tempting method to use in the future.

3.5 Evolution Techniques

Now that the initial data has been constructed we need to evolve our binary forward in time, and thus need to modify the ADM equations (3.23) and (3.24) into a stable form. One of the problems inherent in (3.24) is the presence of mixed derivative terms within ${}^{(3)}R_{ij}$. These terms prevent the equations from taking on a favorable hyperbolic wave equation form. In addition we need to pick a lapse and shift that will keep the evolution stable. We will focus on the BSSN method and moving punctures gauge choices here.

One alternative class of modifications are the hyperbolic formulations (for a review see [106]). Here the mixed derivative terms and the instabilities they cause are removed through the use of Lorentz type coordinate gauge – as was done in the Introduction to get a pure wave function for the metric perturbation. Pretorius (see [117] [118]) has developed a code that implements this technique to great effect: the code begins with two scalar field stars collapsing into black holes which then spiral into each other and merge.

The primary method we will consider here goes by BSSN, after its developers Baumgarte, Shapiro, Shibata and Nakamura (see [119], [120], [121], [122]). In this method we will construct secondary variables that replace the mixed partial derivative terms.

We define the fundamental variables in a similar form as before:

$$\phi = \frac{1}{12}\log\gamma \tag{3.58}$$

$$\tilde{\gamma}_{ij} = e^{-4\phi}\gamma_{ij} \tag{3.59}$$

$$K = \gamma^{kl}K_{kl} \tag{3.60}$$

$$\tilde{A}_{ij} = e^{-4\phi}\left(K_{ij} - \frac{1}{3}\gamma_{ij}K\right) \tag{3.61}$$

$$\tilde{\Gamma}^i = \tilde{\gamma}^{kl}\tilde{\Gamma}^i_{kl} \tag{3.62}$$

The conformal factor has been written in a slightly different form in (3.58) and (3.59). The main addition has been the introduction of the conformal connection function $\tilde{\Gamma}^i$ in (3.62). This is what allows us to rewrite the spatial Ricci tensor ${}^{(3)}R_{ij}$ without explicit reference to the mixed partial derivatives – and so we will need to provide a separate evolution equation for $\tilde{\Gamma}^i$. Note in some sense that we are just hiding the troublesome terms with $\tilde{\Gamma}^i$, and indeed the different formulations are equivalent analytically, but this version will allow for stable evolutions when small errors are introduced by the discretization process.

In the initial description of the ADM formalism, the constraint equations were solved for the first foliation Σ_0, and when the system is evolved forward in time the structure of the Einstein equations insures that the constraints will continue to be satisfied. However, we are free to go back and add the constraint equations into the evolution equations. We do this in the BSSN formulation to produce the following evolution equations:

$$
\begin{aligned}
\frac{d\phi}{dt} &= -\frac{1}{6}\alpha K && (3.63) \\
\frac{dK}{dt} &= -\gamma^{ij} D_j D_i \alpha + \alpha\left(\tilde{A}_{kl}\tilde{A}^{kl} + \frac{1}{3}K^2\right) && (3.64) \\
&+\frac{1}{2}\alpha(\rho + S) \\
\frac{d\tilde{\gamma}_{ij}}{dt} &= -2\alpha\tilde{A}_{ij} && (3.65) \\
\frac{d\tilde{A}_{ij}}{dt} &= e^{-4\phi}(-(D_i D_j \alpha)^{TF} + \alpha(R_{ij}^{TF} - S_{ij}^{TF})) && (3.66) \\
&+\alpha(K\tilde{A}_{ij} - 2\tilde{A}_{ik}\tilde{A}_j^k)
\end{aligned}
$$

and

$$
\begin{aligned}
\frac{d\tilde{\Gamma}^i}{dt} &= -2\tilde{A}^{ij}\alpha_{,j} && (3.67) \\
+2\alpha\left(\tilde{\Gamma}^i_{kl}\tilde{A}^{kl} - \frac{2}{3}\tilde{\gamma}^{ik}K_{,k} - \tilde{\gamma}^{ij}S_j + 6\tilde{A}^{ik}\phi_{,k}\right) \\
+\frac{\partial}{\partial x^j}\left(\beta^k\tilde{\gamma}^{ij}_{,k} - 2\tilde{\gamma}^{m(j}\beta^{i)}_{,m} + \frac{2}{3}\tilde{\gamma}^{ij}\beta^k_{,k}\right)
\end{aligned}
$$

where we have used the total time derivative d/dt:

$$
\frac{d}{dt} = \partial_t - \mathcal{L}_\beta \tag{3.68}
$$

To finish the evolution specification, we need to give conditions for the lapse. We consider a couple versions here.

3.5.1 Gaussian Normal Coordinates

The simplest choice for the lapse and shift is $\alpha = 1$ and $\beta^i = 0$, which certainly simplifies the evolution equations. However it is also a bad choice, as it leads to runaway growth in the equations. For instance the trace of the extrinsic curvature

K will grow without bound, and the coordinate tend to converge, giving rise to coordinate singularities – see e.g. [99].

3.5.2 Maximal Slicing

As the trace of the extrinsic curvature blows up with the simplest coordinate conditions, an alternative is to choose conditions designed to enforce that it doesn't blow up, i.e. set $K = \partial_t K = 0$. This leads to maximal slicing condition for the lapse function. An elliptic version of this condition is given by:

$$D^2\alpha = \alpha K_{ij}K^{ij} \tag{3.69}$$

(valid in vacuum), however elliptic equations are slow to solve and so we can construct diffusion type equations that converge to (3.69). With maximal slicing one can show that the divergence of the normal vectors $\nabla_\alpha n^\alpha$ is zero, and the coordinates thus avoid collapsing in towards the singularity, as opposed to the simple gauge choices $\alpha = 1$ and $\beta^i = 0$. This is very useful behavior, and we will utilize it shortly in the moving punctures section. For a modern view on maximal slicing see Riemann [123].

3.5.3 Minimal Distortion

We also need to find a condition for the shift that produces stability in the code we will develop in chapter 5. We saw before that the spatial metric could be split into an overall conformal factor, and the conformally reduced metric $\bar{\gamma}_{ij}$, which thus has 5 degrees of freedom. 2 of these degrees of freedom are due to gravitational waves, while the other 3 are bound in coordinate freedom. In minimal distortion we thus want to eliminate any coordinate fluctuations, only letting the two true degrees of freedom vary. This can be accomplished in a variety of ways. For instance one construct the conformal time derivative of the spatial metric:

$$u_{ij} \equiv \gamma^{1/3}\partial_t(\gamma^{-1/3}\gamma_{ij}) \tag{3.70}$$

Then setting the longitudinal components of u_{ij} equal to zero, and setting its overall divergence equal to zero gives us the minimal distortion condition for the shift vector:

$$(\Delta_L\beta)^i = 2A^{ij}D_j\alpha + \frac{4}{3}\alpha\gamma^{ij}D_jK + 16\pi\alpha j^i \tag{3.71}$$

Another similar method achieves the same ends by setting the time derivatives of the conformal connection functions equal to zero:

$$\partial_t\tilde{\Gamma}^i = 0 \tag{3.72}$$

These are also related to the minimal strain conditions, in which the rate of change of the spatial metric is minimized. This will generally give rise to a corotating reference frame [124], in which the stars move very little, and which is well adapted to the binary inspiral problem. Corotating reference frames were used in some of the first successful simulations (if short lived) of a binary black hole system, including evolving through an entire orbit: [125], and evolving through the plunge, merger, and ringdown: [126].

In our work to date we have used Nordström's theory, which only has a single scalar conformal field, so we don't use all of this formalism. We have however implemented what is essentially a shift vector that keeps our reference frame in sync with the angular motion of our sources, and used this to generate long stable inspirals. We thus plan to continue using this method when we adapt our techniques to general relativity.

3.5.4 Moving Punctures:

One of the best techniques to emerge recently is the moving puncture method. We saw earlier that we could solve for an entire spatial slice of a multi black hole spacetime by choosing the spatial slice to occur at $t = v = 0$. In this slice there are no physical singularities, and (phrasing things in terms of the isotropic coordinates (3.33)) after reaching the event horizon at $r = M/2$ the spatial slice spreads back out again in a mirror universe. The point $r = 0$ in the coordinates is the puncture, corresponding to the asymptotically flat infinite border of the mirror universe ($R \to \infty$ using the original Schwarzschild radius R). It would be nice to keep a structure similar to this as the spatial slices are evolved forward in time, such that they continue to avoid the future physical singularity of the black hole.

The original method [127], [128] developed to attempt this was to split ψ into the singular part and a regular function f:

$$\psi = \left(1 + \frac{M}{2r}\right) f \tag{3.73}$$

and then only evolve the regular function f, keeping the punctures in the same position as they were found in the initial data. This does not work well in practice however, especially in a binary inspiral, as the function f becomes highly twisted and distorted.

In the moving puncture method ψ is rewritten either as $\xi = \psi^{-4}$ (see [129]) or as $\phi = \ln \psi$ (see [130]) in order to remove the singular behavior in ψ (actually the ln version still diverges, but so slowly that it is no longer a problem). The entire field ξ or ϕ is then evolved, which allows the punctures and thus the black holes to move in the grid (see [131] [132]). By choosing one of two popular lapse gauge choices (1 +

log slicing [133]):

$$\partial_t \alpha = -2\alpha K \tag{3.74}$$

$$\partial_t \alpha = -2\alpha K + \beta^i \partial_i \alpha \tag{3.75}$$

and one of the $\tilde{\Gamma}$ freezing conditions [134]:

$$\partial_t \beta^i = \frac{3}{4} B^i \tag{3.76}$$

$$\partial_t B^i = \partial_t \tilde{\Gamma}^i - \eta B^i \tag{3.77}$$

we can show that the fields ξ or ϕ remain stable through the evolution.

The structure of the punctures changes however. Originally in the initial data (again referring to the isotropic coordinates) the field ψ diverged as $1/r$ as r approached 0, which is equivalent to approaching the infinite border in the mirror universe $R \to \infty$. As the fields evolve, ξ or ϕ can be converted back into ψ, and we then see that at late times ψ diverges as $1/\sqrt{r}$ as $r \to 0$, which corresponds to the puncture ending on a Schwarzschild radius of about $R = 3M/2$ (with the coefficient depending on the precise gauge condition used). The inner boundary is thus inside the event horizon, but continues to avoid the singularity for all times.

3.6 Our Primary Numerical Methods

We have described the general forms of Einstein's equations used in numerical simulations of binary black hole systems. Our current general goal is to build a code that evolves black hole binaries through the late inspiral and merger phases by making use of moving punctures and a corotating spherical coordinate system. As noted before, we have decided to first model Nordström's simpler relativistic theory of gravitation as a stepping stone towards this goal. Many of the techniques we have used to successfully simulate binary inspirals in Nordström's theory will carry over to general relativity, but perhaps not all.

The use of a corotating reference frame (see [124]) forms the nucleus of our numerical line of attack. As noted in the previous subsection on minimal distortion, this greatly reduces the dynamical motion within the grid, which serves to greatly reduce the degree to which spurious field excitations are produced. Indeed we can see that there is progressively more noise in our simulation as we model binaries with successively more eccentric orbits, since the stars will still move a considerable amount radially for highly eccentric orbits. This can generate a moderate amount of spurious excitations for highly eccentric orbits, but in the low eccentricity and quasi-circular binaries (which we are primarily interested in) there is very little noise.

A corotating reference frame then combines naturally with a spherical coordinate system. Spherical coordinate systems have several nice features. They naturally have a high density of mesh points near the origin, where they are needed to resolve the high curvature potential wells of the compact bodies. This thus provides an alternative to the adaptive mesh refinement techniques (see e.g. [135]) that other groups have found necessary to resolve the wells. They also have a smooth, corner-less S^2 outer boundary, which reduces the amount of artificial outgoing wave reflection. They also allow the general 3+1 problem to be split into a set of 1+1 differential equations, which can be evolved with stable implicit finite difference methods. One can also make use of the Weak Radiation Reaction approximation for quasi-circular orbits, and thus change the differential equations into a Schödinger equation like form, thus improving its numerical stability.

The wormhole initial data and moving punctures methods provide a compelling framework to model evolving black hole systems without excision while still avoiding the singularities. We have been using Nordström's theory to date and the spacetime structure of black hole-like objects is not presently clear in this theory. We thus use very compact bodies as the sources of the gravitational fields in our theory. Since tidal distortions of bodies only cause small changes to their geodesic motion, we furthermore make use of the hydro-without-hydro approximation [89], so that the stars retain the same structure in the binary as they have when isolated, and only their bulk motion is changed over the evolution. This works quite well in our simulation, and so it is not clear if we will continue to use it when modeling general relativity, or alternatively use the equally tempting moving puncture method. We discuss the form of the equations we use, and the numerical implementation of them, in chapter 5, and in greater detail in chapter 6.

Chapter 4

Binary Inspirals in Nordström's 2nd Theory: Semi-Analytic Calculations

4.1 Introduction

One of the first predictions of general relativity was found by Einstein only a year after he developed the main theory: the existence of gravitational waves in spacetime. By splitting the metric into a small perturbation $h_{\mu\nu}$ and a Minkowski background spacetime $\eta_{\mu\nu}$ one finds that the perturbation follows a wave equation: $\Box\bar{h}_{\mu\nu} = 8\pi T_{\mu\nu}$ (with $\bar{h}_{\mu\nu} = h_{\mu\nu} - (1/2)h$). However, the question of whether gravity waves actually carry energy was contentious for many decades after Einstein's original prediction – Einstein himself changed his mind on the issue (see e.g. [7]).

Over time the issue was resolved in favor of the waves being physical, and furthermore capable of being generated by bodies freely falling along geodesics. The resolution was helped the concept of general covariance: the waves do carry energy, but the energy can not be defined at individual points in spacetime (since coordinates can always be constructed such that spacetime is flat at those points), and instead needs to be averaged over an entire wavelength. By 1964 Peters and Mathews had calculated ([85],[86]) the energy and angular momentum carried by the waves emitted by a pair of stars in Keplerian orbit, which in turn results in the secular decay of the semi-major axis a and eccentricity e. Chandrasekhar found the same result by developing the post-Newtonian framework out to $2\frac{1}{2}$ order for extended fluid bodies [84]. This was dramatically confirmed by Hulse and Taylor's discovery [136] of the binary pulsar PSR B1913+16, whose orbit decays at the rate predicted by Peters and Mathews.

In our research we have determined that Nordström's second theory (see e.g. [137]) provides a good test bed for the development of numerical techniques to be used in relativistic binary simulations. We need analytical calculations to determine the rate at which a binary system's orbital parameters evolve in order to compare with the results from a numerical evolution of the binary. We thus perform a calculation in this paper similar to the one done by Peters and Mathews in order to find the rate at which semi-major axis a and eccentricity e change due to the emission of gravity waves for Nordström's theory. The method we develop follows the general procedure given by Will in chapter 10.3 of [88] for determining the gravitational radiation produced by alternative theories of gravitation. First we need show that two stars in Nordström's theory do in fact move in Keplerian orbit to lowest order, which is not true in all gravitational theories. We then calculate the energy radiated due to the gravity waves on a large two-sphere out in the radiation zone. This allows us to determine the rate at which a binary orbit decays.

4.2 Nordström's Second Theory

Following Einstein and Fokker's geometric description of the Nordström's theory we find that instead of the Einstein tensor being equated to the stress energy tensor we have instead the Ricci scalar being generated by the trace of the stress energy tensor:

$$R = 24\pi T \tag{4.1}$$

with the additional criteria that the theory is conformally flat:

$$C_{\alpha\beta\gamma\delta} = 0. \tag{4.2}$$

If we pick the metric to be of the form:

$$g_{\mu\nu} = (1+\varphi)^2\eta_{\mu\nu} \tag{4.3}$$

then we can expand (4.1) into:

$$\Box\varphi = 4\pi(1+\varphi)^3(\rho + \rho\varepsilon - 3p) \tag{4.4}$$

where we have used the standard perfect fluid stress energy tensor:

$$T^{\mu\nu} = [\rho(1+\varepsilon)+p]u^\mu u^\nu + g^{\mu\nu}p \tag{4.5}$$

We can also find a conserved energy-momentum complex, $t^{\mu\nu}$, which includes the energy contained in the field:

$$\begin{aligned} t^{\mu\nu} = \frac{1}{4\pi}\left[\eta^{\mu\alpha}\eta^{\nu\beta}\varphi_{,\alpha}\varphi_{,\beta} - \frac{1}{2}\eta^{\mu\nu}\eta^{\alpha\beta}\varphi_{,\alpha}\varphi_{,\beta}\right] \\ +(1+\varphi)^6 T^{\mu\nu} \end{aligned} \tag{4.6}$$

This stress energy tensor follows the flat space conservation law ${t^{\mu\nu}}_{,\nu} = 0$, which is made possible by the flat background metric $\eta_{\mu\nu}$. We will use this to calculate the energy flux in a later section.

A first post-Newtonian calculation performed in the next section reveals that Nordström's theory is fully conservative, with post-Newtonian parameters $\beta = 1/2$ and $\gamma = -1$. There is thus no lowest order Nordtvedt effect [138] in this theory (although the results given in the companion paper suggest that Nordtröm's theory violates the Strong Equivalence Principle at 2PN, which would give rise to higher order Nordtvedt effects). This allows us to utilize Keplerian orbits to calculate the quadrupole moment tensors, which are used to find the energy flux radiated by the system. The fact that the theory is fully conservative also allows for the usage of "Hydro-without-Hydro" approximation [89] since there are no "star-crushing" effects (see e.g. [139]). Therefore in an eccentric orbit the stars will not undergo radial pulsations, which in general can give rise to monopole radiation for scalar fields. This allows us to approximate the stars as point bodies in Keplerian orbit when finding the energy flux.

4.3 Binary Orbits to 1st PN Order

We will give a quick outline of the post-Newtonian calculations here. Following Will [88], we first determine the metric to 1 PN order (following chapter 4 of TEGP), and then calculate orbital motion (chapter 6 of TEGP).

4.3.1 The Metric to 1st PN Order

To make contact with Newtonian physics we only need to know the g_{00} component of the metric to v^2 order. To 1st post-Newtonian order we need to expand g_{00} to v^4, g_{i0} to v^3 and g_{ii} to v^2. We split φ into pieces that scale as the second and fourth powers of the velocity $\varphi = \varphi^{(2)} + \varphi^{(4)}$ (higher order corrections are not needed). This enables us to split (5.5) into:

$$\nabla^2\varphi^{(2)} = 4\pi\rho \tag{4.7}$$

and

$$-\partial_t^2\varphi^{(2)} + \nabla^2\varphi^{(4)} = 4\pi(3\varphi^{(2)}\rho + \rho\varepsilon - 3P). \tag{4.8}$$

Equation (4.7) has the solution

$$\varphi^{(2)} = -\int_V \frac{\rho(\mathbf{x}', t)}{|\mathbf{x} - \mathbf{x}'|} d^3x' = -U \tag{4.9}$$

where we use Will's definition of the Newtonian potential U.

To solve equation (4.8) first introduce the superpotential χ:

$$\chi = -\int_V \rho(\mathbf{x}', t)|\mathbf{x} - \mathbf{x}'| d^3x' \tag{4.10}$$

the Laplacian of which is related to U:

$$\nabla^2\chi = -2U \tag{4.11}$$

We thus find a solution for $\varphi^{(4)}$:

$$\varphi^{(4)} = \frac{1}{2}\partial_t^2\chi + 3\Phi_2 - \Phi_3 + 3\Phi_4 \tag{4.12}$$

where

$$\Phi_2 = \int \frac{\rho' U'}{|\mathbf{x} - \mathbf{x}'|} d^3x' \tag{4.13}$$
$$\Phi_3 = \int \frac{\rho' \Pi'}{|\mathbf{x} - \mathbf{x}'|} d^3x' \tag{4.14}$$
$$\Phi_4 = \int \frac{p'}{|\mathbf{x} - \mathbf{x}'|} d^3x' \tag{4.15}$$

We can also expand out $\partial_t^2\chi$:

$$\partial_t^2\chi = A + B - \Phi_1 \tag{4.16}$$

where

$$A = \int \frac{\rho'}{|\mathbf{x} - \mathbf{x}'|^3} (\mathbf{v}' \cdot (\mathbf{x} - \mathbf{x}'))^2 d^3x' \tag{4.17}$$
$$B = \int \frac{\rho'}{|\mathbf{x} - \mathbf{x}'|} (\mathbf{x} - \mathbf{x}') \cdot \frac{d\mathbf{v}'}{dt} d^3x' \tag{4.18}$$
$$\Phi_1 = \int \frac{\rho' v'^2}{|\mathbf{x} - \mathbf{x}'|} d^3x' \tag{4.19}$$

With $g_{\mu\nu} = (1 + \varphi^{(2)} + \varphi^{(4)})^2 \eta_{\mu\nu}$ we thus find:

$$\begin{aligned} g_{00} = -1 + 2U - U^2 - A - B + \Phi_1 \\ -6\Phi_2 + 2\Phi_3 - 6\Phi_4 \end{aligned} \tag{4.20}$$
$$g_{0i} = 0 \tag{4.21}$$
$$g_{ij} = \delta_{ij}(1 - 2U) \tag{4.22}$$

If we follow Will and transform into the Standard Post Newtonian gauge (with $\lambda_1 = -1/2$ and $\lambda_2 = 0$) then we find:

$$g_{00} = -1 + 2U - U^2 - 6\Phi_2 + 2\Phi_3 - 6\Phi_4 \tag{4.23}$$

$$g_{0i} = g_{i0} = 1/2(V_i - W_i) \tag{4.24}$$

$$g_{ij} = \delta_{ij}(1 - 2U) \tag{4.25}$$

where V_i and W_i are defined to be:

$$V_i = \int \frac{\rho' v'_i}{|\mathbf{x} - \mathbf{x}'|} d^3x' \tag{4.26}$$

$$W_i = \int \frac{\rho' \mathbf{v}' \cdot (\mathbf{x} - \mathbf{x}')(x - x')_i}{|\mathbf{x} - \mathbf{x}'|^3} d^3x' \tag{4.27}$$

By comparing to the PPN metric in Will we can see that $\gamma = -1, \beta = 1/2$ and all the other parameters are zero: $\xi = \alpha_1 = \alpha_2 = \alpha_3 = \zeta_1 = \zeta_2 = \zeta_3 = \zeta_4 = 0$.

Transforming to the Standard Post Newtonian gauge does not affect the equations of motion for circular orbits. This is because in transforming from our original coordinates to the Standard Post Newtonian gauge we subtract $-\chi_{,00}$ from g_{00} and add $\chi_{,0j}$ to g_{0j}. When we compute the connection coefficients we get need $g_{00,j}$ and $g_{0j,0}$, thus both gauges end up contributing $\chi_{,00j}$. In addition the coordinates are unchanged by the gauge transformation in circular orbits, where the velocity is orthogonal to the separation vector: $\mathbf{v} \cdot \mathbf{x}_{ab} = 0$.

4.3.2 Orbits to 1st PN Order

To calculate the equations of motion for the bodies we first need to introduce a useful variable: the conserved density ρ^* (which will also be useful later when we do a multipole expansion of φ). We define ρ^*:

$$\rho^* = \rho\sqrt{-g}u^0 = \frac{(1+\varphi)^3\rho}{\sqrt{1-v^2}} \tag{4.28}$$

which follows an "Eulerian" conservation rule:

$$\partial_t\rho^* = -\partial_i(\rho^* v^i) \tag{4.29}$$

This allows for the general rule:

$$(d/dt)\int_V \rho^* f d^3x = \int_V \rho^*(df/dt)d^3x \tag{4.30}$$

and allows us to define the conserved (baryon) mass:

$$m = \int_V \rho^* d^3x, \qquad \frac{dm}{dt} = 0 \tag{4.31}$$

We then define the center of mass for the a'th body to be:

$$x_a^j = \frac{1}{m_a}\int_a \rho^* x^j d^3x \tag{4.32}$$

The acceleration of the center of mass in the x^j direction is then:

$$\ddot{x}_a^j = \frac{1}{m_a}\int_a \rho^* \frac{dv^j}{dt} d^3x \tag{4.33}$$

We thus need an expression for $\rho^* dv^j/dt$ to use in (4.33). We act on the divergence of the stress energy tensor $T^{\mu\nu}{}_{;\nu} = 0$ with the projection operator $Q^\alpha_\mu = u^\alpha u_\mu + \delta^\alpha_\mu$ to this end:

$$Q^j_\mu T^{\mu\nu}{}_{;\nu} = \rho h u^\nu u^j{}_{;\nu} + Q^{j\nu}p_{,\nu} = 0 \tag{4.34}$$

with $h = 1 + \varepsilon + p/\rho$ (the relativistic specific enthalpy). Expanding this out we find:

$$\begin{aligned} \rho^* \frac{dv^j}{dt} = -\rho^* \Gamma^j_{\alpha\beta} v^\alpha v^\beta - (u^0)^{-1} \rho^* v^j \frac{du^0}{dt} \\ -(u^0)^{-2} \frac{\rho^*}{\rho h} Q^{j\nu} p_{,\nu} \end{aligned} \tag{4.35}$$

Expanding further and keeping only post-Newtonian terms we find:

$$\begin{aligned} \rho^* \frac{dv^j}{dt} = \rho^* U_{,j}[1 - v^2 + U] \\ + p_{,j}(-1 + 3U + \frac{1}{2}v^2 + \Pi + p/\rho^*) \\ -\frac{1}{2}\rho^*(V^j - W^j)_{,0} + v^j(\rho^* U_{,0} - p_{,0}) \\ +\rho^*[-3\Phi_{2,j} + \Phi_{3,j} - 3\Phi_{4,j}] \end{aligned} \tag{4.36}$$

After plugging (4.36) into (4.33) we find that most of the terms cancel. We find that the acceleration scales as:

$$\begin{aligned} \ddot{x}^j_a = -\frac{M_b x^j_{ab}}{r^3_{ab}} \left(1 + \frac{M_b}{r_{ab}} - v_a^2 - \frac{3}{2}\left(\frac{\mathbf{v}_b \cdot \mathbf{x}_{ab}}{r_{ab}}\right)^2\right) \\ + \frac{M_b(v^j_a - v^j_b)(\mathbf{v}_b \cdot \mathbf{x}_{ab})}{r^3_{ab}} \end{aligned} \tag{4.37}$$

where M_b is the gravitational mass of star b:

$$M_b = \int_b \rho^*(1 + (1/2)\bar{v}^2 - (1/2)\bar{U} + \varepsilon) d^3x. \tag{4.38}$$

We thus find that to lowest order the binary is in Keplerian orbit, with corrections that scale as M/r_{ab} coming in at first post-Newtonian order. Note that this is a non-trivial result. Individual terms in (4.36) would give rise to deviations from Keplerian orbits at lowest order. For instance, the ${V^j}_{,0}$ term evaluates to:

$$-\frac{1}{2m_a}\int_a \rho^* {V^j}_{,0} d^3x = -\frac{1}{2m_a}\int_a \rho^* U_a U_{b,j} d^3x \qquad (4.39)$$
$$\sim \frac{1}{2}\frac{M_b x^j_{ab}}{r^3_{ab}} U_a$$

which by itself would cause a constant deviation (proportional to U_a) from the Keplerian value for the acceleration, even for arbitrarily large separations. However, since this theory is fully conservative, the other terms in (4.36) precisely cancel out this one, and there is thus no Nordtvedt effect at 1PN order.

In the following section we calculate the lowest order contribution to energy loss due to radiation, which kicks in at quadrupole order. We will thus only use the lowest order contribution to the acceleration: $\ddot{x}^j_a = -M_b x^j_{ab}/r^3_{ab}$ (which gives rise to Keplerian orbits). However, if we were to calculate the energy loss to the next level of accuracy (which would include octupole terms) we would need to include the corrections in (4.37).

4.4 Calculation of Orbital Evolution

4.4.1 Energy Loss at Outer Boundary

In the first step of the calculation we find the energy radiated on a 2-sphere S^2 far out in the radiation zone. The key is provided by the energy-momentum complex $t^{\mu\nu}$ which follows the standard flat-space conservation law:

$${t^{\mu\nu}}_{,\nu} = 0. \qquad (4.40)$$

We can thus integrate $t^{00}{}_{,0} = -t^{0i}{}_{,i}$ inside the volume of the S^2:

$$\int t^{00}{}_{,0} d^3x = -\int t^{0i}{}_{,i} d^3x \tag{4.41}$$

or, using Gauss's law:

$$\partial_t E = -\int t^{0i} n_i dS. \tag{4.42}$$

We now need an expression for t^{0i}, which we get from equation (4.6):

$$t^{0i} = -\frac{1}{4\pi}\partial_t\varphi\partial_i\varphi. \tag{4.43}$$

$\partial_i\varphi$ can be transformed into $-n^i\partial_t\varphi$ since at large radius φ is approximately a spherical wave $\varphi \sim \sin(t-r)/r$. We thus find:

$$\partial_t E = -\frac{1}{4\pi}\int (\partial_t\varphi)^2 r^2 d\Omega \tag{4.44}$$

for the energy loss.

We now need an expression for $\partial_t\varphi$. We rewrite the equation of motion for the field (5.5) with the conserved mass density ρ^*:

$$\Box\varphi = 4\pi\rho^*(1-v^2)^{1/2}(1+\varepsilon-3p/\rho). \tag{4.45}$$

This can be solved via a Green's function:

$$\varphi = -\int \frac{[\rho^{*\prime}(1-(1/2)v'^2+\varepsilon'-3p'/\rho'+\mathcal{O}(v^4))]_{ret}}{|\mathbf{x}-\mathbf{x}'|} d^3x' \tag{4.46}$$

which is evaluated at the retarded time $t' = t - |\mathbf{x}-\mathbf{x}'|$. The $1/|\mathbf{x}-\mathbf{x}'|$ term can be expanded into:

$$\frac{1}{|\mathbf{x}-\mathbf{x}'|} = \frac{1}{r} + \frac{x^j x^{j\prime}}{r^3} + \ldots \tag{4.47}$$

We will only use the first term since we are working at large radius. Likewise the expansion:

$$r - |\mathbf{x} - \mathbf{x}'| = \frac{x^j x^{j'}}{r} + \frac{x^j x^k}{2r} \frac{(x^{j'} x^{k'} - r'^2 \delta^j_k)}{r^2} + \dots \tag{4.48}$$

will prove useful (again we just use the first term: $r - |\mathbf{x} - \mathbf{x}'| = x^j x^{j'}/r$). We now Taylor expand the numerator in (4.46) about $t-r$. Let $f(t', x') = f(t - |\mathbf{x} - \mathbf{x}'|, x') = [\rho^{*\prime}(1 - (1/2)v'^2 + \varepsilon' - 3p'/\rho' + \mathcal{O}(v^4))]_{ret}$, then:

$$f(t', x') = \sum_{n=0}^{\infty} \frac{1}{n!} \left[\frac{\partial^n}{\partial t'^n} f(t', x') \right]_{t'=t-r} \left(\frac{x^j x^{j'}}{r} \right)^n \tag{4.49}$$

Equation (4.46) can thus be expanded out in multipole moments:

$$\varphi = -\frac{1}{r} \left[M + n_i \partial_t D^i + \frac{1}{2} n_i n_j \partial_t^2 Q^{ij} + \dots \right] \tag{4.50}$$

with

$$M = \int \rho^{*\prime}(1 - (1/2)v'^2 + \varepsilon' - 3p'/\rho' + \mathcal{O}(v^4)) d^3x' \tag{4.51}$$

$$D^i = \int \rho^{*\prime}(1 - (1/2)v'^2 + \varepsilon' - 3p'/\rho' + \mathcal{O}(v^4)) x^{i\prime} d^3x' \tag{4.52}$$

$$Q^{ij} = \int \rho^{*\prime}(1 - (1/2)v'^2 + \varepsilon' - 3p'/\rho' + \mathcal{O}(v^4)) x^{i\prime} x^{j\prime} d^3x' \tag{4.53}$$

We need $\partial_t \varphi$ for equation (4.44), and thus need to calculate the time derivatives of the three multipole moments. Looking ahead we find that the quadrupole contribution $\partial_t^3 Q^{ij}$ scales as v^5, so we will drop all terms that are smaller than this. First we calculate the time derivative of the monopole:

$$\partial_t M = \int \rho^{*\prime} \frac{d}{dt} (1 - (1/2)v'^2 + \varepsilon' - 3p'/\rho') d^3x' \tag{4.54}$$

where we have used (4.30) to pass the time derivative through ρ^*. Note that if the two stars are on a quasi-circular orbit then the total time derivatives in the integrand are on the radiation reaction timescale, and thus contribute radiation at a far lower scale than v^5. They may contribute on elliptical orbits however. First we evaluate the $d\varepsilon/dt$ term, and to simplify we will pick $\Gamma = 2$, although the result holds in general. We find $\varepsilon = \kappa\rho = \kappa\rho^*(1 - (1/2)v^2 - 3\varphi + \mathcal{O}(v^4))$. We only keep $\varepsilon = \kappa\rho^*$ since this is already a higher order term. The term reduces to $d\varepsilon/dt = -\kappa\rho^*\partial_i v^i$. Thus any monopole radiation of order v^5 from the $d\varepsilon/dt$ term stems from the "breathing" motion as the star expands and contracts during the elliptical orbit. However, Nordström's second theory is fully conservative, and thus the stellar matter undergoes no "breathing" motion: the central density is constant to Post-Newtonian order. In fact, this justifies our use of the "Hydro-without-Hydro" assumption where we hold the stars to be rigid bodies throughout the evolution. Thus the entire $d\varepsilon/dt$ term does not contribute at v^5 order. The same holds for the $d(3p/\rho)/dt$ term. We thus find the monopole contribution to the radiation:

$$\partial_t M = -\frac{1}{2}\int \rho^{*\prime}\partial_t(v^{\prime 2})d^3x' + \mathcal{O}(v^7) \tag{4.55}$$

which enters in at v^5 order if the orbit is eccentric and is much smaller otherwise (note also that the total time derivative has been switched to a partial derivative since the velocity is now essentially constant throughout the star). It is also convenient that radial pulsations do not contribute at the order we are considering since this allows us to treat the stars as point bodies in later calculations.

We now calculate the contribution from the dipole via $\partial_t^2 D^j$. After applying two time derivatives we find:

$$\begin{aligned}\partial_t^2 D^j = \int \rho^{*\prime}[(1 - v^{\prime 2} + \varepsilon' - 3p'/\rho')\frac{dv^{j\prime}}{dt} \\ -\frac{d}{dt}\left(\frac{dv^{i\prime}}{dt}v^{i\prime}\right)x^{j\prime} - 2\frac{dv^{i\prime}}{dt}v^{i\prime}v^{j\prime}]d^3x'\end{aligned} \tag{4.56}$$

At first glance the $\int \rho^{*\prime}(dv^{j\prime}/dt)d^3x'$ term appears to contribute at v^4 order, but in fact the term is zero due to Newton's third law. Any corrections would enter at v^6 order at the soonest, and all the other terms in equation (4.56) also scale as v^6. Thus the dipole does not radiate to the order we are considering:

$$\partial_t^2 D^j = 0 + \mathcal{O}(v^6) \tag{4.57}$$

The final multipole moment we consider is the quadrupole. After similar calculations it reduces to:

$$\partial_t^3 Q^{ij} = \partial_t^3 \int \rho^{*\prime} x^{i\prime} x^{j\prime} d^3x' + \mathcal{O}(v^7) \tag{4.58}$$

Putting the terms together we find:

$$\partial_t E = -\frac{1}{4\pi}\int (\partial_t M + (1/2) n_i n_j \partial_t^3 Q^{ij})^2 d\Omega \tag{4.59}$$

for the rate of energy loss. With the integrals:

$$\int n_i n_j d\Omega = \frac{4\pi}{3}\delta^{ij} \tag{4.60}$$
$$\int n_i n_j n_k n_l d\Omega = \frac{4\pi}{15}[\delta^i_j \delta^k_l + \delta^i_k \delta^j_l + \delta^i_l \delta^j_k]$$

we finally find:

$$\partial_t E = -(\partial_t M)^2 - \frac{1}{3}\partial_t M \partial_t^3 Q^{ii} - \frac{1}{60}(\partial_t^3 Q^{ii})^2 - \frac{1}{30}(\partial_t^3 Q^{ij})^2. \tag{4.61}$$

This reduces to:

$$\partial_t E = -\frac{1}{30}(\partial_t^3 Q^{ij})^2. \tag{4.62}$$

for zero eccentricity, which is six times smaller than the value found in GR.

4.4.2 Angular Momentum Loss at Outer Boundary

We perform a similar calculation to find the rate at which the angular momentum decreases. With equation (4.40) and:

$$L_i = \epsilon_{ijk} \int x^j t^{0k} d^3x \tag{4.63}$$

we find that

$$\frac{dL_i}{dt} = -\epsilon_{ijk} \int x^j t^{kl}{}_{,l} d^3x = -\epsilon_{ijk} \int x^j t^{kl} n^l dS \tag{4.64}$$

The stress energy tensor components are:

$$t^{kl} = \frac{1}{4\pi} \partial_k \varphi \partial_l \varphi - \frac{1}{8\pi} \delta^k_l \eta^{\alpha\beta} \partial_\alpha \varphi \partial_\beta \varphi \tag{4.65}$$

Thus

$$\frac{dL_i}{dt} = -\frac{1}{4\pi} \epsilon_{ijk} \int x^j \partial_k \varphi \partial_l \varphi n^l dS. \tag{4.66}$$

The $\eta^{\alpha\beta}\partial_\alpha\varphi\partial_\beta\varphi$ term is zero due to the anti-symmetry of ϵ_{ijk}.

It is tempting at first to transform both of the spatial partial derivatives into time derivatives via $\partial_i \varphi = -n^i \partial_t \varphi$, but the resulting expression is zero due to the anti-symmetry of ϵ_{ijk}. We will thus only switch one of them into a time derivative:

$$\frac{dL_i}{dt} = -\frac{1}{4\pi} \epsilon_{ijk} \int x^j \partial_k \varphi \frac{1}{r} (\partial_t M + (1/2) n_a n_b \partial_t^3 Q^{ab}) dS. \tag{4.67}$$

while the other spatial derivative needs to be calculated out to higher order to find the first non-vanishing contribution (in fact, ϵ_{ijk} determines that it is the $\partial_k \varphi$ term that needs to be expanded to higher order, while the $\partial_l \varphi$ is approximated with the time derivative). When we apply ∂_k to (4.50) one of the terms we get is:

$$\partial_k \left(-\frac{1}{r} \right) M = \frac{x^k}{r^3} M. \tag{4.68}$$

However when we insert this term into (4.67) we get zero, again due to the anti-symmetry of ϵ_{ijk}, and in fact all the terms stemming from derivatives of powers of r are zero for the same reason. This leaves:

$$\partial_k \varphi = -\frac{1}{r^2}\partial_t D^k - \frac{x^c}{r^3}\partial_t^2 Q^{ck} \tag{4.69}$$

Examination of $\partial_t D^k/r^2$ shows that in general it is of order v^3/r. However, we work in the center of mass coordinate system so the lowest order contribution to this term is in fact zero, and lowest order that any corrections can appear is at v^5/r. In turn, the quadrupole term scales as v^4/r, therefore we will keep only it.

Equation (4.67) now becomes:

$$\frac{dL_i}{dt} = \frac{1}{4\pi}\epsilon_{ijk}\int n^j n^c \partial_t^2 Q^{ck}(\partial_t M + (1/2)n_a n_b \partial_t^3 Q^{ab})d\Omega. \tag{4.70}$$

Using the integrals (4.60) again we finally find:

$$\frac{dL_i}{dt} = \frac{1}{15}\epsilon_{ijk}\partial_t^3 Q^{jc}\partial_t^2 Q^{ck} \tag{4.71}$$

where the $\partial_t M$ term has dropped out, again due to ϵ_{ijk}. This expression is precisely one sixth of the value given by general relativity.

4.4.3 Application to Keplerian Orbits

We now apply the equations for the rates of energy (4.61) and angular momentum loss (4.71) to a binary star system in Keplerian orbit. The stars have gravitational masses m_1 and m_2, a semi-major axis a and eccentricity e. The separation d between the two stars is determined by the phase ϕ:

$$d = \frac{a(1-e^2)}{1+e\cos(\phi)} \tag{4.72}$$

which thus also gives the distances of the stars from the center of mass:

$$d_1 = \left(\frac{m_2}{m_1 + m_2}\right) d, \qquad d_2 = \left(\frac{m_1}{m_1 + m_2}\right) d. \tag{4.73}$$

The non-zero quadrupole moment components are:

$$\begin{aligned} Q_{xx} &= \mu d^2 \cos^2 \phi \\ Q_{yy} &= \mu d^2 \sin^2 \phi \\ Q_{xy} = Q_{yx} &= \mu d^2 \sin \phi \cos \phi \end{aligned} \tag{4.74}$$

with $\mu = m_1 m_2/(m_1 + m_2)$. Note also that for consistency we are expressing the Q_{ij} in terms of the gravitational mass instead of the rest mass $m^* = \int \rho^* d^3x$ as used in the previous section. Switching between the two involves corrections of order v^2 which do not affect our lowest order calculation. We need their second and third time derivatives for use in (4.61) and (4.71). Making use of the angular velocity:

$$\omega = \frac{[(m_1 + m_2)a(1 - e^2)]^{1/2}}{d^2} \tag{4.75}$$

we find the second derivatives to be:

$$\begin{aligned} \frac{d^2 Q_{xx}}{dt^2} &= -\gamma(4\cos(2\phi) + e(3\cos(\phi) + \cos(3\phi))) \\ \frac{d^2 Q_{yy}}{dt^2} &= \gamma(4\cos(2\phi) + e(4e + 7\cos(\phi) + \cos(3\phi))) \\ \frac{d^2 Q_{xy}}{dt^2} = \frac{d^2 Q_{yx}}{dt^2} &= -2\gamma \sin(\phi)(4\cos(\phi) + e(3 + \cos(2\phi))) \end{aligned} \tag{4.76}$$

where γ defined as:

$$\gamma = \frac{m_1 m_2}{2a(1-e^2)} \tag{4.77}$$

and third derivatives are:

$$\begin{aligned}
\frac{d^3 Q_{xx}}{dt^3} &= \beta(1+e\cos\phi)^2(2\sin 2\phi + 3e\sin\phi\cos^2\phi) \\
\frac{d^3 Q_{yy}}{dt^3} &= -\beta(1+e\cos\phi)^2(2\sin 2\phi + e\sin\phi(1+3\cos^2\phi)) \\
\frac{d^3 Q_{xy}}{dt^3} &= \frac{d^3 Q_{yx}}{dt^3} = \\
&-\beta(1+e\cos\phi)^2(2\cos 2\phi - e\cos\phi(1-3\cos^2\phi))
\end{aligned} \tag{4.78}$$

with β defined as:

$$\beta^2 = \frac{4m_1^2 m_2^2(m_1+m_2)}{a^5(1-e^2)^5}. \tag{4.79}$$

Finally we need $\partial_t M$. We have:

$$\partial_t M = -\frac{1}{2}(m_1\partial_t v_1^2 + m_2\partial_t v_2^2) = \frac{1}{2}\beta e\sin\phi(1+e\cos\phi)^2 \tag{4.80}$$

Putting the parts together we find:

$$\partial_t E = -\frac{1}{15}\beta^2(1+e\cos\phi)^4(4+2e^2+8e\cos\phi+2e^2\cos^2\phi) \tag{4.81}$$

and

$$\partial_t L_z = -\frac{2}{15}\beta\gamma(1+e\cos\phi)^3(8-2e^2+12e\cos\phi+6e^2\cos^2\phi) \tag{4.82}$$

In general relativity the energy can't be localized at individual points in space, and therefore the expressions for the dE/dt and dL_z/dt need to be averaged over an orbit. While the energy can be localized in Nordström's theory, we will also average (4.81) and (4.82) in order to compare with general relativity. This is valid since the orbital parameters change little over the span of an orbit (for moderately large separations). For the energy we average:

$$\langle \dot{E} \rangle = \frac{\int_0^T \dot{E} dt}{T} = \frac{\int_0^{2\pi} \dot{E}(dt/d\phi)d\phi}{\int_0^{2\pi}(dt/d\phi)d\phi} \tag{4.83}$$

and find:

$$\langle \dot{E} \rangle = -\frac{16}{15}\frac{m_1^2 m_2^2(m_1+m_2)}{a^5(1-e^2)^{7/2}}\left[1+\frac{13}{4}e^2+\frac{7}{16}e^4\right] \tag{4.84}$$

which compares to the value given by Peters [86] for general relativity:

$$\langle \dot{E} \rangle = -\frac{32}{5}\frac{m_1^2 m_2^2(m_1+m_2)}{a^5(1-e^2)^{7/2}}\left[1+\frac{73}{24}e^2+\frac{37}{96}e^4\right] \tag{4.85}$$

Likewise for the angular momentum we average to find:

$$\langle \dot{L}_z \rangle = -\frac{16}{15}\frac{m_1^2 m_2^2(m_1+m_2)^{1/2}}{a^{7/2}(1-e^2)^2}\left[1+\frac{7}{8}e^2\right] \tag{4.86}$$

which again is one sixth the value found in general relativity.

Finally, by using

$$a = -m_1 m_2/2E, \tag{4.87}$$

$$L^2 = m_1^2 m_2^2 a(1-e^2)/(m_1+m_2) \tag{4.88}$$

we can convert $\langle \dot{E} \rangle$ $\langle \dot{L}_z \rangle$ into $\langle \dot{a} \rangle$ and $\langle \dot{e} \rangle$:

$$\left\langle \frac{da}{dt} \right\rangle = -\frac{32}{15}\frac{m_1 m_2(m_1+m_2)}{a^3(1-e^2)^{7/2}}\left[1+\frac{13}{4}e^2+\frac{7}{16}e^4\right] \tag{4.89}$$

and

$$\left\langle \frac{de}{dt} \right\rangle = -\frac{18}{5}\frac{m_1 m_2(m_1+m_2)}{a^4(1-e^2)^{5/2}}e\left[1+\frac{7}{18}e^2\right] \tag{4.90}$$

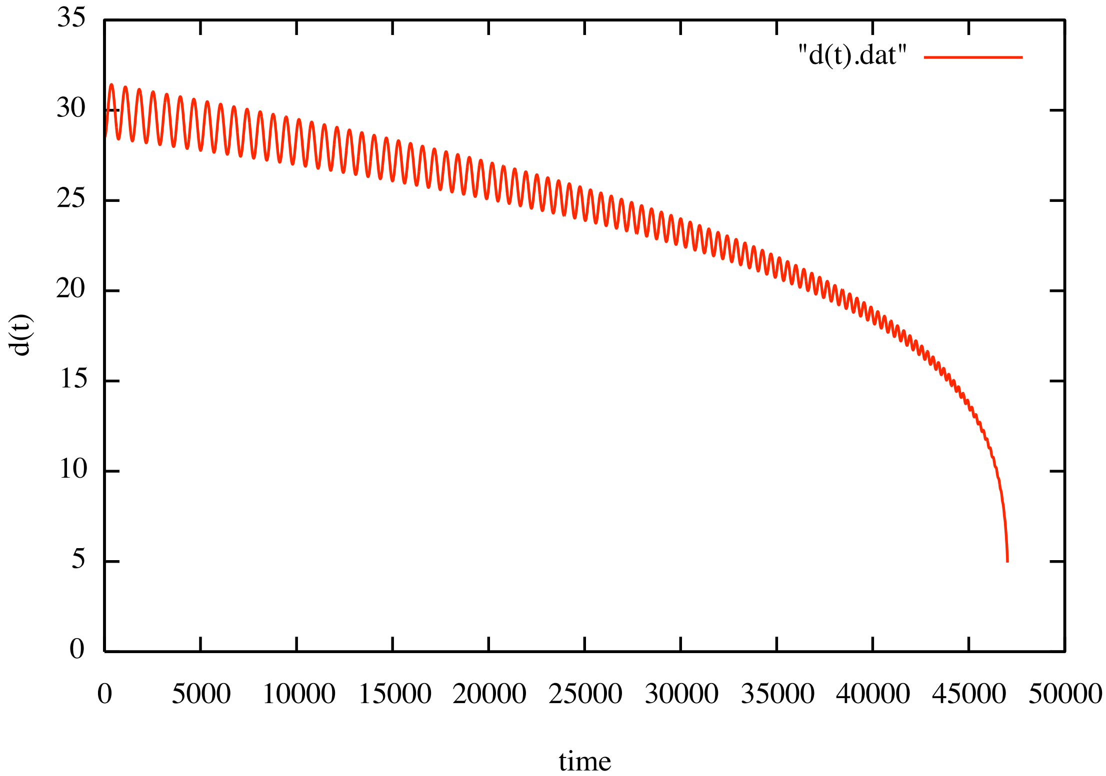

Figure 4.1: Binary separation as a function of time.

We can solve for $a(t)$ exactly for the special case $e = 0$. We find:

$$a(t) = \left(a^4(0) - \frac{128}{15} m_1 m_2 (m_1 + m_2) t\right)^{1/4} \tag{4.91}$$

[Note: maybe also add an equation for e(a) based on (4.89) and (4.90)].

An example orbital evolution based on equations (4.90) and (4.89) is shown in figure (4.1). The system is given an initial separation of $30M$ and an eccentricity of 0.05 and then evolved forward until merger. The overall profile of the inspiral is quite close to the expression given in (4.91) due to the low eccentricity. We also note that the orbit circularizes over time, as it does in general relativity. This inspiral can be compared to the numerical inspirals we describe in the companion paper. A plot of e as a function of a for a numerical inspiral as compared to the theoretical profile is given in figure (4.2).

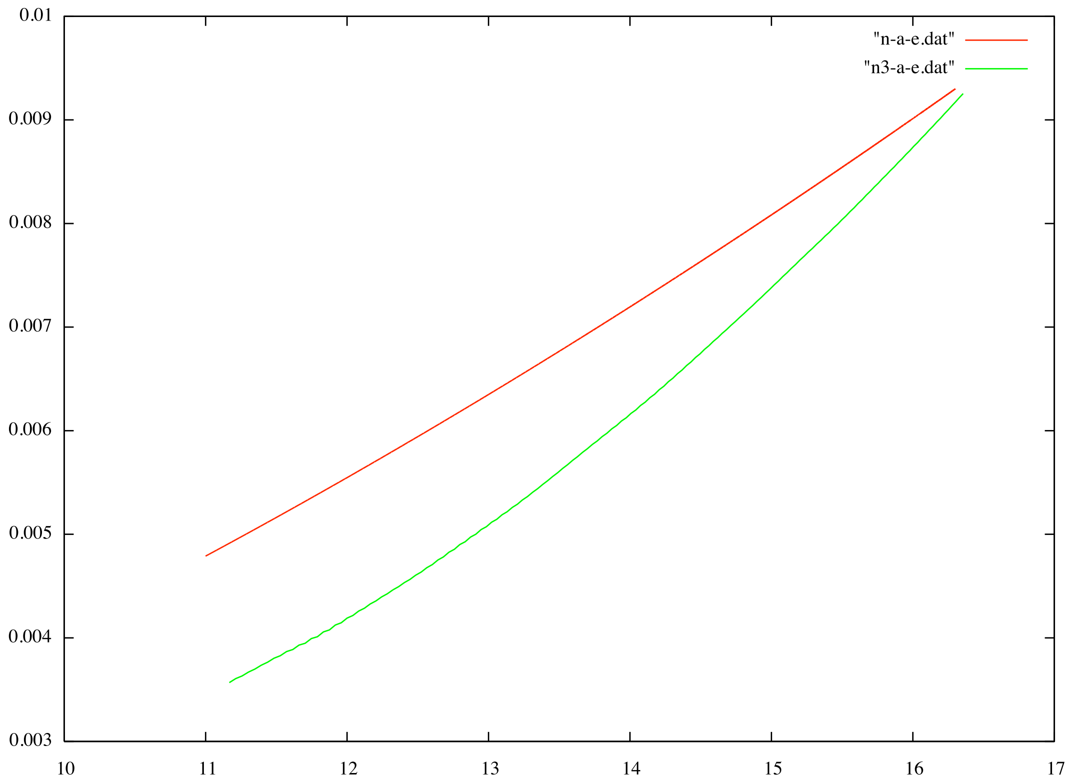

Figure 4.2: Eccentricity e as a function of semimajor axis a for a numerical inspiral and a theoretical inspiral with the same Keplerian parameters.

4.5 Conclusions

Nordström's second theory is a weak emitter of gravitational waves compared to general relativity, which is itself a weakly radiating theory. In the case of quasi-circular orbits, Nordström's theory radiates energy and angular momentum six times more slowly than in GR. This is somewhat surprising at first, since in general scalar theories can emit monopole radiation. This low radiative power is a reflection of the conservation laws that hold at lowest order, similar to those in GR, so that quadrupole level terms are the first to appear. As Will points out in [88], most alternative theories contain dipole radiation since they violate the Strong Equivalence Principle (SEP) and their gravitational and inertial masses differ. Nordström's theory likely also violates the SEP, but not at 1PN, so any Nordtvedt effects occur at high order.

As noted before, binary orbits will circularize over time in Nordström's theory. In our numerical simulations we thus place the stars in quasi-circular orbit and then evolve the system forward in time. The numerical techniques we have developed allow for long stable evolutions composed of many orbits. We compare the inspirals produced by the code to the predicted profiles given in (4.91) and find that they match to high accuracy. Thus the numerical and analytical methods mutually confirm each other. This success demonstrates that Nordström's theory is quite useful for developing numerical techniques to be used in numerical relativity. The next step is to apply the techniques developed and insight derived from Nordström's theory to the problem of binary inspirals in general relativity.

Chapter 5

Binary Inspirals in Nordström's 2nd Theory: Numerical Simulations

5.1 Introduction

Are astrophysical black holes correctly described by general relativity? It seems likely that they are, and yet it is healthy to maintain a "Trust but Verify" attitude [140]. The day when the relativity community announces either a dramatic confirmation of Einstein's theory or a very surprising discovery is surely not too far away. With LIGO doing science runs at design sensitivity we currently have a decent chance of detecting waves produced by a binary black hole merger, and advanced LIGO will make detection likely. There have also been exciting recent advances in the numerical simulation of binary black hole systems, with codes ([117], [129], [130]) now capable of simulating the inspiral, merger and ringdown of a binary system. There is good mutual agreement between these codes [141], and between them and Post-Newtonian calculations [142] and the particulars of using the simulated waveforms to extract signals from the interferometer data are being carefully considered [143].

We are designing our own numerical relativity techniques to complement and confirm the results of other groups. Our main goal is to use corotating spherical coordinate systems to simulate the late inspiral of comparable mass binaries. Spherical coordinate systems have several attractive features from a computational standpoint. A spherical mesh has a naturally high density of grid points near the origin where it is needed to resolve the high curvature potential wells of the compact bodies. This thus provides an alternative to the Adaptive Mesh Refinement methods which have seen success lately. Another nice feature of a spherical grid is that the outer boundary is S^2 which gives rise to less reflection of outgoing waves than a cubic grid. One of the key features is that it allows for the use of pseudo-spectral methods: by using spherical harmonics the 3+1 problem can be split into a set of 1+1 problems which can be solved with fast and accurate implicit methods. This also avoids the complications in directly finite differencing the angular directions θ and ϕ that arise due to the coordinate singularity at $r = 0$.

The final main element we use a corotating coordinate system, as proposed in [124]. This removes most of the dynamical motion in the grid, thus cutting down on the spurious field excitations.

We are currently supplementing our primary numerical method with some useful additional approximations. In order to avoid dealing with horizons and internal singularities for the time being we are using very compact massive bodies as the sources of the gravitational field. To additionally avoid modeling the complex fluid dynamics we further make use of the "Hydro-without-Hydro" approximation [89]. We first solve for the thermodynamic profiles of isolated polytropic stars. We then insert these profiles into a binary system, solving for the gravitational fields and the resulting bulk accelerations of the stars, while keeping their density profiles unchanged. This is a good approximation as geodesic deviations due to tidal distortions of the stars only arise at high post-Newtonian order.

Another useful approximation is possible when the stars are in quasi-circular orbit (as will usually be the case for astrophysical binaries since radiation reaction circularizes the orbit). As pointed out in [124], in the corotating coordinate system the binary now evolves at the slow radiation reaction time scale $\tau \sim d^4/M^3$ for binary separation d and mass M. This makes the Weak Radiation Reaction (WRR) approximation possible: the second time derivative can be dropped, thus changing the character of the differential equation that one solves.

There are some numerical drawbacks to using spherical coordinate systems. The primary one is that spherical decomposition and synthesis are computationally expensive. For instance the decomposition:

$$A_{lm}(r) = \int f(r, \theta, \phi) Y^*_{lm}(\theta, \phi) d\Omega \tag{5.1}$$

appears to be an $\mathcal{O}(N^5)$ calculation when discretized. However it can be reduced to a $\mathcal{O}(N^4)$ calculation by defining intermediate variables and splitting the integration into two steps. The computational cost is further reduced in our case as we only need decompose and synthesize in the small volumes containing our compact bodies. This makes it possible to run high resolution meshes in a reasonable amount of time.

There are some other subtle issues that arise in spherical coordinate systems. For instance it turns out that when computing the volume integrals of field derivatives very fine meshes are needed in order to converge to acceptable levels when using second order accurate methods. We find that using higher order methods in this case allows for accurate results with much lower resolution meshes. This is described in greater detail in section 3.

Before we implement these techniques in a full GR code we have decided to test them in a scalar gravity model theory (following the example of [144] and [145]). This forms the focus of this paper. After the tests are successful and the details of implementation are thoroughly understood we can then feel confident in applying them to a fully general relativistic code. After considering several scalar theories, we chose Nordström's second theory (see [137]). It is a fully conservative metric theory, with parameterized post-Newtonian parameters $\gamma = -1$, $\beta = 1/2$ and all others zero. Thus the theory has no Nordtvedt effect (see [138]), and the stars move on Keplerian orbits in the limit of small mutual gravitational potential. This is nontrivial since the Nordtvedt effect can produce considerable deviation from Keplerian orbits for highly compact bodies, even at arbitrarily large separations. Using Nordström's theory thus allows us to compare the orbital evolutions that our simulation produces to those that we find from a semi-analytical calculation presented in a companion paper.

The fully conservative nature of Nordström's theory has an additional benefit in that it also allows us to use the "Hydro-without-Hydro" approximation. This is valid since corrections to the star's equilibrium only show up after first post-Newtonian order for fully conservative theories as shown by [139].

In the following sections we first review Nordström's second theory, the basis for our model theory. We describe the construction of isolated stars in this theory, the equations of motion for the matter, and review the expected form of the inspiral based on the analytical calculations of the companion paper. Next we go over the numerical methods used to simulate the binary, including switching to a co-rotating reference frame, and several preliminary test cases needed to check the performance of the code. We finish with the results of simulating Nordström binaries in both quasi-circular and slightly eccentric orbits. We in general obtain nice agreement between the results from our simulation and the analytic calculations, but there are some subtle discrepancies. We now believe these are due to violations of the Strong Equivalence Principle (SEP) at 2PN order in Nordström's theory, which is perhaps not too surprising: all metric theories are expected to violate the SEP at some point except for general relativity.

5.2 Nordström's Second Theory

After the development of special relativity it became clear that Newton's gravitational theory could no longer be completely correct. For instance the Poisson equation is solved simultaneously throughout all space, thus the movement a massive body would allow for the instantaneous transmission of signals, in disagreement with the finite speed of light. Comparisons with electromagnetic theory suggested that the Laplacian operator should be replaced with the D'Alembertian wave operator. Gunnar Nordström used this idea to develop two relativistic scalar gravity theories a couple years before Einstein discovered General Relativity. Nordström's theories can not be correct - as Nordström quickly realized after Einstein presented his tensor theory. For instance, being conformally flat, they predict zero bending of light. However, they do provide an excellent test bed for developing tools for numerical relativity.

We utilize Nordström's second theory. The metric is conformally flat (i.e. the

Weyl tensor is zero: $C_{\alpha\beta\gamma\delta} = 0$) and is generated by a scalar field φ:

$$g_{\mu\nu} = (1 + \varphi)^2 \eta_{\mu\nu} \tag{5.2}$$

while the scalar field is generated in turn by the field equation involving the Ricci scalar and the trace of the stress energy tensor (see [137]):

$$R = 24\pi T \tag{5.3}$$

We pick the standard perfect fluid stress energy tensor:

$$T^{\mu\nu} = (\rho + \rho\varepsilon + p)u^\mu u^\nu + g^{\mu\nu} p \tag{5.4}$$

so the EOM for the field becomes:

$$\Box\varphi = 4\pi(1 + \varphi)^3(\rho + \rho\varepsilon - 3p) \tag{5.5}$$

Since Nordström's theory has the background geometry $\eta_{\mu\nu}$, a conserved energy-momentum complex can be constructed:

$$\begin{aligned} t^{\mu\nu} = \frac{1}{4\pi}\left[\eta^{\mu\alpha}\eta^{\nu\beta}\varphi_{,\alpha}\varphi_{,\beta} - \frac{1}{2}\eta^{\mu\nu}\eta^{\alpha\beta}\varphi_{,\alpha}\varphi_{,\beta}\right] \\ +(1+\varphi)^6 T^{\mu\nu} \end{aligned} \tag{5.6}$$

with ${t^{\mu\nu}}_{,\nu} = 0$. Nordström's theory has gravitational waves, although they are quite different from those in general relativity since $C_{\alpha\beta\gamma\delta} = 0$. Namely, the waves occur in the scalar field φ as described by equation (5.5), and they carry a localizable energy $t^{00} = (1/8\pi)[(\partial_t\varphi)^2 + (\nabla\varphi)^2]$.

5.2.1 Single Star Solution

We utilize the hydro-without-hydro approximation in our code. This is valid since tidal distortions of the stars do not affect the orbital dynamics until relatively high Post-Newtonian order. We thus need to construct a model of a single star in Nordström's theory to use as a source in the main code. For a single isolated star equation (4) becomes:

$$\frac{1}{r^2}\partial_r(r^2\partial_r\varphi) = 4\pi(1+\varphi)^3[\rho(1+\varepsilon) - 3p] \tag{5.7}$$

We will assume the star is a polytrope, so that the pressure and internal energy become:

$$p = \kappa\rho^\Gamma \tag{5.8}$$

$$\varepsilon = \frac{\kappa}{\Gamma - 1}\rho^{\Gamma-1} \tag{5.9}$$

which reduces equation (5.7) to two variables. We use the projection operator $Q^\alpha_\mu = u^\alpha u_\mu + \delta^\alpha_\mu$ on the divergence of the stress energy tensor $T^{\mu\nu}{}_{;\mu} = 0$ to get the second equation:

$$\rho h u^\nu u^\alpha{}_{;\nu} + Q^{\alpha\nu} p_{,\nu} = 0 \tag{5.10}$$

where h is the relativistic specific enthalpy: $h = h(\rho) = 1 + \varepsilon + p/\rho$. With $u^0 = 1/(1+\varphi)$ and $u^i = 0$ we can reduce this to:

$$\frac{d\varphi}{dr} = -\frac{(1+\varphi)}{h}\frac{dh}{dr} \tag{5.11}$$

We solve (5.7) and (5.11) iteratively. In the first iteration we drop the $(1+\varphi)^3$ and $(1+\varphi)$ terms respectively, and then solve essentially what is a modified Lane-Emden equation by specifying the central pressure ρ_c and integrating out. For successive iterations we then plug $(1+\varphi)^3$ and $(1+\varphi)$ back in, using the previous iteration's solution for φ. For values of ρ_c below some critical value (which depends on κ and Γ), the iterative process converges.

We use a stiff equation of state with $\Gamma = 2$ for our model stars, and find the most compact star we can form has radius $R \sim 1.75M$, which is smaller than the event horizon radius in classical GR, as well as being smaller than the Buchdahl-Bondi bound of $R = 9/4M$ for GR.

5.2.2 Matter Equations of Motion

Equation (5.5) tells us how the metric reacts to the matter, we thus need to find the equations of motion of the matter in response to the metric. To simplify matters we will utilize the "hydro-without-hydro" assumption, keeping the stars in the rigid profiles determined in the previous section, and only follow the motion of their center of masses. We follow Will (see [88]) and utilize the law of rest-mass conservation $(\rho u^\mu)_{;\mu} = 0$ to this end. We can define a "conserved density" ρ^*:

$$\rho^* = \rho(-g)^{1/2}u^0 = \rho\frac{(1+\varphi)^3}{\sqrt{1-v^2}} \tag{5.12}$$

which follows an "Eulerian" continuity equation:

$$\partial_t\rho^* + \partial_i(\rho^* v^i) = 0 \tag{5.13}$$

Thus for any function $f(\vec{x}, t)$ we have:

$$(d/dt)\int_V \rho^* f d^3x = \int_V \rho^*(df/dt)d^3x \tag{5.14}$$

and we get the total rest mass m_a for the particles in star a with the special case of $f = 1$:

$$m_a \equiv \int_a \rho^* d^3x, \qquad \frac{dm_a}{dt} = 0 \tag{5.15}$$

We use the total rest mass of star a to define its center of mass:

$$x_a^j = \frac{1}{m_a} \int_a \rho^* x^j d^3x \tag{5.16}$$

and then apply (5.14) twice to get the coordinate acceleration a_a^i of the center of mass of star a:

$$a_a^j = \frac{1}{m_a} \int_a \rho^* \frac{dv^j}{dt} d^3x \tag{5.17}$$

We need an expression for $\rho^* dv^j/dt$ which we find by expanding the projection of the divergence of the stress energy tensor (5.10):

$$\begin{aligned} \rho^* \frac{dv^j}{dt} = -\rho^* \Gamma^j_{\alpha\beta} v^\alpha v^\beta - (u^0)^{-1} \rho^* v^j \frac{du^0}{dt} \\ -(u^0)^{-2} \frac{\rho^*}{\rho h} Q^{j\nu} p_{,\nu} \end{aligned} \tag{5.18}$$

5.2.3 Analytical Orbits

The previous section found the equations of motion for the matter, (5.17) and (5.18), which we discretize in the numerical simulation in order to evolve the orbit of the Nordström binary. We also need analytical solutions for the orbits produced by this theory to compare with our numerical results. We show in the companion paper that the equations simplify greatly at first post-Newtonian order, and now restate the main results here.

Consider a binary with stars a and b in a slightly eccentric orbit with an angular velocity ω. Set things up so that the binary is instantaneously aligned along the x-axis of a Cartesian coordinate system, with a separation d and the bulk of the velocity in the $\hat{y}$ direction: $v_a^y \sim \omega d/2$, and a small amount of radial velocity v_a^x. The PN analysis then finds that acceleration $\ddot{x}_a$ of star a in the $\hat{x}$ direction is:

$$\ddot{x}_a = -\frac{M_b}{d^2}\left(1 + \frac{M_b}{d} - v_a^2 - \frac{3}{2}(v_b^x)^2 - (v_a^x - v_b^x)v_b^x\right) \tag{5.19}$$

where $M_b = \int_b \rho^*(1 + (1/2)\bar{v}^2 - (1/2)\bar{U} + \varepsilon)d^3x$ is the gravitational mass (equal to the inertial mass) of star b (with $\bar{U} = \int_b \rho' |\mathbf{x} - \mathbf{x}'|^{-1} d^3x'$ and $\bar{\mathbf{v}} = \mathbf{v} - \mathbf{v}_0$ where $\mathbf{v}_0$ is velocity of the center of mass). It is useful later to simplify this to:

$$\ddot{x}_a \sim -\frac{M_b}{d^2}\left(1 + \frac{1}{2}\frac{M_b}{d}\right) \tag{5.20}$$

which is valid for binaries with low eccentricity (or are in quasi-circular orbit), as we will consider. The acceleration in the $\hat{y}$ direction is:

$$\ddot{y}_a = \frac{M_b(v_a^y - v_b^y)v_b^x}{d^2} \tag{5.21}$$

At large separations the post-Newtonian corrections M_b/d and v_a^2 drop out, leaving the binary in a Keplerian orbit. Thus Nordström's second theory has no Nordtvedt effect (at 1PN order).

The second analytical calculation performed in the companion paper then determines the secular change in the binary orbit driven by radiation reaction. In general a scalar theory will admit monopole radiation, but Nordström's theory has conservation laws for mass and momentum, so in a circular orbit the quadrupole contribution to the radiation is dominant. Thus with the stars moving on Keplerian orbits (as found in the previous section) the rate of energy loss is $dE/dt = 32/(15d^5)$ (having set $M_a = M_b = 1$), which is six times smaller than in general relativity. This in turn gives the separation as a function of time:

$$d(t) = \left[d(0)^4 - \frac{256}{15} t \right]^{1/4} \tag{5.22}$$

Reproducing this 1/4 power law inspiral, similar to the expression found by Peters and Mathews for GR, is a major test of the Nordström simulation.

5.3 Numerical Methods

5.3.1 Co-rotating Coordinates and the Weak Radiation Reaction Approximation

We need to finite difference the main equation (5.5) for our numerical simulation. We start by transforming the wave equation $-\partial_t^2 \varphi + \nabla^2 \varphi$ into a corotating spherical coordinate system. We set up a coordinate transformation where $\bar{\phi} = \phi - \Omega(t)$ (with $\Omega(t) = \int_0^t \omega(t') dt'$ and t, r, and θ remaining unchanged) so that $\omega(t)$ instantaneously matches the binary's angular velocity. The differential equation thus changes to (dropping the bar notation):

$$\begin{aligned} -\partial_t^2 \varphi + \dot{\omega} \partial_\phi \varphi + 2\omega \partial_t \partial_\phi \varphi - \omega^2 \partial_\phi^2 \varphi + \nabla^2 \varphi = \\ 4\pi (1+\varphi)^3 (\rho(1+\varepsilon) - 3p) \end{aligned} \tag{5.23}$$

(alternatively we could transform the metric and then evaluate (5.3)).

We then use spherical harmonics to split this 3+1 differential equation into a set of 1+1 radial equations, one for each l and m term:

$$\begin{aligned} -\partial_t{}^2 \varphi_{lm} + im\dot{\omega} \varphi_{lm} + 2im\omega \partial_t \varphi_{lm} + m^2 \omega^2 \varphi_{lm} + \\ \frac{\partial_r [r^2 \partial_r \varphi_{lm}]}{r^2} - \frac{l(l+1)\varphi_{lm}}{r^2} = 4\pi S_{lm}(t,r) \end{aligned} \tag{5.24}$$

where we have also split the source term:

$$S_{lm}(t,r) = \int d\Omega Y^*_{lm}(\theta,\phi)[(1+\varphi)^3(\rho(1+\varepsilon)-3p)] \tag{5.25}$$

(we also wrote our own spherical harmonic package in order to do decomposition as in (5.25) and synthesis). We will use (5.24) to simulate binaries that retain some degree of eccentricity.

For binaries that are in quasi-circular orbits, we further make the Weak Radiation Reaction (WRR) approximation: there are two timescales present, the fast orbital motion characterized by ω (with period $T \sim \omega^{-1}$), and the longer radiation reaction timescale τ. For a binary with separation d the ratio of these timescales goes as $\tau/T \sim (d/M)^{5/2}$. Thus there is a hierarchy of scales among the time derivatives:

$$\frac{\partial}{\partial t^2} \sim \frac{1}{\tau^2}, \qquad \omega\frac{\partial}{\partial t} \sim \dot{\omega} \sim \frac{1}{T\tau}, \qquad \omega^2\frac{\partial}{\partial \phi^2} \sim \frac{1}{T^2} \tag{5.26}$$

The second time derivative term is the smallest, and is dropped in our code, giving a first order in time differential equation (which resembles the 1-D Schrödinger equation):

$$\begin{aligned}\partial_t\varphi_{lm} = \frac{i}{2m\omega}[&\frac{\partial_r[r^2\partial_r\varphi_{lm}]}{r^2} + (m^2\omega^2 + im\dot{\omega} \\ &-\frac{l(l+1)}{r^2})\varphi_{lm} - 4\pi S_{lm}(t,r)]\end{aligned} \tag{5.27}$$

for the $m \neq 0$ terms and

$$\frac{\partial_r[r^2\partial_r\varphi_{l0}]}{r^2} - \frac{l(l+1)}{r^2}\varphi_{l0} - 4\pi S_{l0}(t,r) = 0 \tag{5.28}$$

for the time independent $m = 0$ terms.

To solve for the initial data for the Cauchy evolution we drop the single time derivative terms in equation (5.27) giving:

$$\frac{\partial_r[r^2\partial_r\varphi_{lm}]}{r^2} + \left(m^2\omega^2 - \frac{l(l+1)}{r^2}\right)\varphi_{lm} \\ -4\pi S_{lm}(t,r) = 0 \tag{5.29}$$

We also need boundary conditions. At the inner boundary we set the radial derivative of the φ_{lm} terms to zero:

$$\partial_r\varphi_{lm} = 0 \tag{5.30}$$

and at the outer boundary we use the Sommerfeld outgoing wave boundary condition, which has been transformed into the co-rotating reference frame:

$$\partial_t\varphi_{lm} = im\omega\varphi_{lm} - (1/r)\varphi_{lm} - \partial_r\varphi_{lm} \tag{5.31}$$

When building our code we first modeled binaries in quasi-circular orbit, and thus used equation (5.27) to evolve the field φ. As noted this equation closely resembles the Schrödinger equation, and we therefore finite differenced it using the fast, stable and accurate Crank-Nicholson method (see e.g. [146]).

After this was successful we turned to finite differencing the hyperbolic equation (5.24). Given the success we had in evolving (5.27) with Crank-Nicholson, we devised a modified Crank-Nicholson for (5.24):

$$\begin{aligned}
-(\varphi_i^{N+1} - 2\varphi_i^N + \varphi_i^{N-1}) + im\omega\Delta t(\varphi_i^{N+1} - \varphi_i^{N-1}) = \\
\frac{\Delta t^2}{2}(-\frac{(\varphi_{i+1}^{N+1} - 2\varphi_i^{N+1} + \varphi_{i-1}^{N+1})}{\Delta r^2} - \frac{(\varphi_{i+1}^{N+1} - \varphi_{i-1}^{N+1})}{r\Delta r} \\
+(\frac{l(l+1)}{r^2} - m^2\omega^2 - im\dot{\omega})\varphi_i^{N+1}) \\
+\frac{\Delta t^2}{2}(-\frac{(\varphi_{i+1}^{N-1} - 2\varphi_i^{N-1} + \varphi_{i-1}^{N-1})}{\Delta r^2} - \frac{(\varphi_{i+1}^{N-1} - \varphi_{i-1}^{N-1})}{r\Delta r} \\
+(\frac{l(l+1)}{r^2} - m^2\omega^2 - im\dot{\omega})\varphi_i^{N-1}) \\
+2\pi\Delta t^2(S_i^{N+1} + S_i^{N-1})
\end{aligned} \tag{5.32}$$

We find that this balanced implicit method also allows for fast, stable, and accurate field evolutions.

5.3.2 Newtonian Binary

Our numerical code was developed in three primary steps in order to ensure that it correctly models the dynamics of a Nordtröm binary. In this subsection we model a simple Newtonian system, and then model a linear scalar wave equation system in the next. We then finish with the results for Nordström's fully relativistic theory.

The Newtonian system is given by:

$$\nabla^2\varphi = 4\pi\rho \tag{5.33}$$

$$d^2x_a^i/dt^2 = m_a^{-1}\int_a \rho\partial_i\varphi d^3x \tag{5.34}$$

Equation (5.33) can be split into its spherical harmonic components by dropping the $m^2\omega^2\varphi_{lm}$ term from equation (5.29):

$$\frac{\partial_r[r^2\partial_r\varphi_{lm}]}{r^2} - \frac{l(l+1)}{r^2}\varphi_{lm} + 4\pi S_{lm}(t,r) = 0 \tag{5.35}$$

and generating the source terms via $S_{lm}(t,r) = \int d\Omega Y^*_{lm}(\theta,\phi)\rho(t,r,\theta,\phi)$. Equation (5.35) is then finite differenced in the standard second order manner. We need to check that the numerical solution for φ converges to the correct answer. One can concoct a matter distribution for the stars such as $\rho(r) = \rho_0(1 - r^2/R^2)$ (with central density ρ_0 and radius R) which allows for an exact analytical solution for φ. Upon resynthesizing the field from its harmonic components, we find that our numerical solution converges at second order to the analytical solution. Figure 1 shows an equatorial slice of φ in a given setup, while figure 2 demonstrates second order convergence to the analytical solution.

The Newtonian system presents a second test in addition to the convergence of the field: the integral in equation (5.34) must also converge to the expected inverse square law (when x^i is the separation vector). Note also that we are already using a "hydro-without-hydro" type of approximation: the matter is described by a rigid density profile, so that only the acceleration of the center of mass needs to be determined via (5.34). We find that solving for this acceleration is somewhat involved in a spherical coordinate system. When the derivatives $\partial_i\varphi$ in (5.34) are approximated with the standard second order finite differencing method: $\partial_i\varphi \sim (\varphi(i+1) - \varphi(i-1))/2\Delta x^i$ it turns out that an excessively large number of grid points are needed within the volume of the star for the total integral to accurately reproduce the expected inverse square law. Mesh resolutions that solve (5.33) correctly to within 1 percent can give accelerations based on (5.34) that are 100 percent off. Even if we by fiat insert the analytical values for φ into the grid points and then proceed with the finite differencing we find a similar low performance. Note that this method does converge at second order to the correct solution; it just starts off very poorly, so that an unreasonably high resolution is needed for this second order convergence to reduce the error to an acceptable value. A plot of the error in the radial acceleration as a function of separation for a particular setup is shown in Figure 3.

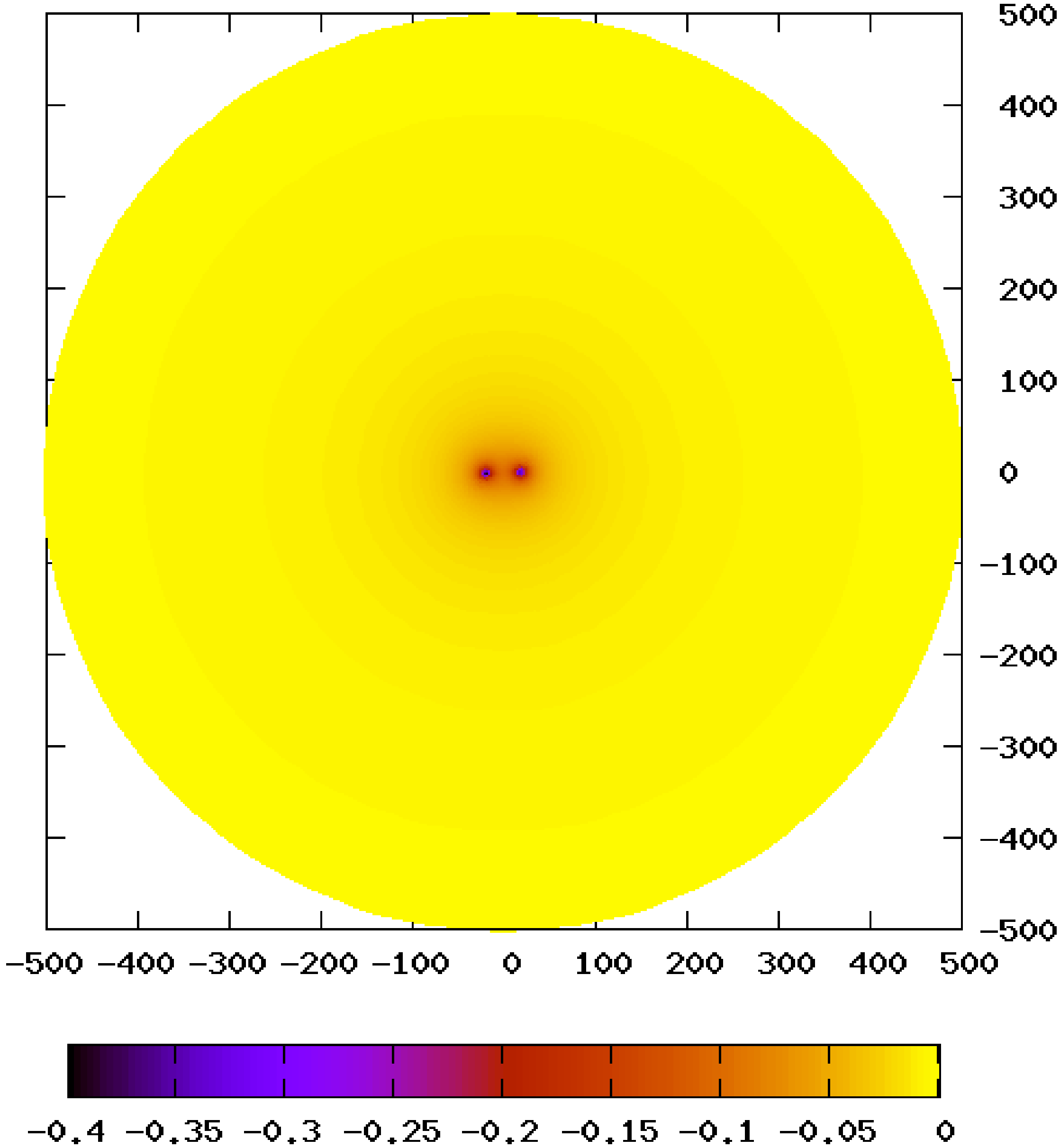

Figure 5.1: Equatorial slice of the field strength φ. The stars have radius $5M$, are situated $\pm 20M$ from the origin, and the outer boundary is $500M$ from the origin.

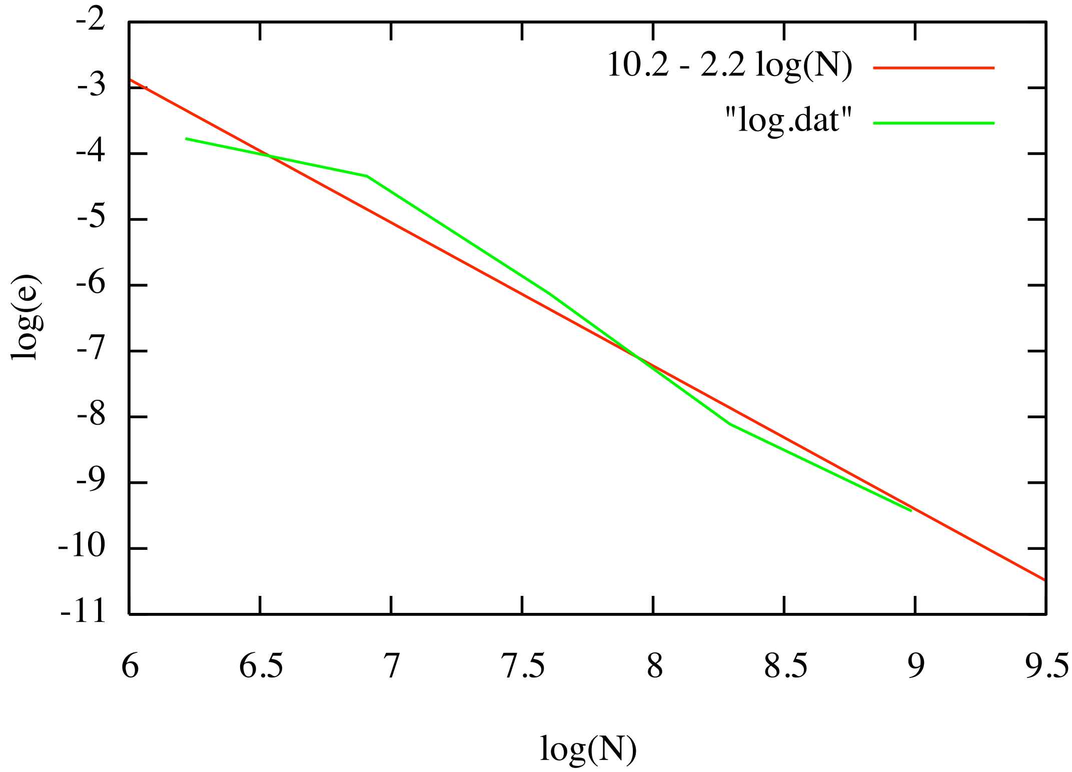

Figure 5.2: Plotted is the log of the error $e = \sup|\varphi_{Newton}/\varphi - 1|$ against the log of the number of radial grid points N. A linear fit gives a slope of -2.2 ± 0.2, i.e. second order convergence. The lowest resolution grid uses $N = 500$ radial grid-points and L and M values up to 25. This is then doubled four times up to resolution with $N = 8000$ radial grid points and L and M values up to 400.

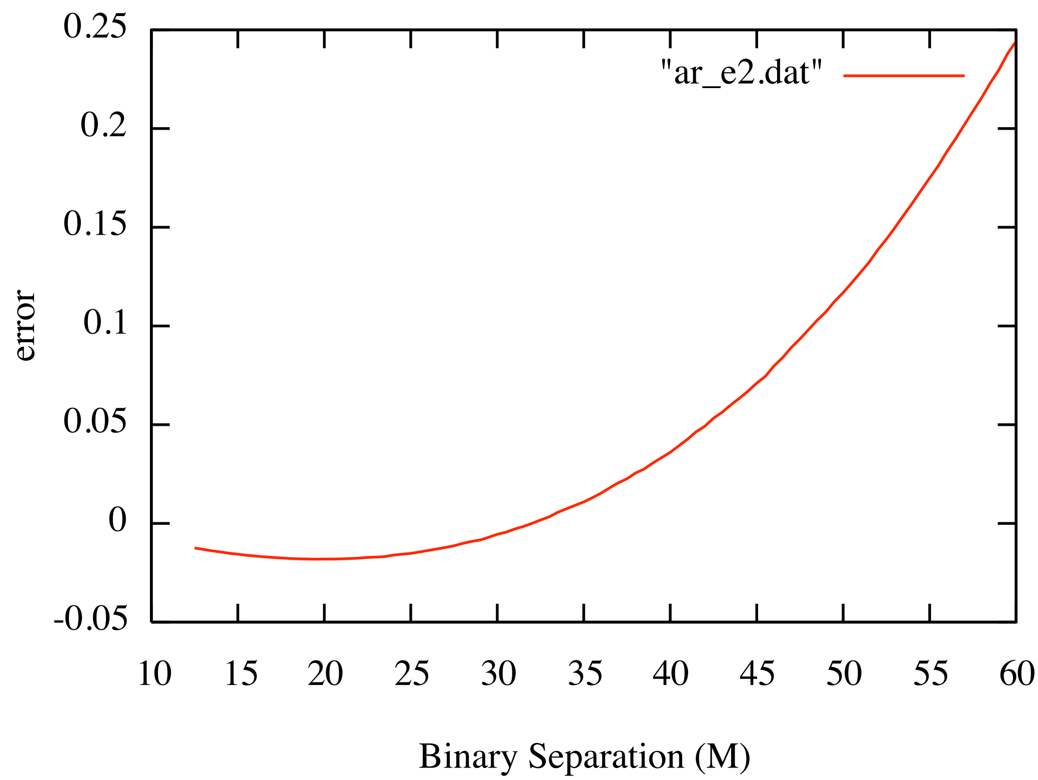

Figure 5.3: Plotted is the error $= (a_r)/(1/d^2) - 1$ of the radial acceleration (compared to the expected Newtonian inverse square law) as a function of the separation d. Standard second order accurate finite differencing methods are used to find the derivatives of the field en route to calculating a_r. The error grows to 25 percent for a separation of $60M$, despite the field being correctly resolved to within 0.3 percent at this distance.

The low performance can be understood by examining φ in the region of star a. φ is the sum of two components: $\varphi = \varphi_a + \varphi_b$ where φ_a is the self-field of star a: $\varphi_a \sim -M_a/R$ and φ_b is the field due to star b at a distance d away: $\varphi_b \sim -M_b/d$. Analytically the contribution of φ_a to the integral in (25) is zero: $\int_a \rho \partial_i \varphi_a d^3x = 0$, but numerically there will be some small residue C. The residue C is exacerbated by the fact that the spherical grid does not intersect the star evenly: the hemisphere closer to the origin has a denser distribution of grid points than the hemisphere which is further away. The problem is then that the self field φ_a is much larger than φ_b in the region of a and thus the residue C can swamp the correct contribution from $\int_a \rho \partial_i \varphi_b d^3x$. As expected, this swamping effect becomes worse at larger separations, since the φ_b contribution decreases as the inverse square of the distance, and the mesh resolution inside the star decreases.

We noted that poor accuracy is the result even if we insert the analytical solution into the mesh points and proceeded with the calculation. However, we can also find the exact analytical solutions for the derivatives of the field $\partial_i \varphi$ at the mesh locations. It turns out that if we insert these and do the sum, a much more accurate result is obtained. The second order finite differencing in the curvilinear coordinate system is thus the source for the slow initial convergence. We found that using higher order methods resulted in much greater accuracy. In fact, each higher order resulted in a more accurate result, so we ended up settling on a 12th order method. The 12th order derivative is found by fitting the grid point in question, and 6 more adjacent grid points on either side, to a 12th order polynomial via the Lagrange Interpolation Formula (see [147]). The derivative of this polynomial is taken, and then evaluated

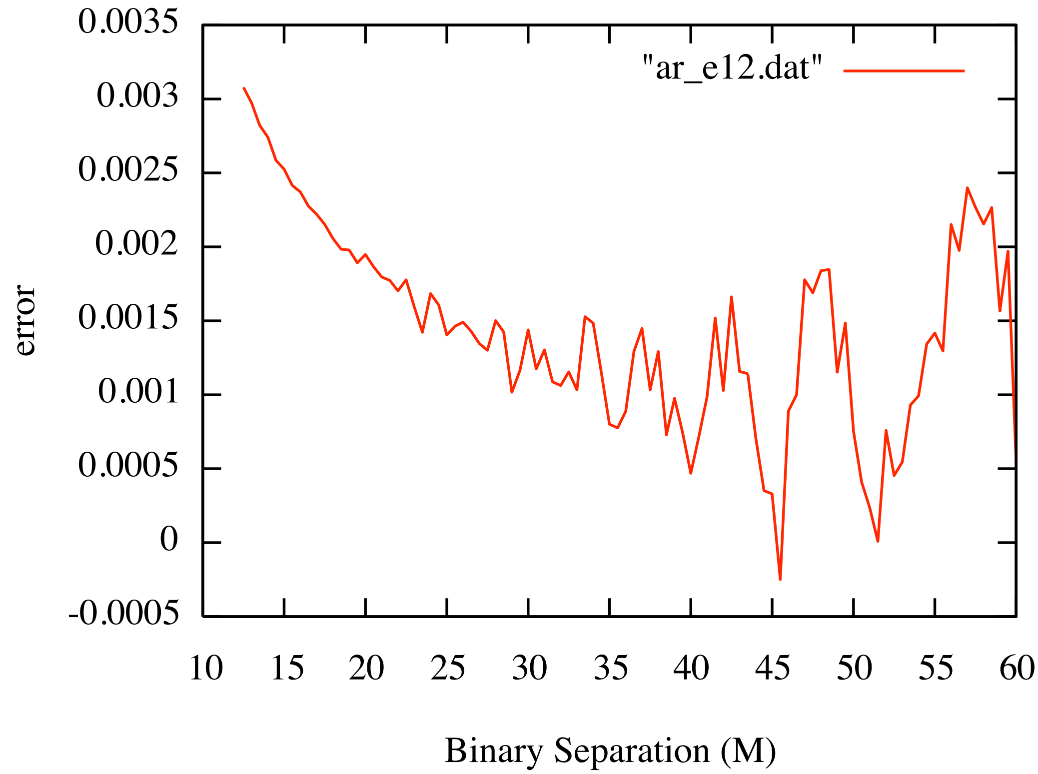

Figure 5.4: Another plot of the error $= (a_r)/(1/d^2) - 1$ of the radial acceleration, but now using 12th order finite differencing to extract the derivatives. The result is now accurate to with 0.3 percent, which is the same accuracy the field is resolved to.

at the central grid point giving:

$$\begin{aligned}\partial_i \varphi \simeq \frac{1}{27720\Delta x}[&5\varphi_{i-6} - 72\varphi_{i-5} + 495\varphi_{i-4}\\ &-2200\varphi_{i-3} + 7425\varphi_{i-2} - 23760\varphi_{i-1}\\ &+23760\varphi_{i+1} - 7425\varphi_{i+2} + 2200\varphi_{i+3}\\ &-495\varphi_{i+4} + 72\varphi_{i+5} - 5\varphi_{i+6}]\end{aligned} \tag{5.36}$$

As noted by Boyd [147] using high order polynomials can be dangerous as the polynomial fit can vary wildly from the function it approximates between sample points. However, we only utilize the 12th order polynomial in the very center, which is essentially always well fit. It is analogous to the case of finding a power series expansion for a function: the power series will only be valid in its radius of convergence, as determined by the poles of the function in the complex plane. Since we only utilize our interpolated polynomial at the central point, it will be accurate as long as it has some minimal radius of convergence ϵ. Indeed we find that these high order approximations give good performance throughout our code, as shown in Figure 4. We note that other groups have reported that they need a lot of resolution in the potential wells of the sources in order to resolve the fields sufficiently (many using Adaptive Mesh Refinement to enable this). They may find that using higher order methods lessens the resolution needed for accurate results.

5.3.3 Linear Scalar Wave Binary

The next step is to change the Laplacian operator in equation (5.33) into a wave operator:

$$\Box\varphi = 4\pi\rho \tag{5.37}$$

The spherical harmonic decomposition for this in corotating coordinates was given in (5.24) and the initial data is found by solving (5.29). The homogeneous version of (5.29) is solved by the Bessel and Neumann functions $j_l(m\omega r)$ and $\eta_l(m\omega r)$, or in the case of the Sommerfeld boundary condition (6.30), an outgoing wave spherical Hankel function. At large r this asymptotically approaches a sinusoidal function of frequency $m\omega$ with a $1/r$ envelope. Our solver correctly reproduces this behavior. In general the full solution to the inhomogeneous equation could also be found by utilizing Green's functions. In Figure 5 we show an example solution to (5.37), having divided through everywhere by the Newtonian solution in order to emphasize the waves.

This simple wave equation system provides further precise tests. We can continue to use the Newtonian equation (5.34) to calculate accelerations based on the field φ. As is the case for Norström's theory, the wave nature of $\Box\varphi$ gives rise to an acceleration

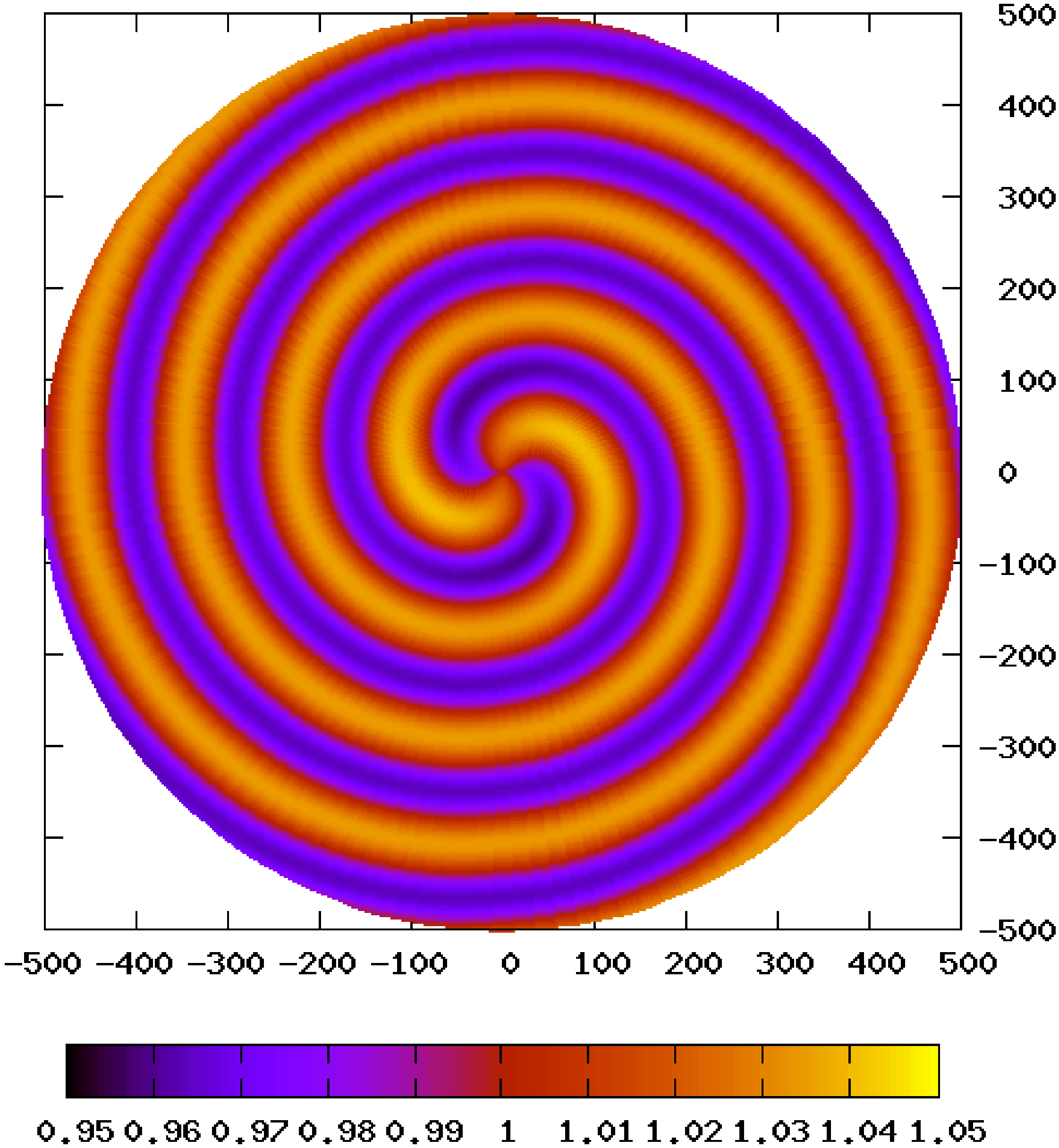

Figure 5.5: Plot of φ_{Newton}/φ for a separation of $14M$. The waves differ from the Newtonian field by about 5 percent.

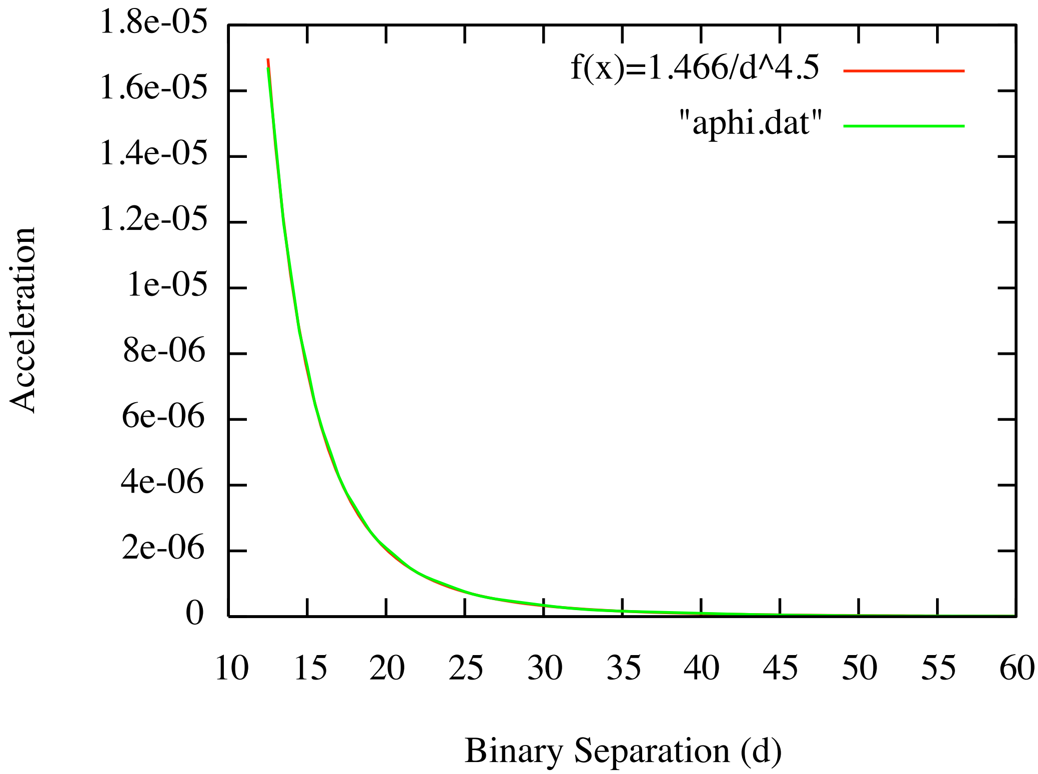

Figure 5.6: Plot of the acceleration in the ϕ direction as a function of separation. The fit value of 1.466 agrees with the theoretical value $2^{9/2}/15$ to within 3 percent.

opposite of the direction of motion for two stars. To phrase it in Newtonian language, this is the drag force that causes the orbit to decay and the stars to spiral into one another. The quadrupole calculation dictates that the stars decay at a rate: $\dot{d} = -(64/15)M^3/d^3$ where d is the separation and $M = M_a = M_b$ is the mass of the equal mass stars. Let the two stars be instantaneously aligned along the x-axis in a Cartesian plane, at $\pm d/2$ away from the origin, with Newtonian velocities $\pm\hat{y}\sqrt{M/4d}$. The acceleration opposite to the velocity needed to cause a quasi-circular orbit to decay at this rate is $\ddot{y} = (1/15)M^{7/2}/(d/2)^{9/2}$. The code correctly reproduces the inverse nine-halves scaling of the acceleration with respect to the separation, with the correct coefficient, as shown in Figure 6.

There is a final, interesting test to perform with the linear scalar wave system before implementing the full Nordström theory. In the Newtonian system we used

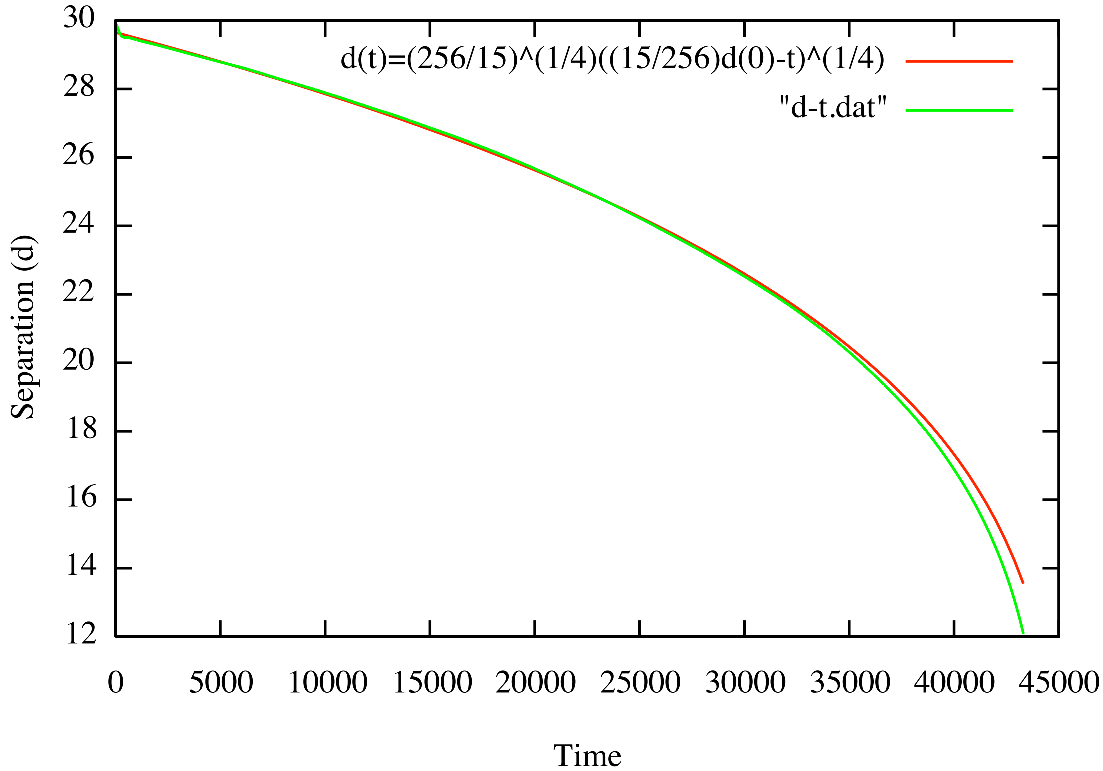

Figure 5.7: Separation as a function of time for a quasi-circular inspiral.

high order finite differencing to solve equation (5.34) and found $\ddot{x}_a = -M_b/d^2$ as expected. When we solve for the acceleration along the x-axis after migrating to the wave system we still recover an inverse square scaling, but the overall coefficient is a fraction of the mass M_b, no matter how large the separation is. It turns out that this is the correct result, since this system does exhibit the Nordtvedt effect. Again using Newtonian parlance, the Nordtvedt effect essentially adds a ”repulsive force” that also scales as $1/d^2$. The magnitude of the acceleration due to the Nordtvedt effect can be calculated using the post-Newtonian framework, giving: $\ddot{x} = -1/(3d^2)\int_a \rho\varphi d^3x$. The magnitude of the effect thus scales linearly with the compactness of the object M/R. The code accurately reproduces this effect on the acceleration.

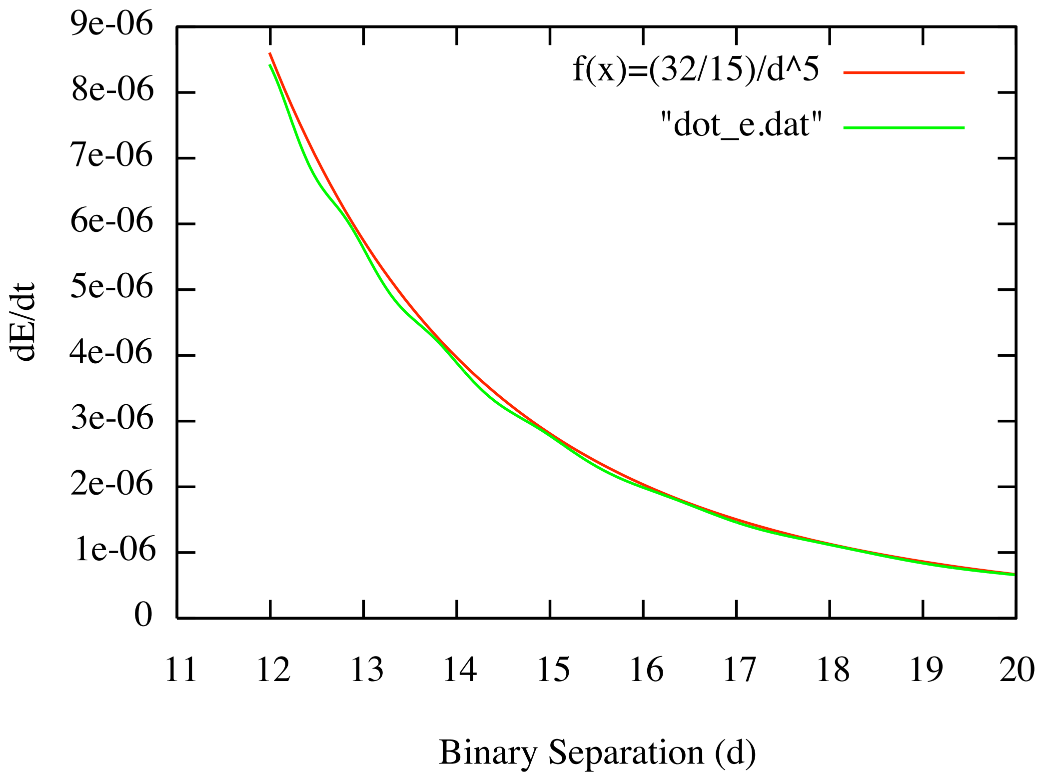

Figure 5.8: Plot of the rate of energy loss of the binary dE/dt as a function of the separation d, compared to the theoretical value.

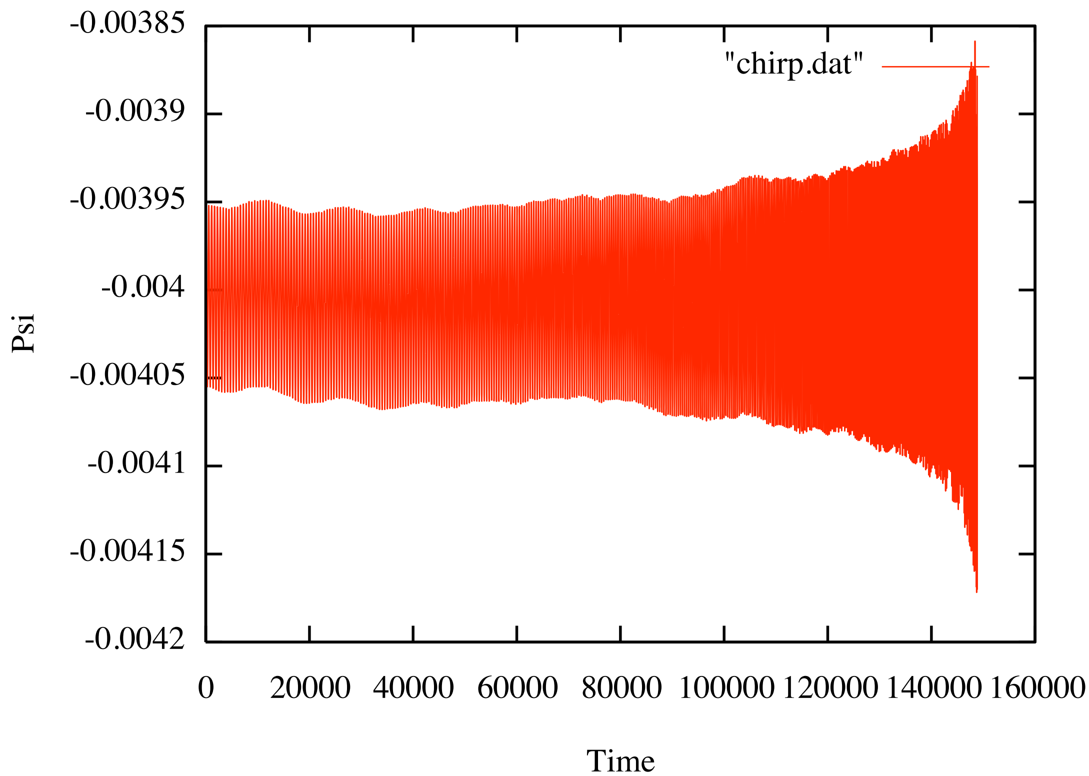

Figure 5.9: Plot field $\varphi(t, r = Rmax, \theta = \pi/2, \phi = 0)$ at the outer boundary as a function of time, showing the chirp waveform.

5.4 Modeling Nordström's Theory

With all of the intermediate tests passed we now solve for the full Nordström theory. Again we solve for the initial data with (5.29), but we do not decompose the source as we did in (5.25). Instead we rewrite the source term using the conserved density ρ^*, finding:

$$S_{lm}(t,r) = \int d\Omega Y^*_{lm}(\theta,\phi)[\sqrt{1-v^2}\rho^*(1+\varepsilon-3p/\rho)] \tag{5.38}$$

This removes much of the nonlinearity from the equation of motion for the field. Corrections to the internal energy and pressure now show up at 2PN order in the source, so it is not a bad approximation to plug in the initial isolated star profiles for these quantities. To test this we can also reevaluate ε and p using ρ^* (which we always keep equal to its single star solution), the iterative solutions for φ, equation (5.12), and the polytropic equations of state. When we solve for these new values and use them in (5.38) we find similar results: the net accelerations of the stars differ by a couple tenths of a percent.

First we model quasi-circular inspirals, and make use of the WRR approximation. After we find the initial data the field is evolved forward in time via (5.24), which is finite differenced with the Crank-Nicholson scheme. Note that it is crucial to also time average the source $S_{lm}(t,r)$ in the Crank-Nicholson scheme. Otherwise the source and field will be a half time step out of sync and large spurious accelerations will arise.

After each time step we synthesize the field $\varphi(r,\theta,\phi)$ from its spherical harmonic components. We use φ solve for the acceleration using discretized combination of (5.17) and (5.18). Equation (5.18) is expanded out in the corotating reference frame. The corotation coordinate transformation adds new terms the metric (which resemble the lapse and shift vectors in GR) which in turn adds new terms to the sum of connection coefficients $\Gamma^j_{\alpha\beta}v^\alpha v^\beta$ in (5.18). These new additions add essentially a centripetal force, so that when the correct ω is found given the stars will be nearly at rest in the co-rotating frame. Not quite however, as an acceleration opposite of the direction of motion due to radiation reaction will cause the stars to slowly spiral in towards one another.

An example quasi-circular evolution is given in Figure 7 which closely matches the 1/4 power law inspiral predicted by the semi-analytical calculation. To the degree that it differs the simulation gives a slightly faster inspiral. While we don't calculate the radiation reaction out to octupole, this seems reasonable since the angular velocity ω is a little higher than would exist in a Keplerian orbit, due to the 1PN corrections in (5.20). Other checks are available as well: shown in Figure 8 is a plot of the measured energy loss rate at the outer shell of the domain. This also matches the analytical prediction. In fact we can track the energy as a function of time throughout the computational domain using (5.6) and we find that it decreases in sync with the radiation loss. Finally a representative plot of the chirp waveform produced by this system is shown in Figure 9.

The quasi-circular case is a success, so we now examine binaries that retain a small amount of eccentricity. We drop the WRR approximation and evolve the field with the modified Crank-Nicholson scheme given in (6.34). An example inspiral is shown in figure (5.10). Note that the binary circularizes over time, as in GR. We describe this in more depth in our companion paper.

The main feature we examine here is the rate of precession of our binary. The 1PN accurate accelerations given in (5.19) and (5.21) cause a binary to precess at

$$\Delta\tilde{\omega} = -\frac{\pi M}{a(1-e^2)} \tag{5.39}$$

radians per radial orbit, which is six times slower and in the opposite direction as GR.

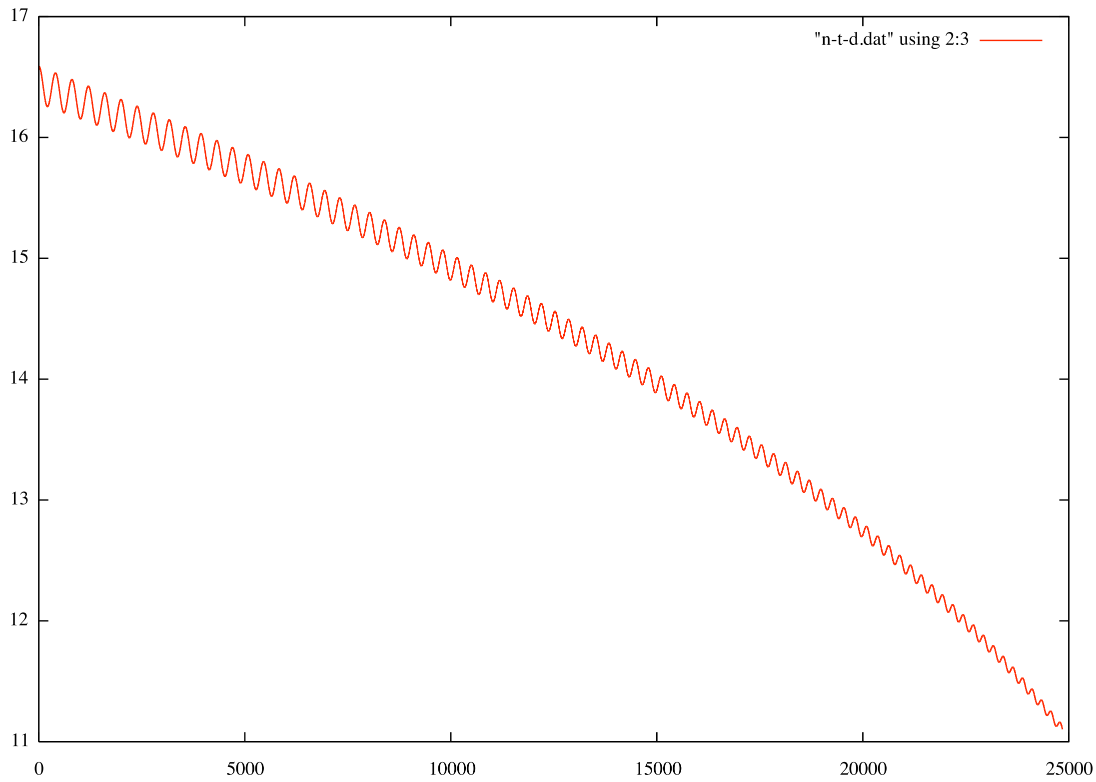

Figure 5.10: Eccentric inspiral: separation as a function of time.

While our simulation gives a rate of precession similar to (5.39) (it is also inversely proportional to the separation d), the overall coefficient is smaller: in the simulation the binary precesses more slowly. It was assumed at first that this was due to a numerical or coding error, but we now feel that this is actually physically realistic. As noted, the analytic rate of precession can be traced to the post-Newtonian corrections to the accelerations given in (5.19) and (5.21). The code reproduces (5.21) nicely, but differs from the expected radial acceleration (5.20). The Newtonian acceleration in (5.20) is magnified by the post-Newtonian correction $(1 + (M_b/2)/d)$, but our code instead gives a larger magnification $(1 + (M_b/2 + C)/d)$ with $C > 0$ (which leads to a slower rate of precession).

After checking for errors, we now believe that this is a real feature of the theory. It turns out that the discrepancy C is proportional to the compactness of the star: $C \propto M_a/R$, and thus we recover the expected rate of precession when the compactness M_a/R goes to zero. We also recover the expected precession (5.39) for highly compact stars if we use the 1PN approximation of the matter equations of motion (5.18). In fact, while we have not done a complete 2PN analysis of Nordström's theory, we can point towards suspicious 2PN terms in an expansion (5.18) that would explain the discrepancy we observe.

We thus appear to be observing a Nordtvedt-like effect occurring in Nordström's second theory, only in this case is occurring due to 2PN terms. In hindsight we should have perhaps expected this since all metric theories of gravitation other than general relativity are expected to fail the Strong Equivalence Principle (SEP) at some level (see e.g. [88]). If this is the correct analysis, then not only has our code closely matched the secular decay rates as found in our companion paper, but it has also correctly detected subtle behavior we were not initially expecting.

5.5 Conclusions

The numerical techniques we have developed work well in simulating binary inspirals in Nordström's theory. The code accurately matches the analytic predictions we made for Nordström's theory in the companion paper. It is also encouraging that the simulation picks up subtle behavior that we hadn't initially considered.

As a side benefit we find that Nordström's second theory is a useful laboratory for developing computational techniques for numerical relativity. It is a fully relativistic metric theory, and yet has fairly simple field equations which can be made nearly linear. Some of its nice attributes derive from the fact that it has no lowest order Nordtvedt effect, as it satisfies ($4\beta - \gamma - 3 = 0$) (see [88]): the stars move on Keplerian orbits to lowest order, and there are no star-crushing effects. There does appear to be higher order deviation from geodesic motion for highly compact bodies, but this is most likely the case for any theory other than GR, and it only slightly affects the orbital motion (we are considering attempting to prove that Nordström's theory violates the SEP at 2PN in a follow up paper).

Our main goal is to use our corotating spherical coordinates framework to model the late inspirals of binaries in GR. Given the success we have had in applying it to Nordström binaries, we feel confident that it should allow for fast and accurate simulations in GR as well, thus complementing the results of other groups. We are still considering the specifics of the implementation. The "Hydro-without-Hydro" and WRR approximations have served us well so far, and we may use them again in building a GR code. However, the moving puncture results are also impressive, so we are also tempted to try and integrate them with a corotating spherical grid. They would allow us to evolve the binary from late inspiral through the plunge, merger and ringdown.

Chapter 6

Details of the Numerical Implementation

6.1 Introduction

The previous chapter gives the basics of our computational simulation of an inspiraling binary, but there are many interesting and sometimes tricky details that need to be included here. We discuss them in the order they are evaluated in the simulation. We first construct isolated star density profiles which will be used later as sources, following the hydro-without-hydro approximation. We then pre-compute the spherical harmonics at the necessary angular grid locations, and use these to decompose the source found in the previous section. With the source expressed in its spherical harmonic components we then solve for the initial field data, and then proceed to evolve the fields forward in time, with one of two methods depending on whether the Weak Radiation Reaction approximation is being used or not. After each time step we re-synthesize the field and solve for the matter equations of motion, thus updating the stars positions and velocities. The code runs until the stars have nearly merged and then finishes by writing out the data. In the second to last section we describe modifications that are needed to adapt the code to a parallel architecture. We finish with an examination of the acceleration of massive bodies in Nordström's theory: we check that there is no Nordtvedt effect to 1PN, as expected, and then outline the calculation to 2PN where we do expect a violation of the SEP based on the evidence outlined in the numerical paper.

6.2 Isolated Star Solutions

In our code we make use of the Hydro-without-Hydro approximation. This allows us to avoid dealing with black hole horizons and singularities and complicated fluid motions, at least for the time being. In general relativity one could hypothetically construct a very compact star that was near to the Buchdahl-Bondi limit [148], [149] with a radius approaching $9/4M$. We find that we can also construct very compact

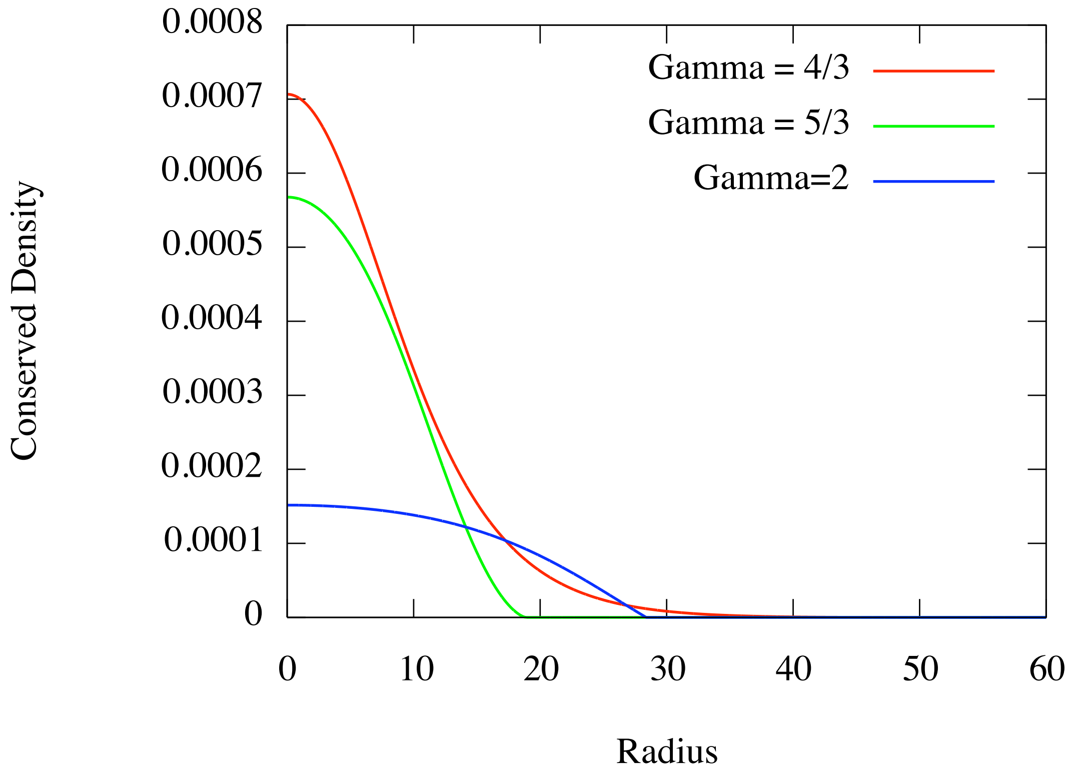

Figure 6.1: Plot of conserved density as a function of radius $\rho^*(r)$ for three stars with polytropic equations of state $\Gamma = 4/3$, $5/3$, and 2. All stars are constructed to give $M_{grav}/R = 1/5$.

stars in Nordström's theory as well. We note some of the empirical findings for very compact stars with different equations of state here.

The main equations are given in the numerical paper, which for clarity we repeat here. $R = 24\pi T$ reduces to:

$$\frac{1}{r^2}\partial_r(r^2\partial_r\varphi) = 4\pi(1+\varphi)^3(\rho(1+\varepsilon) - 3p) \tag{6.1}$$

We will assume the star is a polytrope, so that the pressure and internal energy become:

$$p = \kappa\rho^{\Gamma} \tag{6.2}$$

$$\varepsilon = \frac{\kappa}{\Gamma - 1}\rho^{\Gamma-1} \tag{6.3}$$

which reduces equation (6.1) to a function two variables. We use the projection operator $Q^{\alpha}_{\mu} = u^{\alpha}u_{\mu} + \delta^{\alpha}_{\mu}$ on the divergence of the stress energy tensor $T^{\mu\nu}{}_{;\mu} = 0$ to get the second equation:

$$\rho h u^{\nu} u^{\mu}{}_{;\nu} + Q^{\nu\mu} p_{,\nu} = 0 \tag{6.4}$$

where h is the enthalpy: $h = h(\rho) = 1 + \varepsilon + p/\rho$. With $u^0 = 1/(1+\varphi)$ and $u^i = 0$ we can reduce this to:

$$\frac{d\varphi}{dr} = -\frac{(1+\varphi)}{h}\frac{dh}{dr} \tag{6.5}$$

We will solve (6.1) and (6.5) by constructing an iterative version of the Lane-Emden equation (see [15]). In the first iteration the $(1+\varphi)^3$ term is dropped from (6.1) and the $(1+\varphi)$ term from (6.5), and we then pick a value for the central density ρ_c and integrate out until the density and pressure drop to zero. Then in successive iterations we plug in the previously computed values for these into (6.1) and (6.5) to solve for the next iteration. For low enough values of ρ_c the process will converge, giving us our stellar model.

We need to pick values for κ and Γ as well. Γ is the most important quantity since it determines the distribution of matter inside the star. The overall scaling is not as important since in the primary code we will re-scale the mass and radius so that each star has a mass of 0.5. Nevertheless, out of curiosity we also gave the stars quasi-realistic values for κ as well. Since we are building neutron-star like objects, we pick the fundamental unit of measurement to be kilometers, and set $c = G = 1$ so that the mass is also measured in kilometers. Following [15] we have for non-relativistic neutrons $\Gamma = 5/3$ and κ is given by:

$$\kappa = \frac{3^{2/3}\pi^{4/3}}{5}\frac{\hbar^2}{m_{neutron}^{8/3}} \tag{6.6}$$

while for extremely relativistic neutrons we have $\Gamma = 4/3$ and

$$\kappa = \frac{3^{1/3}\pi^{2/3}}{4}\frac{\hbar c}{m_{neutron}^{4/3}} \tag{6.7}$$

Additionally we construct a κ for the stiff equation of state $\Gamma = 2$, which is considered to be more realistic given current models of nuclear matter at neutron star densities.

Three example profiles of the conserved density ρ^* as a function of radius are given in figure (6.1). In each case we have picked central densities such that the final star is quite compact, with $M_{grav}/R = 1/5$. Note that here we are using the gravitational mass, which we showed in the post-Newtonian chapter to be:

$$M_{grav} = \int \rho^* \left(1 + \frac{1}{2}\bar{v}^2 - \frac{1}{2}\bar{U} + \Pi\right) d^3x \tag{6.8}$$

We can also compute the conserved rest mass of the star:

$$M_{rest} = \int \rho^* d^3x \tag{6.9}$$

which we can compare to M_{grav} as the central density increases. We see in (6.1) generally what we expect from solving Lane-Emden equations for different gravitational theories. The $\Gamma = 4/3$ star has a very long tail – it's hard to tell in the graph, but the tail doesn't completely peter out until a radius of about 53.6. The stiff $\Gamma = 2$ also behaves generally as we would expect, with the density more even throughout the star, and a sharp cutoff at the outer boundary. The $\Gamma = 5/3$ star is somewhere between these two extremes.

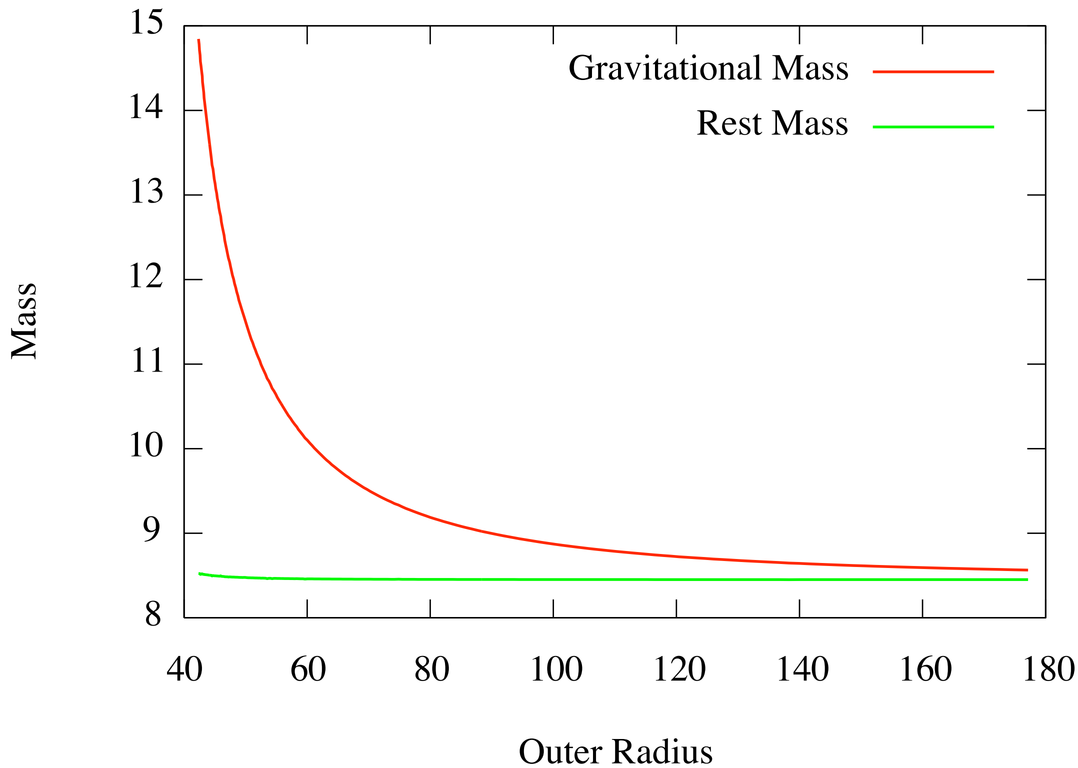

Figure 6.2: Total gravitational and rest masses as a function of the outer radius for a range of stars with polytropic equation of state $\Gamma = 4/3$.

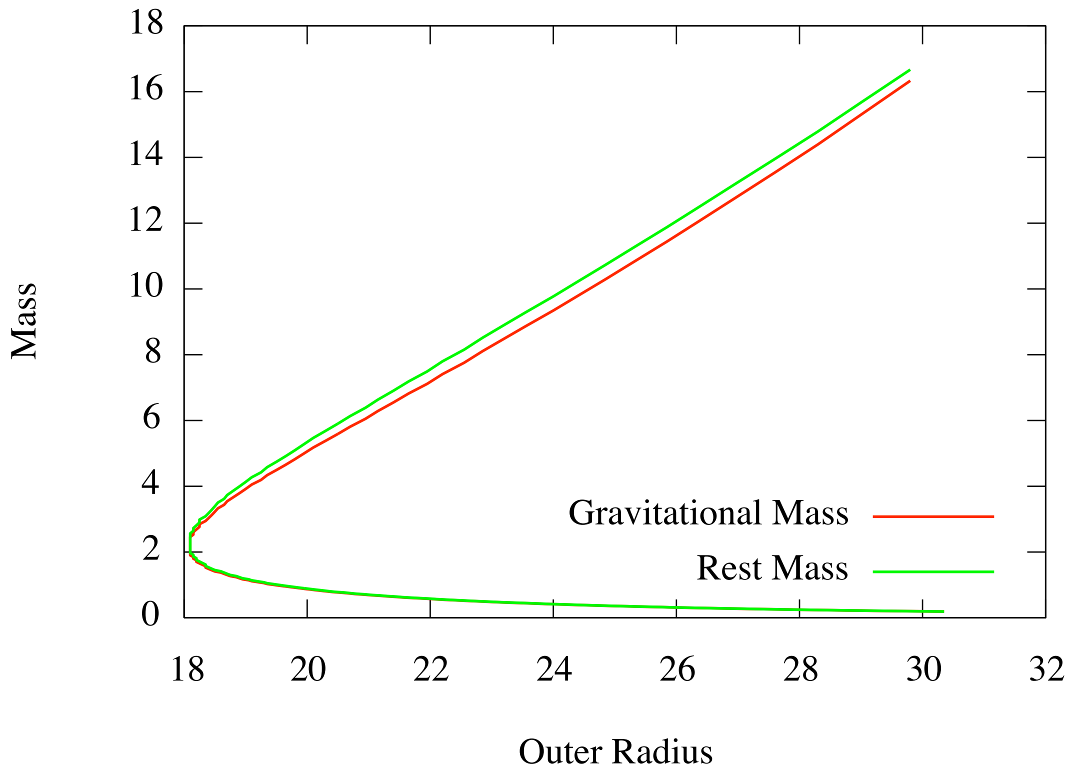

Figure 6.3: Total gravitational and rest masses as a function of the outer radius for a range of stars with polytropic equation of state $\Gamma = 5/3$.

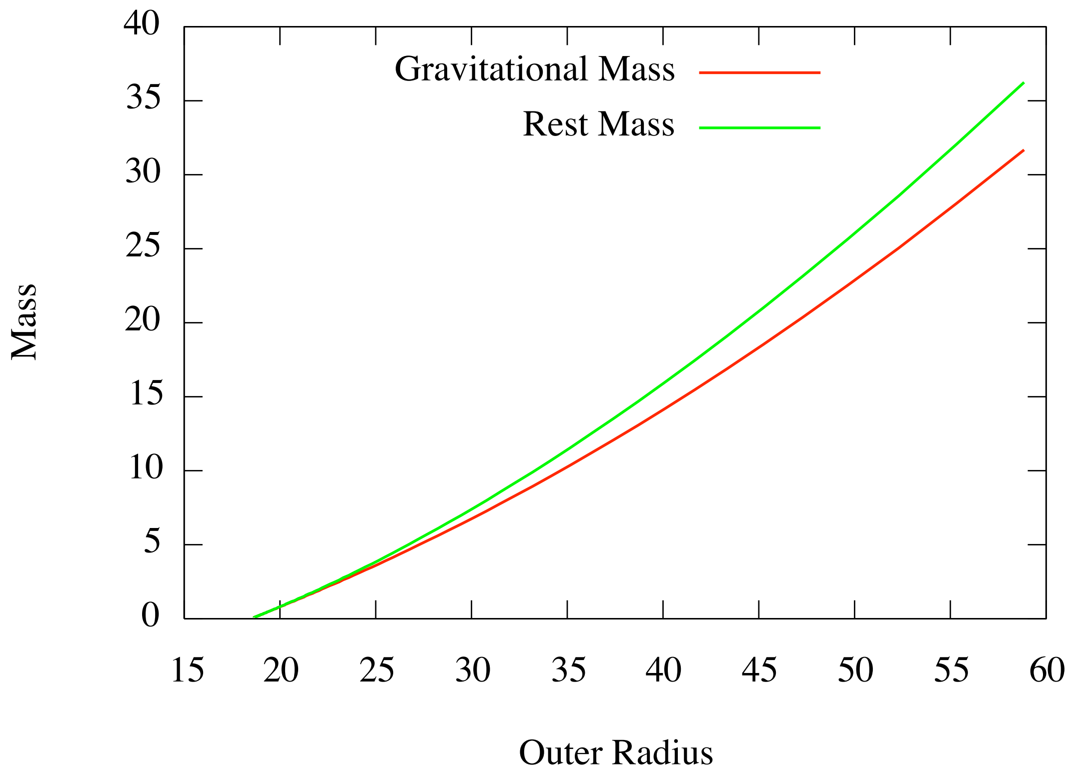

Figure 6.4: Total gravitational and rest masses as a function of the outer radius for a range of stars with polytropic equation of state $\Gamma = 2$.

As we will see in the next section on spherical harmonics, it is very helpful to use very smooth functions when doing spherical harmonic decomposition, as this process will converge exponentially quickly for a C^∞ function, and at n'th order for a C^n function. By this reasoning we should use the $\Gamma = 4/3$ function as our model star in our code since the outermost tail transitions very smoothly to zero. However we find that in practice at the mesh resolutions we are using for long term numerical evolutions that the $\Gamma = 5/3$ and $\Gamma = 2$ profiles converge more quickly. This is because many radial divisions are needed to sufficiently resolve the $\Gamma = 4/3$ case, which starts out with a very high density for a short interval near the origin, and then has a long skinny tail which doesn't contribute much mass but needs to be included. However, we find in testing that once enough zones are included to accurately resolve the $\Gamma = 4/3$ case that further refinements lead to a very quick convergence, so we may use this type of star in the future as computers get faster.

For each value of Γ we can also make a plot of the gravitational and conserved masses as a function of radius for a range of central densities, as we show in figures (6.2), (6.3), and (6.4). The $\Gamma = 4/3$ again shows behavior that we have seen elsewhere: the conserved rest mass M_{rest} is almost independent of the central density, with a value of about 8.6 kilometers, so that changing ρ_c only changes the radius of the star. The gravitational mass M_{grav} diverges however as the central density grows, indicating, as we would expect, that these stars are not stable. The $\Gamma = 5/3$ case is also interesting. For very low values of the central density the mass is about zero and the radius of the star diverges. As the central density increases, the mass increases and the star shrinks for a while, eventually hitting an inflection point with a radius of about 18 kilometers, and a mass of about 2.2 kilometers, which interestingly is in the ball park for neutron stars in general relativity. After that the star effectively grows stiffer, so that adding more mass increases the radius of the star until the central density grows too high and the iterative process no longer converges. It is also interesting that the gravitational and conserved masses are very similar all the way from very non-compact stars (where we would expect them to be), to very compact and highly self-gravity stars. The final case is $\Gamma = 2$ which is also interesting. Here in the limiting case that the mass and central density go to zero the star's radius converges to about 18.5 kilometers. Then, as this is a very stiff equation of state, as the mass grows so does the outer radius, while the process still converges. Also, as opposed to the $\Gamma = 4/3$ case, the gravitational mass now lags behind the conserved mass.

Finally in order to compare with the Buchdahl-Bondi limit we list the maximum values of compactness that we get in Nordström's theory for these equations of state. One can see that as the compactness increases and thus φ approaches -1 that equations (6.1) and (6.5) will break down. We find that for all of the equations of state that we get a somewhat similar maximum compactness: for $\Gamma = 2$ we get a minimum radius of about $R \simeq 1.94 M_{grav}$, for $\Gamma = 5/3$ we get a minimum radius of about $R \simeq 1.68 M_{grav}$, and for $\Gamma = 4/3$ we get a minimum radius of about $R \simeq 1.77 M_{grav}$. The depth of φ for these different polytropes is fairly different: the $\Gamma = 4/3$ star reaches its maximum compactness at about $\varphi \simeq -.978$, the $\Gamma = 5/3$ star becomes unstable at $\varphi \simeq -.725$, and the $\Gamma = 2$ star becomes unstable at $\varphi \simeq -.684$. While smaller than the Buchdahl-Bondi limit in general relativity and indeed smaller than the Schwarzschild radius, these radii are not too different from those in general relativity – other alternative theories of gravity can give substantially different minimum radii, or even none at all (see e.g. [88]).

6.3 Spherical Harmonic Analysis

A key component of our numerical methods is the implementation of spherical harmonics. There are numerical libraries available that can allow for a program to make use of spherical harmonics, but we prefer writing our own implementation so that it can be optimized and parallelized according to the needs of our code.

The first step is to generate them efficiently and store them in memory. Spherical harmonics are defined by:

$$Y_{lm}(\theta, \phi) = \sqrt{\frac{2l+1}{4\pi}\frac{(l-m)!}{(l+m)!}} P_l^m(\cos\theta) e^{im\phi} \tag{6.10}$$

We will pre-evaluate (6.10) at pre-chosen discrete values of theta and phi: $\theta \to \theta_i$ and $\phi \to \phi_j$ for l and m values up to some maximum value: $0 \leq l \leq L_{max}$, $-l \leq m \leq l$ (we will drop the i and j subindices henceforth: all equations are understood to be transformed into a discrete form for numerical implementation). We first split (6.10) into two functions:

$$Y_1(l, m, \theta) = \sqrt{\frac{2l+1}{4\pi}\frac{(l-m)!}{(l+m)!}} P_l^m(\cos\theta) \tag{6.11}$$

$$Y_2(m, \phi) = e^{im\phi} \tag{6.12}$$

with $Y_{lm}(\theta, \phi) = Y_1(l, m, \theta) \times Y_2(m, \phi)$ and thus we only need order $\mathcal{O}(N^3) + \mathcal{O}(N^2)$ bits to store the harmonics instead of $\mathcal{O}(N^4)$.

The next step is to evaluate the associated Legendre polynomials in (6.11). Given their definition the following recursion relation can be derived (see e.g. [150]):

$$(l-m)P_l^m(x) = x(2l-1)P_{l-1}^m(x) - (l+m-1)P_{l-2}^m \tag{6.13}$$

with the initial two terms given by

$$P_{l=m+1}^m(x) = x(2l-1)P_m^m(x) \tag{6.14}$$

and

$$P_m^m(x) = (-1)^m(2m-1)!!(1-x^2)^{m/2} \tag{6.15}$$

We can then multiply by the square root coefficient in (6.11) to generate the spherical harmonics. However, this method is not ideal, as it necessitates taking fractions of large factorials. By the time we have reached $L_{max} \sim 85$ this process breaks completely down since $171! \sim 10^{309}$ is the limit of double precision numbers. We can rewrite the recursion relations in terms of the $Y_1(l, m, \theta)$ functions which sidesteps this difficulty. We start by combining (6.11) and (6.15):

$$Y_1(m, m, \theta) = \sqrt{\frac{1}{4\pi} \frac{(2m+1)!!}{2^m m!}} (-1)^m (\sin\theta)^m \tag{6.16}$$

where the factorial section can be computed without doing dividing large numbers:

$$\sqrt{\frac{(2m+1)!!}{2^m m!}} = \left(\prod_{i=1}^{m} \frac{2i+1}{2i} \right)^{1/2} \tag{6.17}$$

We can then rewrite the recursion relation as:

$$\begin{aligned} Y_1(l, m, \theta) = \cos\theta Y_1(l-1, m, \theta) \sqrt{\frac{(2l+1)(2l-1)}{(l+m)(l-m)}} \\ -Y_1(l-2, m, \theta) \sqrt{\frac{(2l+1)(l+m-1)(l-m-1)}{(2l-3)(l-m)(l+m)}} \end{aligned} \tag{6.18}$$

with the special case of:

$$Y_1(m+1, m, \theta) = \cos\theta Y_1(m, m, \theta) \sqrt{2m+3} \tag{6.19}$$

Now that the spherical harmonics have been computed at the desired grid points, we need to use them to first decompose the source and later synthesize the field. The general equations are:

$$A_{lm} = \int d\Omega Y^*_{lm}(\theta, \phi) g(\theta, \phi) \tag{6.20}$$

and

$$g(\theta,\phi) = \sum_{l=0}^{\infty}\sum_{m=-l}^{l} A_{lm}Y_{lm}(\theta,\phi) \tag{6.21}$$

Both of these operations are order $\mathcal{O}(N^4)$, and each then need to be done for a span of radial grid points, so that the operations are overall $\mathcal{O}(N^5)$ for each time step. This is a steep price but we can reduce it defining temporary functions and by breaking up the operations into two steps:

$$\begin{aligned} B(\theta,m) &= \int d\phi g(\theta,\phi)Y_2^*(m,\phi) \\ A_{lm} &= \int \sin\theta d\theta B(\theta,m)Y_1(l,m,\theta) \end{aligned} \tag{6.22}$$

and

$$\begin{aligned} h(m,\theta) &= \sum_{l=0}^{L_{max}} A_{lm}Y_1(l,m,\theta) \\ g(\theta,\phi) &= \sum_{m=-L_{max}}^{L_{max}} h(m,\theta)Y_2(m,\phi) \end{aligned} \tag{6.23}$$

This reduces the calculation to order $\mathcal{O}(N^4)$ per volume per time step, which is further reduced by the fact that we only need to decompose and synthesize in the small volumes containing the compact bodies, as opposed to the entire coordinate grid.

Additionally, spherical harmonics are capable of converging very quickly, so that using very high order harmonics is unnecessary for accurate results. For a C^∞ function, spherical harmonics will converge exponentially quickly, and C^N functions will converge at order N. Unfortunately the polytropes that we chose in the previous section with $\Gamma = 2$ or $\Gamma = 5/3$ have low order C^N behavior at their outer boundaries. Nevertheless we find that they converge at reasonable rates. For example, we show a surface plot of a typical stellar profile with a typical mesh spacing in figure(6.5).

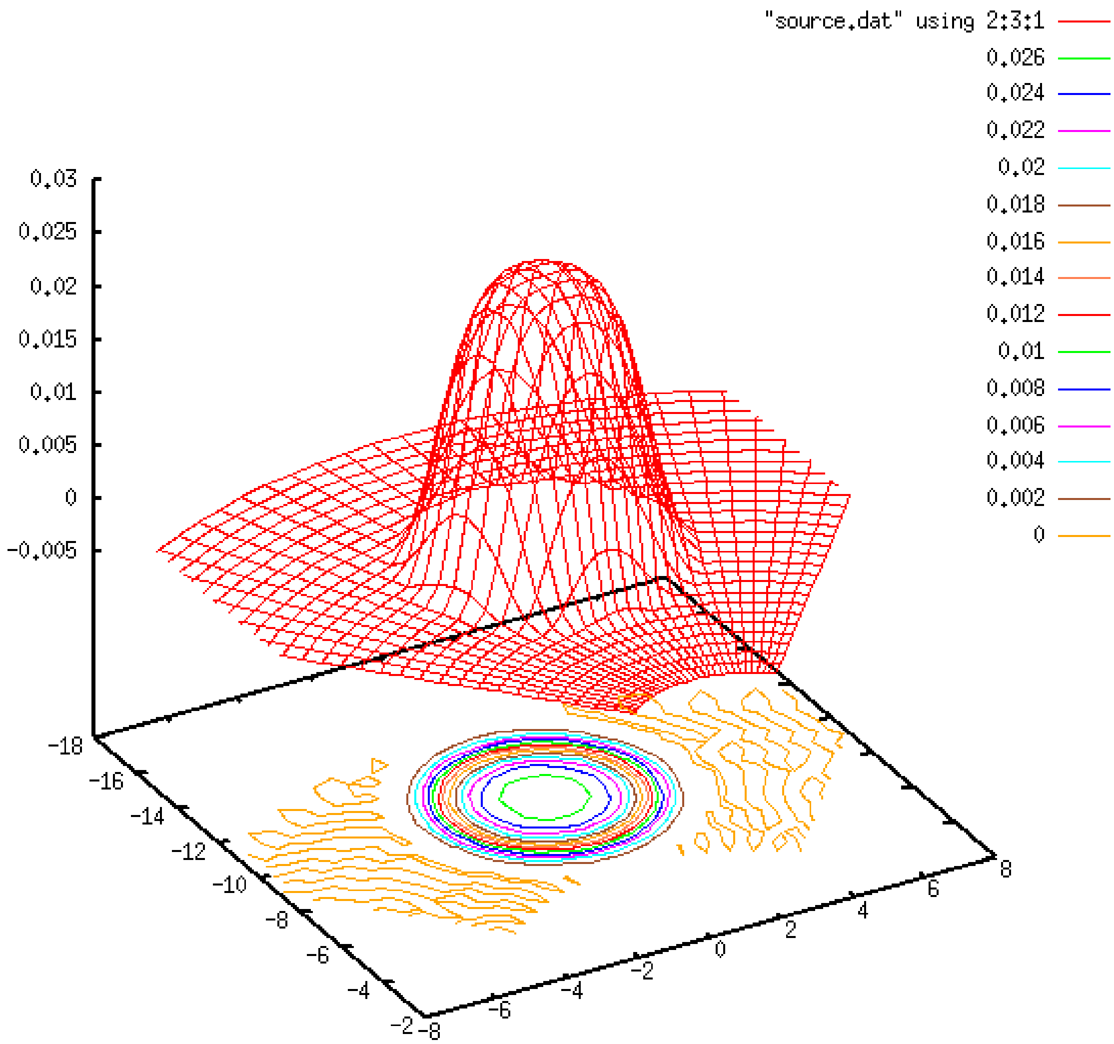

Figure 6.5: Equatorial slice of the source density

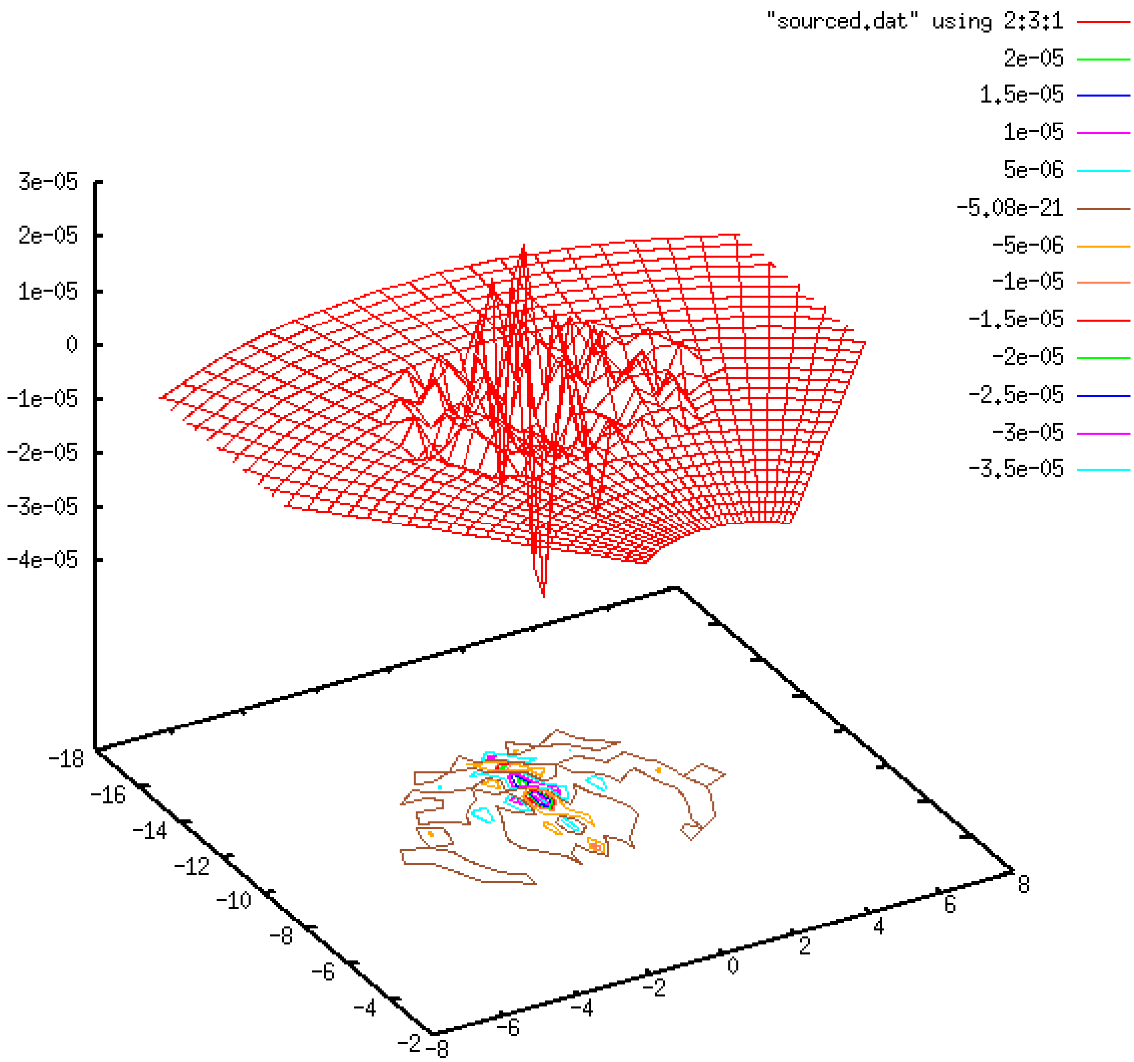

Figure 6.6: Source errors after convolution

We then decompose and re-synthesize this source and compare against the original profile, and find the errors are about one part in a thousand: (6.6).

It is thus possible to run high resolution meshes in a reasonable amount of time: a mesh with 10^3 radial grid points and spherical harmonics up to $L_{max} = 64$ takes about one second per time step on a modern single processor, and significantly less on a parallel architecture.

We get nice performance from the use of spherical harmonics in our program, but the implementation may need to be changed in the future. The primary problem is that the decomposition and synthesis operations are order $\mathcal{O}(N^4)$ as noted previously, and thus if they are needed over the entire volume of the simulation, as may be the case in the future, then the code will slowed considerably. However, alternative implementations based on adapting fast Fourier transform techniques to spherical harmonics are possible, see for example: [151], [152], [153]. These implementations converge more rapidly than our version, but they also have high overheads, and only become efficient when the harmonics L_{max} grow into the hundreds. There is thus room for improvement using these methods.

6.4 Implicit Finite Differencing

Now that we can find the source density as described in the first section of this chapter, and decompose it into its spherical harmonic components as described in the second section, we need to solve for the initial value of the scalar field φ and then evolve it forward in time. We rewrite the main 1+1 equations first given in the numerical paper. For the initial field we solve:

$$\frac{\partial_r[r^2\partial_r\varphi_{lm}]}{r^2} + \left(m^2\omega^2 - \frac{l(l+1)}{r^2}\right)\varphi_{lm} - 4\pi S_{lm}(t,r) = 0 \tag{6.24}$$

To evolve the field forward in time we then solve:

$$-\partial_t{}^2\varphi_{lm} + im\dot{\omega}\varphi_{lm} + 2im\omega\partial_t\varphi_{lm} + m^2\omega^2\varphi_{lm} + \frac{\partial_r[r^2\partial_r\varphi_{lm}]}{r^2} - \frac{l(l+1)\varphi_{lm}}{r^2} = 4\pi S_{lm}(t,r) \tag{6.25}$$

Additionally, if we make the Weak Radiation Reaction (WRR) approximation, then we drop the second time derivative from (6.25), giving:

$$\partial_t\varphi_{lm} = \frac{i}{2m\omega}\left[\frac{\partial_r[r^2\partial_r\varphi_{lm}]}{r^2} + (m^2\omega^2 + im\dot{\omega} - \frac{l(l+1)}{r^2})\varphi_{lm} - 4\pi S_{lm}(t,r)\right] \tag{6.26}$$

with the special case of:

$$\frac{\partial_r[r^2\partial_r\varphi_{l0}]}{r^2} - \frac{l(l+1)}{r^2}\varphi_{l0} - 4\pi S_{l0}(t,r) = 0 \tag{6.27}$$

for the time independent $m = 0$ terms.

In all of these equations we have already decomposed the source into its spherical harmonic components:

$$S_{lm}(t,r) = \int d\Omega Y^*_{lm}(\theta,\phi)[\sqrt{1-v^2}\rho^*(1+\varepsilon-3p/\rho)] \tag{6.28}$$

Note that we have rewritten the source by making use of the conserved density ρ^*. This removes much of the nonlinearity from the equations, which will be useful later when we adapt the code to a parallel architecture.

The boundary conditions are

$$\partial_r\varphi_{lm} = 0 \tag{6.29}$$

at the inner boundary, and

$$\partial_t\varphi_{lm} = im\omega\varphi_{lm} - (1/r)\varphi_{lm} - \partial_r\varphi_{lm} \tag{6.30}$$

which is the outgoing wave Sommerfeld boundary condition, expressed in the corotating reference frame.

We first solve (6.24). We take the finite differenced form of this equation, we produce a linear algebra problem of the form:

$$A_i^j \varphi_j = 4\pi S_i \tag{6.31}$$

where the tri-diagonal matrix A_i^j stems from the finite differenced derivatives and other multiplicative terms in (6.24). To solve for φ_j at the grid points j we thus need to do Gauss-Jordan elimination, which is an order $\mathcal{O}(N)$ operation for tri-diagonal matrices (see [146]).

In order to check the accuracy and convergence of this method we construct an analytical source ρ_{an} distribution which allows for an analytical solution for the field φ_{an} in the special case that $\omega = 0$ (i.e. it reduces to Newtonian gravity). Comparison with analytic solutions will also turn out to be very valuable later when we take volume integrals of field derivatives. As we showed in the paper, we find second order convergence to the analytic field with our second order accurate methods. We show a few more graphs here to flesh this out. In figure (6.7) we resynthesize φ from its spherical harmonic components to show a surface plot of the field strength on an equatorial slice of the domain. Figure (6.8) uses a color scale to show the same field from a top down view, and (6.9) shows the same from a side view. We then divide the numerical solution for the field φ through by the exact analytical solution φ_{an} in figure (6.10) to see the degree to which they agree – the plot shows that there is about 0.2 percent error near the compact bodies and about 0.4 percent error at the outer boundary. If we double the mesh resolution (both radially and in angular resolution, thus requiring 8 times the memory) we see that in figure (6.11) that the numerical error in the center is now at about 0.05 percent, agreeing with our claim of

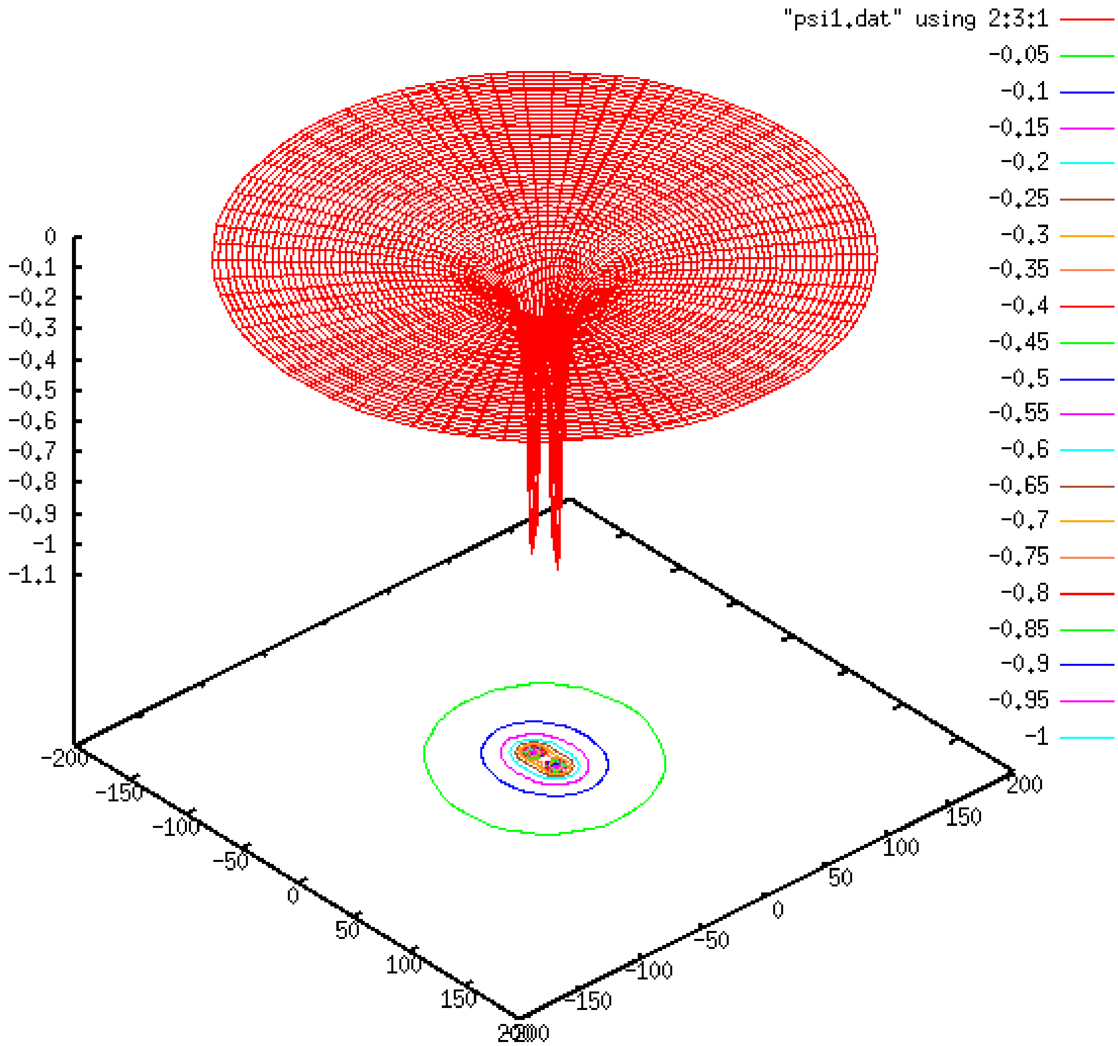

Figure 6.7: Equatorial slice of the field φ

second order convergence earlier. However, the error at the outer boundary has not improved much, as this error is instead due to the boundary conditions, which, being expressed in terms of r, assume a field generated at the origin, instead of two sources slightly offset on either side of it. Thus by instead doubling the radius of the outer boundary we get the error there to also decrease at second order, as seen in figure (6.12).

Satisfied that we are solving for the initial data we now set ω to a physically realistically value, usually about that needed to put the binary into a slightly eccentric

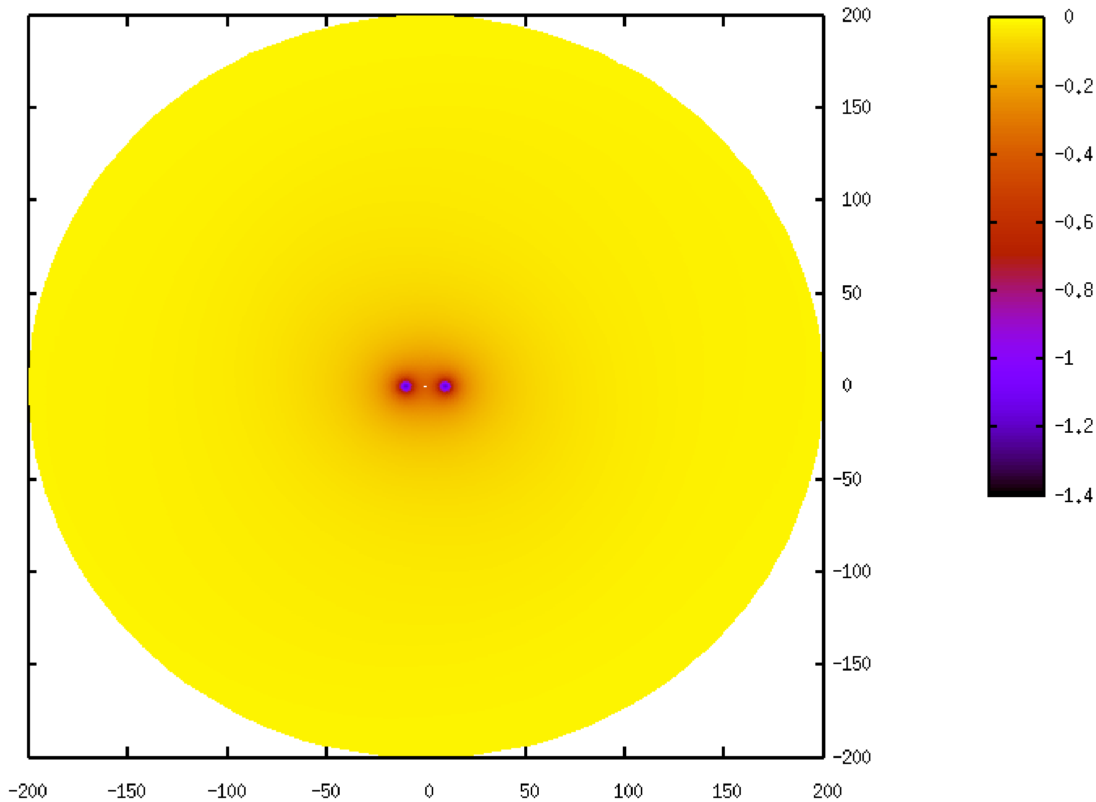

Figure 6.8: Top down view of the equatorial slice of the field φ

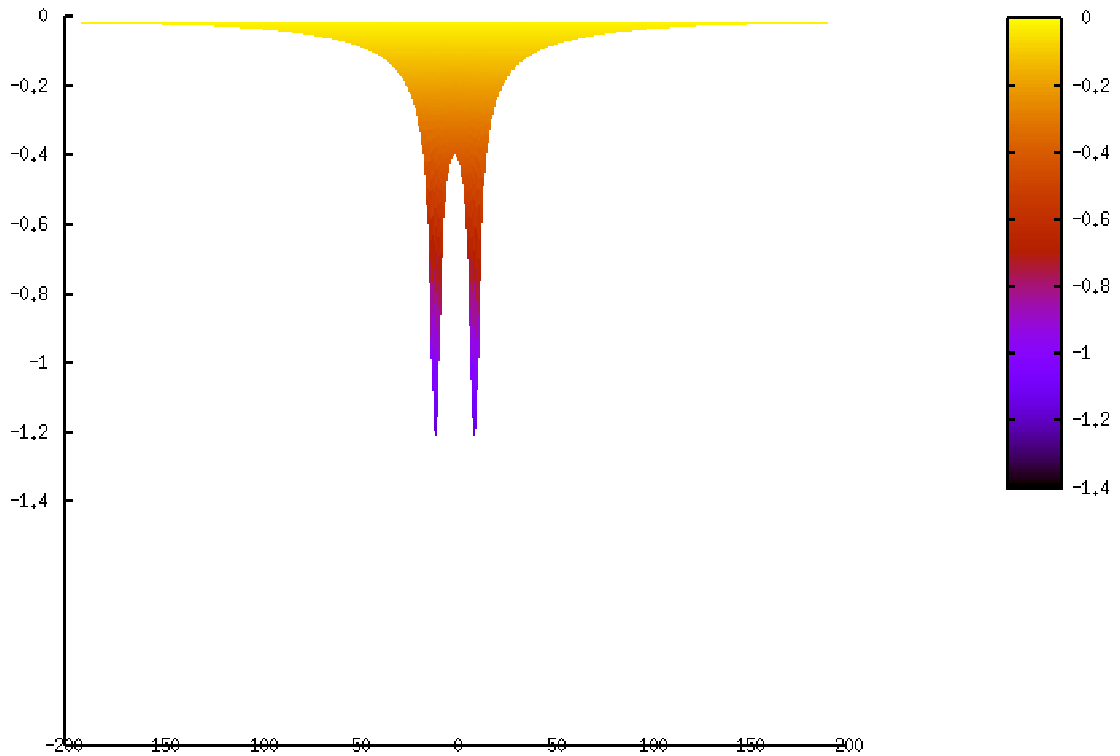

Figure 6.9: Side view of the equatorial slice of the field φ

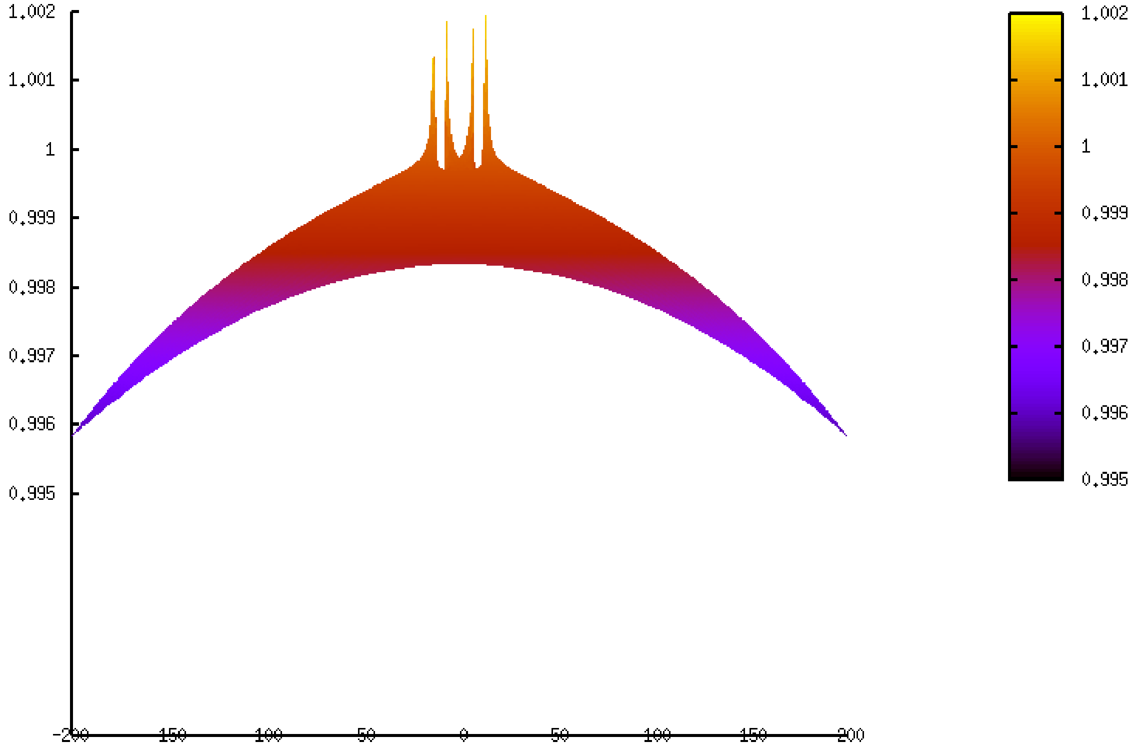

Figure 6.10: Side view of φ/φ_{an}

Keplerian orbit $\omega \simeq (2M/a^3)^{1/2}$. We show two example plots with this initial data: figure (6.13) and figure (6.14). In figure (6.13) we have taken the difference between φ and the "Newtonian" (not strictly Newtonian as there are additional contributions to the source density beyond the mass-energy density) solution $\varphi(\omega = 0)$ which now reveals the wave like component of the field. We note that this wave part of the field also has deep potential wells – this stems from the $(1/2)\partial_t^2\chi$ component of the 1PN terms as discussed in the post-Newtonian chapters. We can thus also divide through by the analytical solution, and the deep potential wells at the Newtonian and 1PN levels cancel out, leaving just the wave field, as we see in (6.14). We see that for this configuration the waves are a 6 percent oscillation about the lowest order Newtonian field.

The initial data assumes eternal circular orbits, and thus can not be the precise solution for a binary that has evolved into the orbital parameter set we choose. It will

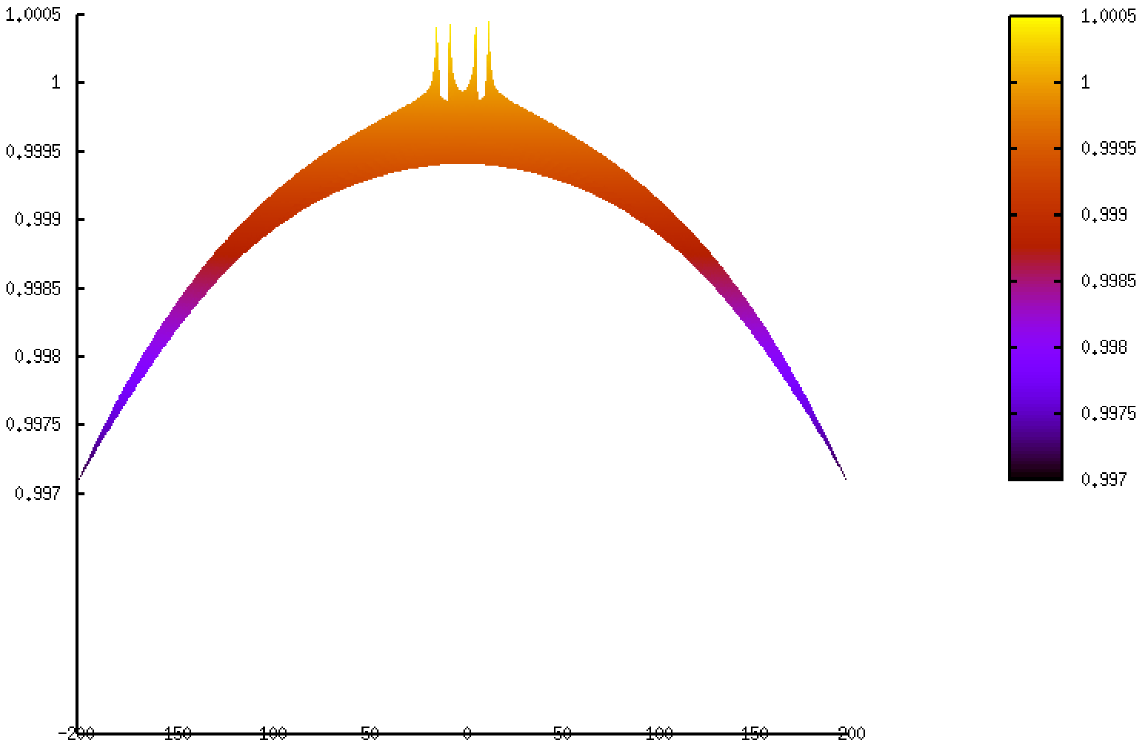

Figure 6.11: Side view of φ/φ_{an} at double resolution

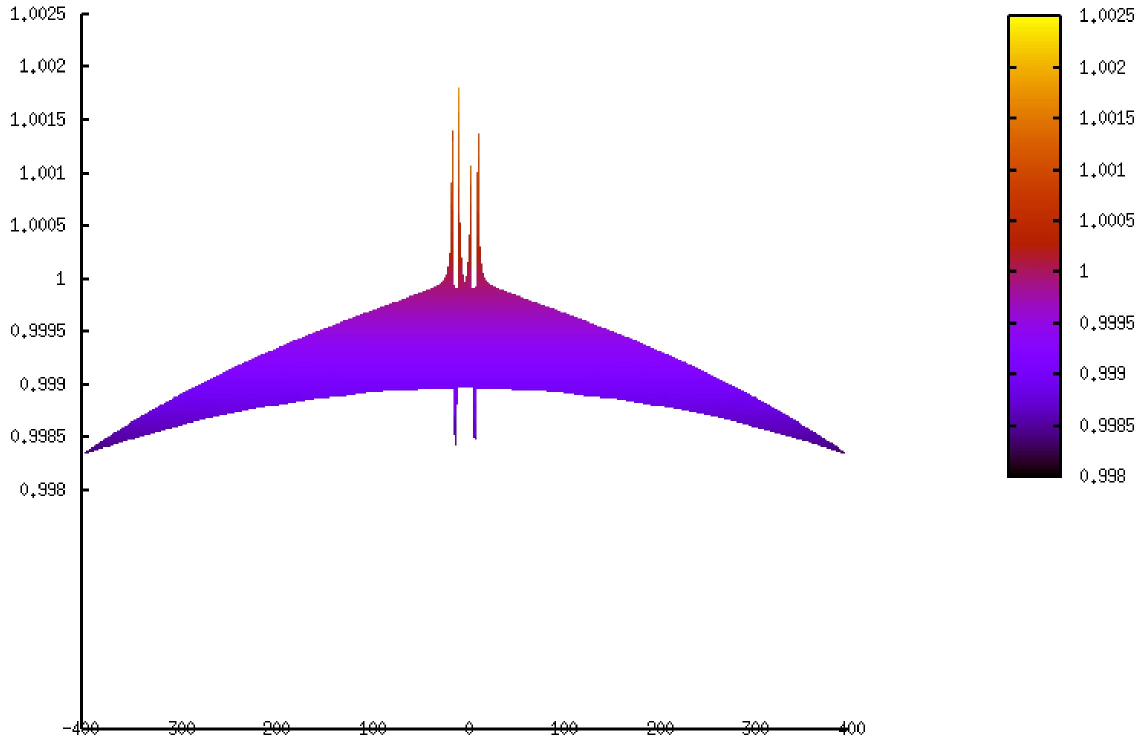

Figure 6.12: Side view of φ/φ_{an} with doubled outer boundary

be quite close to the true solution however, especially for binaries that are in quasi-circular orbit. The difference between the initial field and the true field will manifest during the time evolution as small transient waves that propagate off of the mesh. Indeed, as we watch the accelerations of the compact bodies after setting the code in motion we can see a small hiccup in the acceleration as the field quickly transitions from the initial composition to a dynamically realistic one.

With the initial data computed we are now ready to evolve the field forward in time. We first assume quasi-circular orbits and thus use the WRR approximation. We will use an implicit finite differencing of (6.26) (6.27 is finite differenced using the same method for the initial data). Implicit methods are stable and fast, as they generally have no Courant condition that restricts the size of the time step that can be used. In particular, as (6.26) resembles the Schrödinger equation, we will use the Crank-Nicholson method, which neither amplifies nor diminishes waves of any

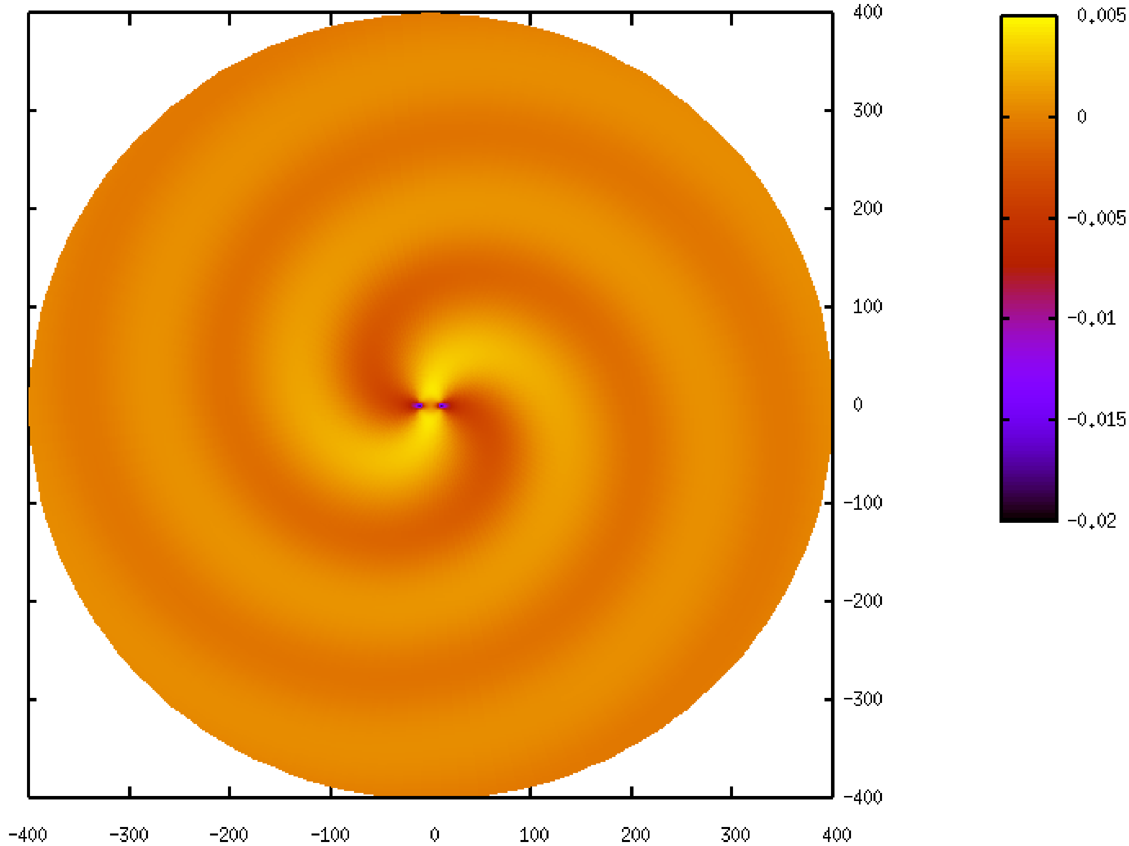

Figure 6.13: Topdown view of $\varphi - \varphi_{an}$ with nonzero ω

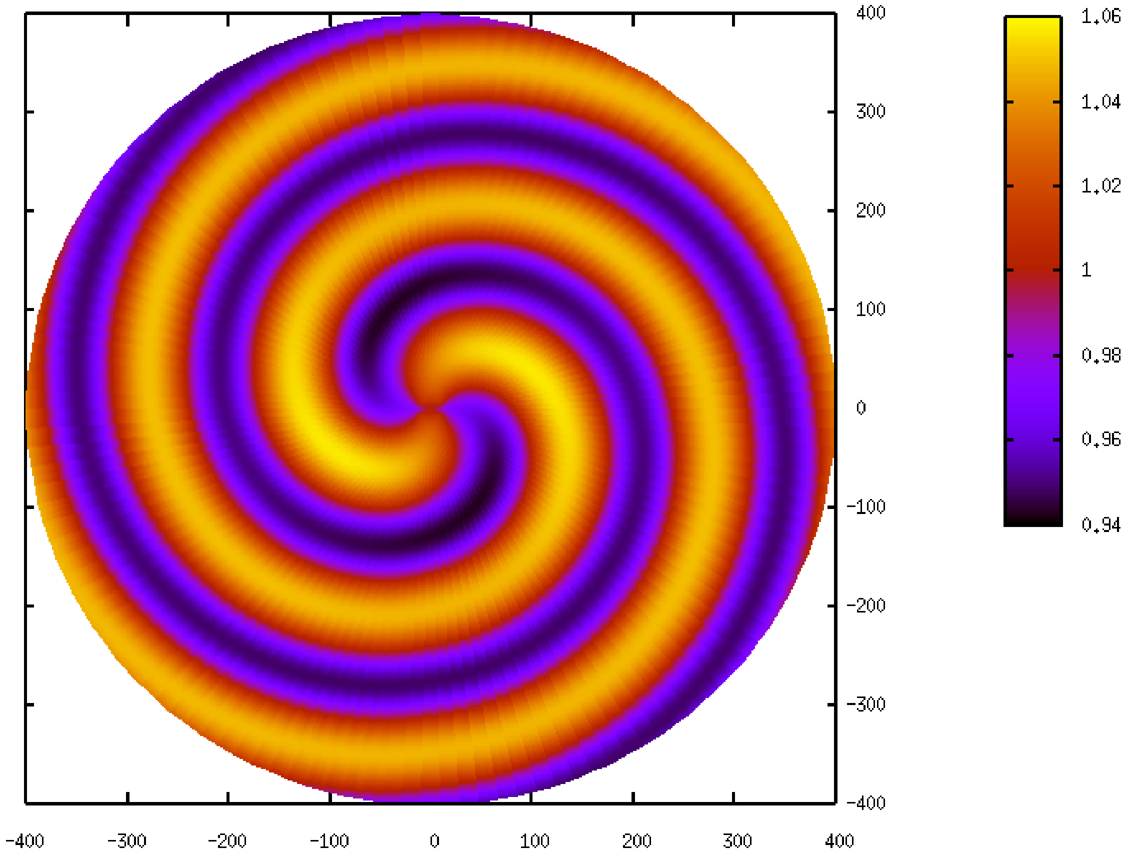

Figure 6.14: Topdown view of φ/φ_{an} with nonzero ω

frequency (see [146]). We get:

$$2im\omega(\varphi_i^{N+1} - \varphi_i^N) = \tag{6.32}$$

$$\frac{\Delta t}{2}\left[-\frac{(\varphi_{i+1}^{N+1} - 2\varphi_i^{N+1} + \varphi_{i-1}^{N+1})}{\Delta r^2} - \frac{(\varphi_{i+1}^{N+1} - \varphi_{i-1}^{N+1})}{r\Delta r} + (\frac{l(l+1)}{r^2} - m^2\omega^2 - im\dot{\omega})\varphi_i^{N+1}\right]$$
$$+\frac{\Delta t}{2}\left[-\frac{(\varphi_{i+1}^{N} - 2\varphi_i^{N} + \varphi_{i-1}^{N})}{\Delta r^2} - \frac{(\varphi_{i+1}^{N} - \varphi_{i-1}^{N})}{r\Delta r} + (\frac{l(l+1)}{r^2} - m^2\omega^2 - im\dot{\omega})\varphi_i^{N}\right]$$
$$+2\pi\Delta t(S_i^{N+1} + S_i^N)$$

This can be rearranged into linear algebra problem of the form:

$$A_i^j\varphi_j^{N+1} = B_i^k\varphi_k^N + 2\pi\Delta t(S_i^{N+1} + S_i^N) \tag{6.33}$$

which we can solve with the same Gauss-Jordan procedure we used before to find the initial data. Note that in addition to evenly splitting the field φ between the N and $N+1$ time steps we have also evenly averaged the source S between these two time steps. This is crucial as otherwise the field and source will be half of a time step out of sync, which gives rise to large anomalous accelerations that quickly cause the code to crash. We thus need to first solve for the position of the source at time step $N+1$ by using accelerations computed from the field at the N time step. A "molecular" diagram for this method of finite differencing is given in figure (6.15).

We first implemented the WRR approximation while building our code, and by using the implicit finite differencing scheme we have described we were able to compute long and accurate quasi-circular inspirals. Given this success of the Crank-Nicholson scheme, we wanted to adapt a version of it to the general second order in time differential equation given in (6.25). This will allow us to evolve binaries that retain some amount of eccentricity, and thus vary at the orbital time scale in the corotating

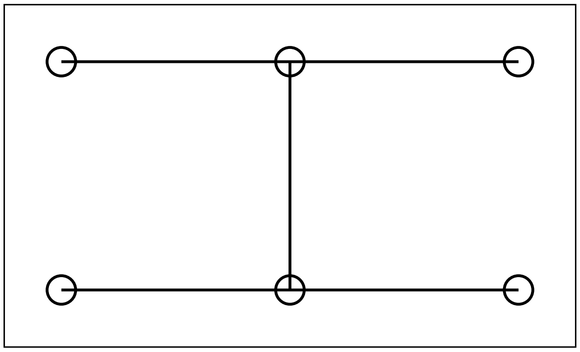

Figure 6.15: Molecular diagram for the Crank-Nicholson implicit finite differencing scheme. Spatial derivatives are taken and averaged at the N and $N+1$ time steps.

reference frame. The Crank-Nicholson scheme evenly balances the N and $N+1$ time steps, so we experimented with expanding it to a separation of two time steps $N+1$ and $N-1$ and then using the third, intermediate time step N to implement the second time derivative. The implicit finite differencing scheme we settled on is given by:

$$
\begin{aligned}
-(\varphi_i^{N+1} - 2\varphi_i^{N} + \varphi_i^{N-1}) + im\omega\Delta t(\varphi_i^{N+1} - \varphi_i^{N-1}) = \\
\frac{\Delta t^2}{2}\left[-\frac{(\varphi_{i+1}^{N+1} - 2\varphi_i^{N+1} + \varphi_{i-1}^{N+1})}{\Delta r^2} - \frac{(\varphi_{i+1}^{N+1} - \varphi_{i-1}^{N+1})}{r\Delta r} + (\frac{l(l+1)}{r^2} - m^2\omega^2 - im\dot{\omega})\varphi_i^{N+1}\right] \\
+\frac{\Delta t^2}{2}\left[-\frac{(\varphi_{i+1}^{N-1} - 2\varphi_i^{N-1} + \varphi_{i-1}^{N-1})}{\Delta r^2} - \frac{(\varphi_{i+1}^{N-1} - \varphi_{i-1}^{N-1})}{r\Delta r} + (\frac{l(l+1)}{r^2} - m^2\omega^2 - im\dot{\omega})\varphi_i^{N-1}\right] \\
+2\pi\Delta t^2(S_i^{N+1} + S_i^{N-1})
\end{aligned}
\tag{6.34}
$$

and a molecular representation is given in figure (6.16). We found that this method allowed us to stably and accurately evolve the field in the corotating reference frame. As noted in the paper we did get unexpected results for the rate of precession of binaries in Nordström's theory, which caused us to doubt this method at first. As a check we used it to evolve eccentric orbits in a simplified scalar wave system given

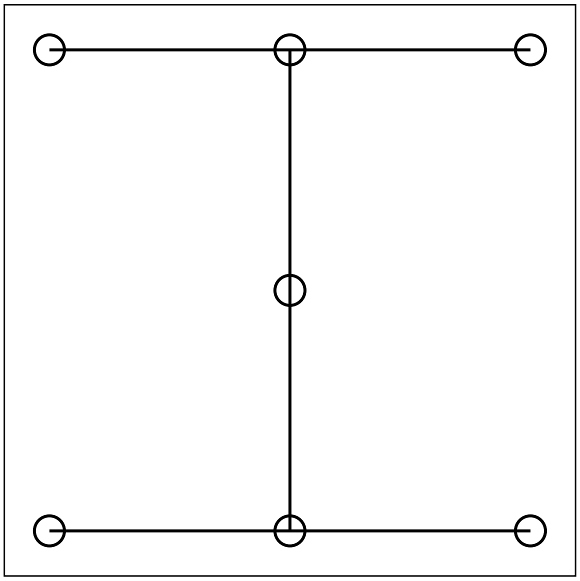

Figure 6.16: Molecular diagram for the modified, second order in time Crank-Nicholson differencing scheme. Spatial derivatives are taken and averaged at the $N-1$ and $N+1$ time steps.

by:

$$\Box\varphi = 4\pi\rho \tag{6.35}$$

We checked the numerical solution for the field against a post-Newtonian analysis of (6.35), and we found that the code accurately reproduced the 1PN corrections. This contributed in convincing us that the deviations we observed for Nordström's theory were real.

6.5 Matter Equations of Motion in Corotating Coordinates

We have now shown how to generate the source, decompose it into its spherical harmonic components, and use these to calculate the initial value of the scalar field φ. We now need to calculate how the matter moves in response to the metric so that we can evolve the field. In keeping with the hydro-without-hydro approximation we only need to keep track of the position, velocity, and acceleration of the center of mass of the compact bodies. As we describe in the papers, we make use of the conserved density ρ^* to this end:

$$\frac{dv_a^j}{dt} = \frac{1}{m_a}\int_a \rho^* \frac{dv^j}{dt} d^3x \tag{6.36}$$

We find the local coordinate acceleration dv^j/dt from the projected divergence of the stress energy tensor$Q^\alpha_\mu T^{\mu\nu}{}_{;\nu} = 0 = \rho h u^\nu u^\alpha{}_{;\nu} + Q^{\alpha\nu} p_{,\nu}$. As we have seen, this reduces to:

$$\frac{dv^j}{dt} = -\Gamma^j_{\alpha\beta} v^\alpha v^\beta - v^j \frac{1}{u^0}\frac{du^0}{dt} - \frac{1}{\rho h} Q^{j\nu} p_{,\nu} \tag{6.37}$$

Since we evolve the field in a corotating reference frame we also need to evaluate this expression in corotating coordinates. We will first evaluate the connection coefficients. We start with the Nordström metric in an inertial reference frame $g_{\mu\nu} = (1+\varphi)^2 \eta_{\mu\nu}$ and transform it into the corotating reference frame in the usual manner: $\bar{g}_{\bar{\mu}\bar{\nu}} = (\partial x^\alpha/\partial \bar{x}^\mu)(\partial x^\beta/\partial \bar{x}^\nu) g_{\alpha\beta}$. We let the $\hat{z}$ direction be the axis of rotation so the x and y coordinates transform as:

$$\bar{x} = \cos\Omega(t)x + \sin\Omega(t)y \tag{6.38}$$

$$\bar{y} = -\sin\Omega(t)x + \cos\Omega(t)y \tag{6.39}$$

with $\Omega(t) = \int \omega(t)dt$ (since we will need to evolve $\omega(t)$ in order to keep the reference frame synced to the motion of the compact bodies). This gives rise to the metric (dropping the bar notation from here on out):

$$g_{\mu\nu} = (1+\varphi)^2 \begin{pmatrix} -1+\omega^2(x^2+y^2) & -\omega y & \omega x & 0 \\ -\omega y & 1 & 0 & 0 \\ \omega x & 0 & 1 & 0 \\ 0 & 0 & 0 & 1 \end{pmatrix} \tag{6.40}$$

Raising the indices gives us:

$$g^{\mu\nu} = (1+\varphi)^{-2} \begin{pmatrix} -1 & -\omega y & \omega x & 0 \\ -\omega y & 1-\omega^2 y^2 & \omega^2 xy & 0 \\ \omega x & \omega^2 xy & 1-\omega^2 x^2 & 0 \\ 0 & 0 & 0 & 1 \end{pmatrix} \tag{6.41}$$

On a side note, we see that we can interpret this metric in the ADM formalism. We see that we have: $\beta_x = -y\omega(1+\varphi)^2$ and $\beta_y = x\omega(1+\varphi)^2$. The raised index shift is then $\beta^x = -y\omega$ and likewise for $\beta^y = x\omega$, so that the lapse is $\alpha = (1+\varphi)$, and the spatial metric is given by: $\gamma_{ij} = (1+\varphi)^2\eta_{ij}$.

We now need to calculate the connection coefficients in order to find the acceleration. We find:

$$\Gamma^x_{tt} = -\omega^2 x - y\dot{\omega} + [-y\omega(1-\omega^2(x^2+y^2))\partial_t\varphi \tag{6.42}$$

$$+(1-\omega^2(x^2+2y^2)+\omega^4 y^2(x^2+y^2))\partial_x\varphi$$

$$+xy\omega^2(1-\omega^2(x^2+y^2))\partial_y\varphi]/(1+\varphi)$$

$$\Gamma^y_{tt} = -\omega^2 y + x\dot{\omega} + [x\omega(1-\omega^2(x^2+y^2))\partial_t\varphi \tag{6.43}$$

$$+xy\omega^2(1-\omega^2(x^2+y^2))\partial_x\varphi$$

$$+(1-\omega^2(2x^2+y^2)+\omega^4 x^2(x^2+y^2))\partial_y\varphi]/(1+\varphi)$$

and

$$\Gamma^x_{tx} = [(1-\omega^2y^2)\partial_t\varphi + y\omega(1-\omega^2y^2)\partial_x\varphi \tag{6.44}$$
$$+xy^2\omega^3\partial_y\varphi]/(1+\varphi)$$
$$\Gamma^x_{ty} = -\omega + [xy\omega^2\partial_t\varphi - x\omega(1-\omega^2y^2)\partial_x\varphi \tag{6.45}$$
$$-yx^2\omega^3\partial_y\varphi]/(1+\varphi)$$
$$\Gamma^x_{xx} = [y\omega\partial_t\varphi + (1+\omega^2y^2)\partial_x\varphi \tag{6.46}$$
$$-xy\omega^2\partial_y\varphi]/(1+\varphi)$$
$$\Gamma^x_{xy} = \partial_y\varphi/(1+\varphi) \tag{6.47}$$
$$\Gamma^x_{yy} = [y\omega\partial_t\varphi - (1-\omega^2y^2)\partial_x\varphi \tag{6.48}$$
$$-xy\omega^2\partial_y\varphi]/(1+\varphi)$$

and

$$\Gamma^y_{tx} = \omega + [xy\omega^2\partial_t\varphi + xy^2\omega^3\partial_x\varphi \tag{6.49}$$
$$+y\omega(1-\omega^2x^2)\partial_y\varphi]/(1+\varphi)$$
$$\Gamma^y_{ty} = [(1-\omega^2x^2)\partial_t\varphi - yx^2\omega^3\partial_x\varphi \tag{6.50}$$
$$-x\omega(1-\omega^2x^2)\partial_y\varphi]/(1+\varphi)$$
$$\Gamma^y_{xx} = [-x\omega\partial_t\varphi - xy\omega^2\partial_x\varphi \tag{6.51}$$
$$-(1-\omega^2x^2)\partial_y\varphi]/(1+\varphi)$$
$$\Gamma^y_{xy} = \partial_x\varphi/(1+\varphi) \tag{6.52}$$
$$\Gamma^y_{yy} = [-x\omega\partial_t\varphi - xy\omega^2\partial_x\varphi \tag{6.53}$$
$$+(1+\omega^2x^2)\partial_y\varphi]/(1+\varphi)$$

The connections coefficients then need to be multiplied by the coordinate velocities of the matter. We set the stars up to be irrotational as NS and BH binaries do not have sufficient time to tidally lock (see [154]). We set the binary up so that it is instantaneously align along the x axis. In the inertial reference frame the equal mass stars are situated at $\pm r_0$ from the origin, and have angular velocities ω, and, if the orbit retains a slight amount of eccentricity, a small radial velocity $\dot{r}_0$. The velocities in the co-rotating reference frame are then $v^x = y\omega - \dot{r_0}$ and $v^y = -(x + r_0)\omega$. This thus allows us to solve for the first term on the right hand side of (6.37).

To solve for the second term on the RHS of (6.37) we need to compute u^0 via $g_{\mu\nu}u^\mu u^\nu = -1$. We find the same value in the co-rotating frame as in the original inertial reference frame:

$$u^0 = \frac{1}{1+\varphi}\frac{1}{\sqrt{1-\dot{r_0}^2 - r_0^2\omega^2}} = \frac{1}{1+\varphi}\frac{1}{\sqrt{1-\bar{v}^2}} \tag{6.54}$$

where $\bar{v}$ is the inertial frame velocity: $\bar{v}^2 = r_0^2\omega^2 + \dot{r}_0^2$. We can then solve for:

$$-\rho^*(u^0)^{-1}v^j\frac{du^0}{dt} = \rho^* v^j\left[\frac{1}{1+\varphi}\frac{d\varphi}{dt} - \frac{1}{(1-\bar{v}^2)}(\ddot{r_0}\dot{r_0} + r_0\omega(\dot{r_0}\omega + r_0\dot{\omega}))\right] \tag{6.55}$$

Finally we solve for the third term on the RHS of (6.37). We find:

$$\begin{aligned} -(u^0)^{-2}\frac{\rho^*}{\rho h}Q^{x\nu}p_{,\nu} &= -\frac{(1+\varphi)^3}{\sqrt{1-\bar{v}^2}(1+\varepsilon+p/\rho)}v^x\frac{dp}{dt} \\ -\frac{\sqrt{1-\bar{v}^2}(1+\varphi)^3}{(1+\varepsilon+p/\rho)}&(-y\omega p_{,t} + (1-y^2\omega^2)p_{,x} + xy\omega^2 p_{,y}) \end{aligned} \tag{6.56}$$

and

$$\begin{aligned} -(u^0)^{-2}\frac{\rho^*}{\rho h}Q^{y\nu}p_{,\nu} &= -\frac{(1+\varphi)^3}{\sqrt{1-\bar{v}^2}(1+\varepsilon+p/\rho)}v^y\frac{dp}{dt} \\ -\frac{\sqrt{1-\bar{v}^2}(1+\varphi)^3}{(1+\varepsilon+p/\rho)}&(x\omega p_{,t} + xy\omega^2 p_{,x} + (1-x^2\omega^2)p_{,y}) \end{aligned} \tag{6.57}$$

With the local acceleration (6.37) expanded we now need to solve for it numerically throughout the volume of the compact body in order to find the net acceleration of the body: (6.36). To do so we need to find the discretized derivatives of φ. As we discussed in the numerical paper, finding these accurately is somewhat more involved than is apparent at first. We discuss the details in the next section.

6.6 Spherical Volume Integrals

We used an analytic source distribution ρ_{an} with an analytic Newtonian potential φ_{an} in section 6.4 to show that our numerical methods converge at second order to the correct solution. We now make use of these analytic solutions to develop an efficient way to take the volume integrals of field derivatives in a two body system. As noted in the numerical paper the straight forward method of calculating the second order accurate field derivatives in the volume of the body does not give accurate results unless unreasonably high mesh resolutions are used. We find cases where resolutions that are sufficient to resolve the field to within one percent error also give rise to 100 percent errors in the acceleration (which should reproduce the inverse square law for the test case where $\omega = 0$). This error arises because analytically the derivatives of the self field integrate up to zero, but numerically they will contribute a small error, which can swamp the small correct acceleration at large separations. We can show that if we plug the analytical values of the field into the grid points and then take the second order accurate derivatives that we get essentially the same result. However, if we plug in the analytic values for the derivatives and integrate we get quite accurate results. We thus need to evaluate the derivatives more accurately than second order.

Our solution is to make use of higher order interpolation methods to find more accurate derivatives at the grid points. We will fit the field to a polynomial that stretches through the several grid points on either side of the point where we wish to find the derivative. We will then take the derivative of the polynomial at that location to produce a more accurate result. Following Boyd [147] we the Lagrange

Interpolation Formula, which fits a N degree polynomial $P_N(x)$ to a function $f(x)$ via $N+1$ sample points:

$$P_N(x) = \sum_{i=0}^{N} f(x_i) C_i(x) \tag{6.58}$$

where

$$C_i(x) = \prod_{j=0, j\neq i}^{N} \frac{x - x_j}{x_i - x_j} \tag{6.59}$$

which follows $C_i(x_j) = \delta_i^j$. Although $P_N(x)$ is guaranteed to match $f(x)$ at the sample points, it can vary wildly from them in between as seen in figure (6.17), where we have fit to the "Witch of Agnesi" function $f(x) = 1/(1+x^2)$ with evenly spaced sample points. The interpolation fits quite well in the center, but deviates wildly towards the edges, and these deviations grow quickly in size as the number of sample points is increased. This is due to the poles in the function that occur at $x = \pm i$. Thus in general one needs to be cautious when making use of interpolations, however in our case we only make use of the interpolation in the very center, where the interpolation is essentially always guaranteed to be a good fit. This is what we find in our code: the use of higher order polynomials greatly increases the accuracy of our volume integrals. We give a list below of the finite differenced derivatives of increasing accuracy as computed via the interpolation polynomials. We stop at 12th order as this produces accelerations that are at the same accuracy as we solve for the field.

- 2nd order:

$$\partial_x \psi = (-\psi_{i-1} + \psi_{i+1})/(2dx) \tag{6.60}$$

- 4th order:

$$\partial_x \psi = (\psi_{i-2} - 8\psi_{i-1} + 8\psi_{i+1} - \psi_{i+2})/(12dx) \tag{6.61}$$

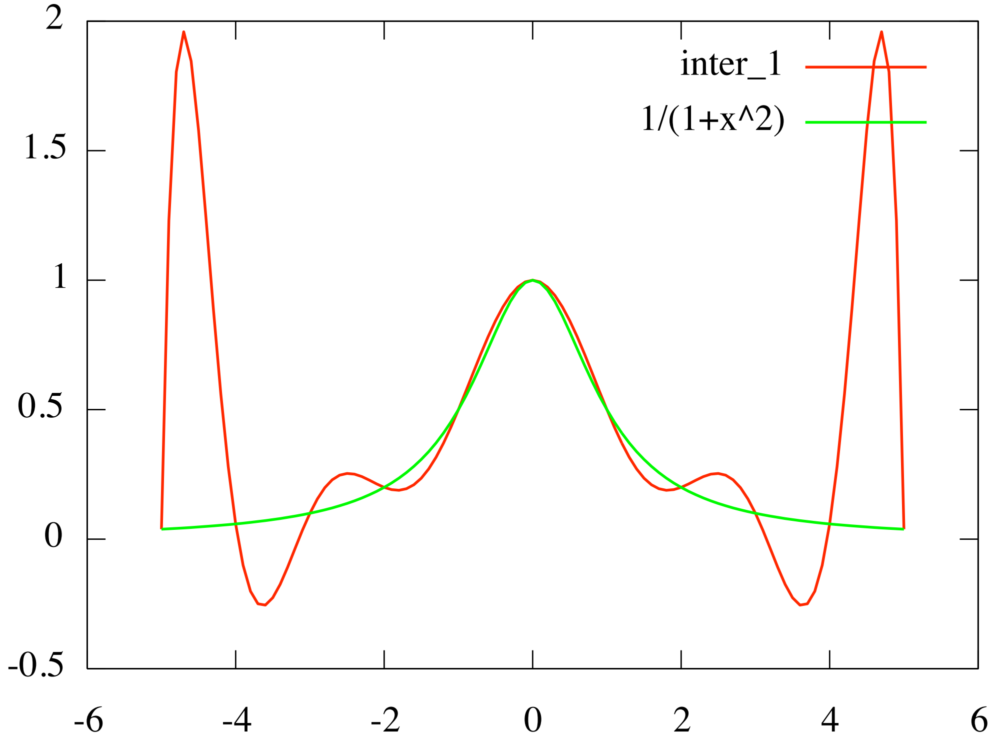

Figure 6.17: $1/(1 + x^2)$ and a regular spacing interpolation.

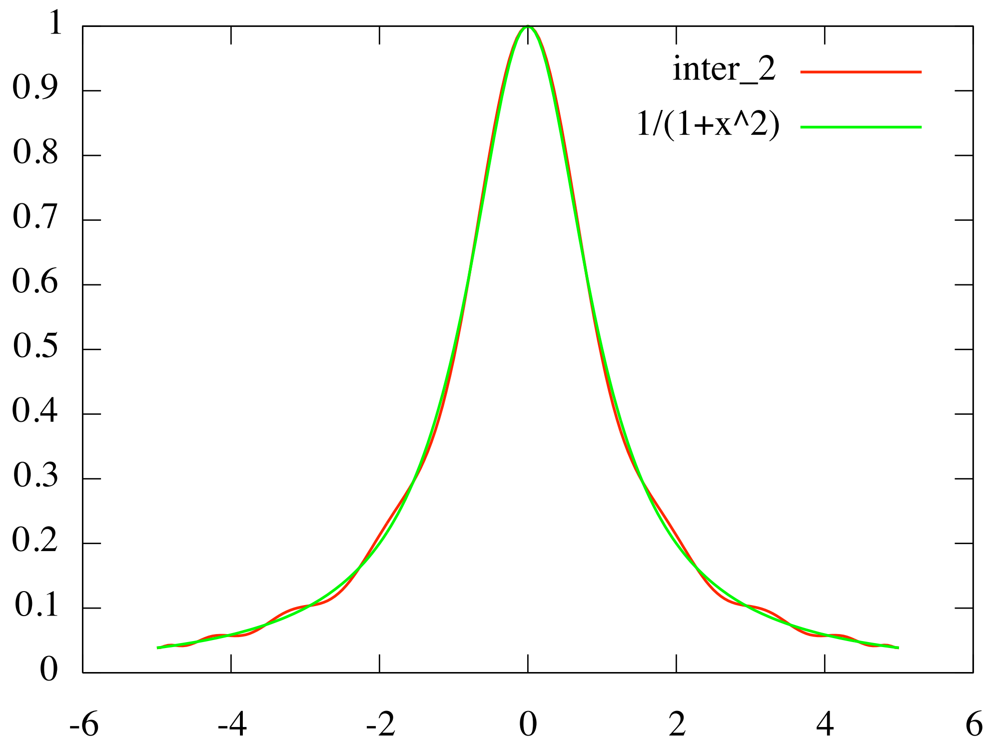

Figure 6.18: $1/(1+x^2)$ and end-weighted interpolation.

- 6th Order:

$$\partial_x \psi = (-\psi_{i-3} + 9\psi_{i-2} - 45\psi_{i-1} \\ +45\psi_{i+1} - 9\psi_{i+2} + \psi_{i+3})/(60dx) \tag{6.62}$$

- 8th Order:

$$\partial_x \psi = (3\psi_{i-4} - 32\psi_{i-3} + 168\psi_{i-2} - 672\psi_{i-1} \\ +672\psi_{i+1} - 168\psi_{i+2} + 32\psi_{i+3} - 3\psi_{i+4})/(840dx) \tag{6.63}$$

- 10th Order:

$$\partial_x \psi = (-2\psi_{i-5} + 25\psi_{i-4} - 150\psi_{i-3} + 600\psi_{i-2} \\ -2100\psi_{i-1} + 2100\psi_{i+1} - 600\psi_{i+2} \\ +150\psi_{i+3} - 25\psi_{i+4} + 2\psi_{i+5})/(2520dx) \tag{6.64}$$

- 12th Order:

$$\partial_x \psi = (5\psi_{i-6} - 72\psi_{i-5} + 495\psi_{i-4} - 2200\psi_{i-3} \\ +7425\psi_{i-2} - 23760\psi_{i-1} + 23760\psi_{i+1} \\ -7425\psi_{i+2} + 2200\psi_{i+3} - 495\psi_{i+4} \\ +72\psi_{i+5} - 5\psi_{i+6})/(27720dx) \tag{6.65}$$

Given the success we have had using high order polynomial fits, they will be tempting to use again. We thus note that we can sample points such that $P_N(x)$ converges over the entire range. We do this by choosing a higher density of sample points at the ends of the range. The precise points x_i we sample from are the roots of a Chebyshev polynomial over the range under consideration:

$$x_i \equiv -\cos\left[\frac{(2i-1)\pi}{2(N+1)}\right] \tag{6.66}$$

An example of this sampling and the accurate fit it gives is shown in figure (6.18).

6.7 Adaptation to Parallel Architectures

The code we have described was originally written for a standard single processor machine, but we have also adapted it to a parallel architecture. This allows us to use much more memory, allowing for a finer mesh and greater precision, and to run our simulations much more quickly. The implementation is somewhat involved and we describe it here.

In the parallel architecture types that we have used the different processors (or nodes) each have their own separate memory, instead of drawing from a common source. We will thus need to divide up the mesh so that different subsets of it are processed on different nodes. In general we also want to try and send as little information between nodes as possible, as this is generally slower than local processing, and thus forms a bottleneck. Using our spherical coordinate system, we generally have two simple options for splitting up the mesh. One can either split the mesh into a series of concentric radial shells, with different nodes handling the different shells. Alternatively one can split the problem up by sending the different spherical harmonic components of the field φ_{lm} to different nodes – this is the method we have implemented.

If we implement a linearized version of our equations on the parallel architecture then we get excellent performance – essentially the use of N nodes allows the code to run N times faster. This is because in the linearized version all of the φ_{lm} components can be processed (almost) independently of each other. However in the nonlinear version there is the need for a moderate amount of information passing between nodes, as the local content of the field in a coordinate basis $\varphi(r^i, \theta^j, \phi^k)$ is needed but the various $\varphi_{lm}(r^i)$ terms from which it can synthesized are stored on different nodes. Consider for instance the decomposition of the source:

$$S_{lm}(t, r) = \int d\Omega Y^*_{lm}(\theta, \phi)[\sqrt{1 - v^2}\rho^*(1 + \varepsilon - 3p/\rho)] \tag{6.67}$$

This is almost in a linear form, as we use the same distribution for ρ^* as we found in section (6.2). However, there are the additional source terms ε, ρ, and p which are defined in terms of the conserved density and the scalar field: $\rho = \rho^*(1 - v^2)^{1/2}(1 + \varphi)^{-3}$, (and likewise for ε, and p via the polytropic equations of state). We thus need to know the local value of the field φ to do the decomposition. However, this also shows a way to linearize the system without too much error: instead of computing the value of ρ using the true value of the scalar field φ we can use the Newtonian approximation instead: φ_{Newton}. In testing with commonly used binary parameters we find that this approximation produces errors on the order of 2 percent in the accelerations of the bodies, but the code can run considerably faster. A similar approximation needs to be made with respect to the accelerations as computed in section (6.5). This is also a useful tactic for constructing the initial data and evolving the system in the nonlinear case, as we can solve the system iteratively, with the first iteration supplied by the Newtonian approximation of the field. The degree to which the information passing serves as a bottleneck is also reduced for Nordström's theory since we only need to know the coordinate values of the field in the small volumes that contain the compact bodies.

However, in the future when we apply our framework to the binary problem in general relativity we will likely need the local values for the relevant fields everywhere within the computational domain. Information passing between nodes would then become a larger bottleneck. It is thus useful to also consider splitting the mesh radially, so that for N radial mesh points and M nodes, each node will handle a N/M chunk of the radial calculations. In this scheme each node would also do all of the spherical harmonic calculations for its radial sector, and thus the local values for the field quantities can be calculated locally, without need for information passing (there in general will be information passing at the surfaces of the shells to each other, but this is not nearly as demanding as sending the entire contents of the field to all nodes).

There are significant disadvantages to this method however. We use implicit finite differencing methods to both create the initial data for φ and to solve the 1+1 problem and evolve the field forward in time. The standard implementation of this method requires the entire span of radial mesh points, although it is possible that a stable and accurate work-around could be developed. If this can't be done we would need to switch explicit finite differencing methods, along with a less accurate method for finding the initial data. This would require smaller time steps in order to satisfy the courant condition and make the evolution stable, thus erasing at the least some of the gains earned by avoiding information passing.

Our current disposition is to apply the specific parallelization methods we have developed for Nordström's theory to the problem in general relativity, thus probably necessitating longer run times. A careful examination of the discretization of the equations involved and thorough experimentation will be necessary to determine the best way to implement general relativity in corotating spherical coordinates on a parallel architecture.

6.8 Acceleration of Massive Bodies in Nordström's Theory

One of the interesting and unexpected results we found by modeling binary inspirals in Nordström's 2nd theory is that Nordström's theory violates the Strong Equivalence Principle (SEP) at 2PN order, thus causing deviations from the expected 1PN behavior for compact bodies with significant self gravitational energy. Strictly speaking we have not proven this, although the empirical evidence seems compelling and since we also should expect (in hindsight) for Nordström's theory to violate the SEP at some level. Proving that Nordström's theory violates the SEP at 2PN thus provides material for a quick follow up paper to follow this thesis. We have begun work on the topic already, and in this section we show that Nordström's theory does not violate the SEP due to 1PN terms – as expected – and we begin the investigation of 2PN terms.

As we wish to show that Nordström's theory violates the SEP at 2PN, any demonstration that it does so is sufficient. We are thus free to pick as simple of a test problem as possible in attempt to show this. We will thus consider the acceleration of a compact body due to a simple perturbative accelerating field $\delta\varphi$ that asymptotically has a constant gradient: $\delta\varphi = Cx$ for large x. If Nordström's theory does not violate the SEP at 2PN, then the massive compact body will accelerate at the same rate as a test body in response to $\delta\varphi$. We thus need to calculate the geodesic motion of a test body:

$$\frac{du^x}{d\tau} = -\Gamma^x_{\alpha\beta} u^\alpha u^\beta \tag{6.68}$$

For simplicity we will only calculate the initial acceleration, and we will set the initial velocity equal to zero. We also switch from the acceleration of the 4-velocity to the coordinate acceleration, in keeping with our earlier methods. We find:

$$\frac{dv^x}{dt} = -\Gamma^x_{00} = \frac{-\partial_x \varphi}{(1+\varphi)} \tag{6.69}$$

We will rewrite the main equations for Nordström's theory and modify them to our purposes here. As usual we have:

$$g_{\mu\nu} = (1+\varphi)^2 \eta_{\mu\nu} \tag{6.70}$$

and

$$\Box\varphi = 4\pi(1+\varphi)^3(\rho + \rho\varepsilon - 3p) \tag{6.71}$$

which we can rewrite by using the conserved density ρ^*:

$$\Box\varphi = 4\pi\rho^*(1-v^2)^{1/2}(1+\varepsilon - 3p/\rho) \tag{6.72}$$

In order to simplify further we will use a polytropic equation of state ($p = \kappa\rho^\Gamma$ and $\varepsilon = \kappa\rho^{\Gamma-1}/(\Gamma-1)$), and set $\Gamma = 2$. We thus get:

$$\Box\varphi = 4\pi\rho^*(1-v^2)^{1/2}(1-2\kappa\rho) \tag{6.73}$$

Since we are solving for the initial acceleration when the velocity is zero we will drop the velocity from this term henceforth (although in general we can't drop time derivatives of the velocity).

We set the general solution to be equal to the sum $\varphi = \varphi_0 + \delta\varphi$ where φ_0 solves the single star equation:

$$\Box\varphi_0 \Rightarrow \frac{1}{r^2}\partial_r(r^2\varphi_0) = 4\pi\rho^*(1-2\kappa\rho^*(1+\varphi_0)^{-3}) \tag{6.74}$$

and $\delta\varphi$ contains the accelerating field $\delta\varphi^{(2)} = Cx$ and perturbative corrections. One assumption we will use is that the solution for ρ^* is unchanged when we move the isolated star into the accelerating field - i.e. not only is the integral $\int \rho^* d^3x = m^*$ conserved but the radial profile $\rho^*(r)$ is unchanged as well (and on a side note we will solve for the isolated star solution using the iterative methods discussed in the first section of this chapter).

The general solution for φ_0 is:

$$\varphi_0(x,t) = -\int \frac{\rho^*(x',t)[1-2\kappa\rho^*(x',t)(1+\varphi_0(x',t))^{-3}]}{|x-x'|} d^3x' \tag{6.75}$$

It turns out that it is useful to expand this solution order by order: $\varphi_0 = \varphi_0^{(2)} + \varphi_0^{(4)} + ...$, i.e.:

$$\varphi_0^{(2)}(x,t) = -\int \frac{\rho^*(x',t)}{|x-x'|} d^3x' \tag{6.76}$$

$$\varphi_0^{(4)}(x,t) = 2\kappa \int \frac{(\rho^*(x',t))^2}{|x-x'|} d^3x' \tag{6.77}$$

Likewise we will also need the superpotential, which will also need to be expanded: $\chi_0 = \chi_0^{(2)} + \chi_0^{(4)} + ...$

$$\chi_0(x,t) = -\int \rho^{*\prime}[1-2\kappa\rho^{*\prime}(1+\varphi_0')^{-3}]|x-x'|d^3x' \tag{6.78}$$

$$\chi_0^{(2)}(x,t) = -\int \rho^{*\prime}|x-x'|d^3x' \tag{6.79}$$

$$\chi_0^{(4)}(x,t) = 2\kappa \int (\rho^{*\prime})^2|x-x'|d^3x' \tag{6.80}$$

We now need to subtract equation (6.74) from (6.73) and solve for $\delta\varphi$:

$$-\partial_t^2(\varphi_0 + \delta\varphi) + \nabla^2\delta\varphi = \tag{6.81}$$

$$-8\pi\rho^*\kappa\rho^*((1+\varphi_0+\delta\varphi)^{-3} - (1+\varphi_0)^{-3})$$

There does not appear to be a pure analytic method to solve (6.81), so we will do a post-Newtonian type expansion as usual. We set $\delta\varphi^{(2)} = Cx$. We thus find for the 1PN correction $\delta\varphi^{(4)}$:

$$-\partial_t^2\varphi_0^{(2)} + \nabla^2\delta\varphi^{(4)} = 0 \tag{6.82}$$

and we will later solve for the 2PN correction:

$$-\partial_t^2(\varphi_0^{(4)} + \delta\varphi^{(4)}) + \nabla^2\delta\varphi^{(6)} = 8\pi\rho^*\kappa\rho^* 3\delta\varphi^{(2)} \tag{6.83}$$

We use $\chi_0^{(2)}$ to solve for $\delta\varphi^{(4)}$:

$$\delta\varphi^{(4)} = \frac{1}{2}\partial_t^2\chi_0^{(2)} = \frac{1}{2}(A + B - \Phi_1) \tag{6.84}$$

We now need to solve for the acceleration of the compact body to 1PN order. As usual, we will integrate up the coordinate acceleration with the conserved density serving as the weighting:

$$\frac{dv_a^x}{dt} = \frac{1}{m_a^*}\int_a \rho^*\frac{dv^x}{dt}d^3x \tag{6.85}$$

We get the local acceleration by operating on $T^{\mu\nu}{}_{;\nu} = 0$ with the projection operator $Q_\mu^j = u^j u_\alpha + \delta_\alpha^j$:

$$\rho^*\frac{dv^j}{dt} = -\rho^*\Gamma^j_{\alpha\beta}v^\alpha v^\beta - (u^0)^{-1}\rho^* v^j\frac{du^0}{dt} - (u^0)^{-2}\frac{\rho^*}{\rho h}Q^{j\nu}p_{,\nu} \tag{6.86}$$

With the initial velocity equal to zero this becomes:

$$\rho^*\frac{dv^x}{dt} = -\rho^*\Gamma^x_{00} - (u^0)^{-2}\frac{\rho^*}{\rho h}g^{x\nu}p_{,\nu} \tag{6.87}$$

To first post-Newtonian order Γ^j_{00} is given by:

$$\Gamma^j_{00} \sim \varphi^{(2)}_{0,x}(1-\delta\varphi^{(2)}-\varphi^{(2)}_0)+\delta\varphi^{(2)}_{,x}(1-\delta\varphi^{(2)}-\varphi^{(2)}_0)+\varphi^{(4)}_{0,x}+\delta\varphi^{(4)}_{,x} \tag{6.88}$$

which reduces to

$$\Gamma^j_{00} \sim -\varphi^{(2)}_{0,x}\delta\varphi^{(2)}+\delta\varphi^{(2)}_{,x}(1-\delta\varphi^{(2)}-\varphi^{(2)}_0)+\frac{1}{2}B_{,x} \tag{6.89}$$

after the symmetric terms integrate to zero. With

$$B=\int\frac{\rho^{*\prime}}{|x-x'|}(x^i-x^{i\prime})\frac{dv^{i\prime}}{dt}d^3x' \tag{6.90}$$

we find

$$\frac{1}{2}B_{,x}=\frac{1}{2}\frac{2}{3}\delta\varphi^{(2)}_{,x}\varphi^{(2)}_0 \tag{6.91}$$

The pressure term reduces to:

$$-(u^0)^{-2}\frac{\rho^*}{\rho h}g^{x\nu}p_{,\nu}\Rightarrow(1+3\varphi)\rho^*\varphi^{(2)}_{0,x}\Rightarrow 3\delta\varphi^{(2)}\rho^*\varphi^{(2)}_{0,x} \tag{6.92}$$

Adding all the terms together we find:

$$\frac{dv^x_a}{dt}=\frac{1}{m^*_a}\int_a\rho^*\left[-\delta\varphi^{(2)}_{,x}(1-\delta\varphi^{(2)})+\varphi^{(2)}_{0,x}\delta\varphi^{(2)}+\delta\varphi^{(2)}_{,x}\varphi^{(2)}_0-\frac{1}{3}\delta\varphi^{(2)}_{,x}\varphi^{(2)}_0+3\varphi^{(2)}_{0,x}\delta\varphi^{(2)}\right]d^3x \tag{6.93}$$

We have

$$\int_a\rho^*\varphi^{(2)}_{0,x}\delta\varphi^{(2)}d^3x=-\frac{1}{6}\int_a\rho^*\delta\varphi^{(2)}_{,x}\varphi^{(2)}_0d^3x \tag{6.94}$$

It thus all reduces to:

$$\frac{dv^x_a}{dt}=\frac{-1}{m^*_a}\int_a\rho^*\delta\varphi^{(2)}_{,x}(1-\delta\varphi^{(2)})d^3x \tag{6.95}$$

which agrees with equation (2), so at least in this special case we confirm that 1PN terms in an expansion of Nordström's theory do not cause a violation of the SEP.

The next step would be to check the 2PN acceleration, where we do expect a violation. While the bulk of this calculation will be done in the future, we can note a few of the 2PN terms we will need to calculate. We will first need to define the so-called "superduperpotential" (see e.g. [87]) in order to solve (6.83):

$$Y_0^{(2)}(x,t) = -\int \rho^{*\prime} |x - x'|^3 d^3x' \tag{6.96}$$

such that:

$$\nabla^2 Y_0^{(2)} = 12\chi_0^{(2)} \tag{6.97}$$

Thus, solving (6.83) we find:

$$\delta\varphi^{(6)} = \frac{1}{2}\partial_t^2 \chi_0^{(4)} + \frac{1}{24}\partial_t^4 Y_0^{(2)} - 6\kappa \int \frac{(\rho^{*\prime})^2 \delta\varphi^{(2)\prime}}{|x - x'|} \tag{6.98}$$

Terms such as $\partial_t^4 Y_0^{(2)}$ will be fairly involved, although they should simplify to a large degree with the simplifications we have made.

Chapter 7

Conclusions

7.1 Summing Up and Outlook

The development of corotating spherical reference frames for use in numerical relativity has been a success. By combining these with the Weak Radiation Reaction (WRR) and Hydro-without-Hydro approximations we have been able to accurately and stably model binary inspirals in Nordström's second theory of gravitation. In fact, our simulation has also detected physical effects that we hadn't initially expected, thus further illustrating its usefulness.

There will always be surprises that occur during the process of fleshing out an idea. Corotating spherical coordinate systems were hypothesized to be good platforms in which to simulate the late inspiral of a compact body system. They single out the physical field excitations, provide a dense mesh where it is needed to resolve the stars, and give a smooth outer boundary for the outgoing waves. But, as to be expected, a range of technical complications arose during their implementation in code. For instance generating and using spherical harmonics in a fast and stable way is not trivial, and their adaptation to a parallel architecture takes some careful thought. A good bit of experimentation was also needed to settle on a stable and balanced technique to evolve the fields and sources forward in time.

One of the biggest surprises was that different components of the simulation would need very different amount of resources in order to converge to accurate values. In particular the volume integrals of field derivatives, used to find the accelerations of the stars, needed much higher resolutions to converge than other aspects of the simulation (when using standard second order finite differencing techniques). The use of analytical techniques in conjunction with our primary numerical ones allowed us to diagnose the problem, and solve it with higher order methods. Likewise the successful use analytic calculations to confirm the various results of the simulation gave us confidence that the code was working correctly when it produced behavior that we hadn't foreseen. This includes both the original Nordtvedt effect when we were using a simple linear scalar wave equation theory, and the violation of the Strong Equivalence Principle (SEP) at second post-Newtonian order in Nordström's theory.

As a quick intermediate project before we begin the application of our techniques to binary inspirals in general relativity, we would like to rigorously confirm that Nordström's theory does in fact violate the SEP at 2PN. We began this calculation in the previous chapter, including checking the behavior through the 1PN level, and looking at the fields that need to be evaluated for the 2PN level. As noted before we have a good amount of confidence that our conclusions will be born out: the expected behavior emerges when we either use a 1PN treatment of the system or let the compactness of the bodies M/R trend to zero, and furthermore we should expect a violation of the SEP at some point after 1PN level in Nordtröm's theory.

Our next and primary goal is to apply our computational framework to the binary inspiral problem in full general relativity. There will be a number of design choices that need to be made in order to adapt our work to this problem. We will almost certainly continue to use spherical coordinates, and choose some variation of the minimal distortion shift vector technique to keep the reference frame corotating in sync with compact bodies. It isn't clear at this point if we will then try to rewrite the ADM equations as to implement the WRR approximation. It worked well in Nordström's theory and we suspect it will in general relativity as well, but there are other compelling frameworks as well. Likewise we are not sure if we will use compact bodies as gravitational sources in conjunction with the Hydro-without-Hydro approximation, or if instead we will give in to the temptation to build a code that uses wormhole initial data and moving punctures for the evolution. The adaptation of the code to a parallel architecture may also necessitate changes to the way in which we divide up our grid. And no doubt there will be further surprises, which our experience with modeling inspirals in Nordström's theory will help us to deal with. We are confident that in the end our primary strategy for simulating binary inspirals in general relativity can be carried out, and will thus help to both extract the signals from the new detectors and test general relativity in the strong field limit.

REFERENCES

[1] C. Cutler and K. S. Thorne. An overview of gravitational-wave sources. *eprint arXiv:gr-qc/0204090*, (2002).

[2] A. Einstein. *Königlich Preussische Akademie der Wissenschaften Berlin, Sitzungsberichte*, 688, (1916).

[3] A. Einstein. *Königlich Preussische Akademie der Wissenschaften Berlin, Sitzungsberichte*, 154, (1918).

[4] S. Liberati, S. Sonego, and M. Visser. Faster-than-c signals, special relativity, and causality. *Annals Phys.*, 298:167–185, (2002).

[5] R. Wald. *General Relativity*. University of Chicago Press, Chicago, (1984).

[6] T. Damour. Gravitational radiation reaction in the binary pulsar and the quadrupole-formula controversy. *Phys. Rev. Lett.*, 51:1019, (1983).

[7] D. Kennefick. Controversies in the history of the radiation reaction problem in general relativity. (1997), gr-qc/9704002.

[8] K. S. Thorne. Gravitational waves. *Particle and Nuclear Astrophysics and Cosmology in the Next Millenium, Proceedings of the 1994 Snowmass Summer Study held 29 June - 14 July, 1994. Edited by E.W. Kolb and R.D. Peccei. Singapore: World Scientific, 1995., p.160*, (1995), gr-qc/9506086.

[9] K. S. Thorne. Gravitational radiation – a new window onto the universe. *eprint arXiv:gr-qc/9704042*, (1997).

[10] E. E. Flanagan and S. A. Hughes. The basics of gravitational wave theory. *New J. Phys.*, 7,204, (2005).

[11] C.W. Misner, K.S. Thorne, and J.A. Wheeler. *Gravitation*. Freeman: San Francisco, (1973).

[12] L. D. Landau and E. M. Lifschitz. *The Classical Theory of Fields*. Addison-Wesley, (1962).

[13] S. A. Hughes, S. Marka, P. L. Bender, and C. J. Hogan. Listening to the universe with gravitational-wave astronomy. *Prodeedings of the 2001 Snowmass Meeting*, (2001), astro-ph/0110349.

[14] E. E. Flanagan. Gravitation and relativity: At the turn of the millennium, 15th

international conference on general relativity and gravitation. *Inter-University Centre for Astronomy and Astrophysics*, (1998).

[15] S. L. Shapiro and S. A. Teukolsky. *Black Holes, White Dwarfs, and Neutron Stars*. John Wiley and Sons, Inc., (1983).

[16] A. A. Penzias and R. W. Wilson. A measurement of excess antenna temperature at 4080 mc/s. *Astrophys. J.*, 142:419–421, (1965).

[17] R. H. Dicke, P. J. E. Peebles, P. G. Roll, and D. T. Willkinson. Cosmic black-body radiation. *Astrophys. J.*, 142:414–419, (1965).

[18] J. Gallego, J. Zamorano, A. Aragon-Salamanca, and M. Rego. The current star formation rate of the local universe. *Astrophys. J. Lett.*, 455:L1, (1995).

[19] C. M. Baugh, S. Cole, C. S. Frenk, and C. G. Lacey. The epoch of galaxy formation. *Astrophys. J.*, 498:504, (1998).

[20] M. Schmidt. The rate of star formation. ii. the rate of formation of stars of different mass. *Astrophys. J.*, 137:758, (1963).

[21] P. Kroupa. On the variation of the initial mass function. *Mon. Not. Roy. Astro. Soc.*, 322:231–246, (2001).

[22] J. Frank, A. R. King, and D. Raine. *Accretion Power in Astrophysics 3rd Ed.* Cambridge University Press, (2002).

[23] M. C. R. D'Souza, P. M. Motl, J.E. Tohline, and J. Frank. Numerical simulations of the onset and stability of mass transfer in binaries. *Astrophys. J.*, 633:381, (2006).

[24] G. Giuricin, F. Mardirossian, and M. Mezzetti. General properties of algol binaries. *Astrophys. J. Supp. Ser.*, 52:35, (1983).

[25] C. T. Bolton. Identification of cygnus x-1 with hde 226868. *Nature*, 235:271–273, (1972).

[26] S. L. Shapiro, A. P. Lightman, and D. M. Eardley. A two-temperature accretion disk model for cygnus x-1 - structure and spectrum. *Astrophys. J.*, 204:187, (1976).

[27] J. R. Dickel, W. J. M. van Breugel, and R. G. Strom. Radio structure of the remnant of tycho's supernova (sn 1572). *Astronom. J.*, 101:2151–2159, (1991).

[28] J. Faulkner, B. P. Flannery, and B. Warner. Ultrashort-period binaries. ii. hz 29 (=am cvn): a double-white semidetached postcataclysmic nova? *Astrophys. J.*, 175:L79, (1972).

[29] K. A. Postnov and L. R. Yungelson. The evolution of compact binary star systems. *Living Rev. Relativity 9, (2006), 6. URL (cited on 5/21/07): http://www.livingreviews.org/lrr-2006-6*, (2006).

[30] G. Nelemans. Am cvn stars. *Proceedings of ASP Conference Vol. 330. Edited by J.-M. Hameury and J.-P. Lasota. San Francisco: Astronomical Society of the Pacific*, page 27, (2005).

[31] J. M. Weisberg and J. H. Taylor. The relativistic binary pulsar b1913+16: Thirty years of observations and analysis. *Binary Radio Pulsars, ASP Conference Series*, 328, (2005).

[32] E. S. Phinney. The rate of neutron star binary mergers in the universe: Minimal predictions for gravity wave detectors. *Astrophys. J. Lett.*, 380:L17–L21, (1991).

[33] M. Burgay, N. D'Amico, A. Possenti, R. N. Manchester, A. G. Lyne, B. C. Joshi, M. A. McLaughlin, M. Kramer, J. M. Sarkissian, F. Camilo, V. Kalogera, C. Kim, and D. R. Lorimer. An increased estimate of the merger rate of double neutron stars from observations of a highly relativistic system. *Nature*, 426:531–533, (2003).

[34] A. J. Faulkner, M. Kramer, A. G. Lyne, R. N. Manchester, M. A. McLaughlin, I. H. Stairs, G. Hobbs, A. Possenti, D. R. Lorimer, N. D'Amico, F. Camilo, and M. Burgay. Psr j1756-2251: A new relativistic double neutron star system. *Astrophys. J.*, 618:L119–L122, (2005).

[35] R. Narayan, B. Paczynski, and T. Piran. Gamma-ray bursts as the death throes of massive binary stars. *Astrophys. J.*, 395:L83, (1992).

[36] T. Piran. The physics of gamma-ray bursts. *Rev. Mod. Phys.*, 76:1143, (2005).

[37] W. H. Lee, E. Ramirez-Ruiz, and J. Granot. A compact binary merger model for the short, hard grb050509b. *Astrophys. J.*, 630:L165–L168, (2005).

[38] K. et. al. Hurley. An exceptionally bright flare from sgr1806-20 and the origins of short-duration gamma-ray bursts. *Nature*, 434:1098, (2005).

[39] S. F. Portegies Zwart and S. L. W. McMillan. Black hole mergers in the universe. *Astrophys. J.*, 528:L17–L20, (2000), astro-ph/9910061.

[40] C. R. Evans, I. Jr. Iben, and L. Smarr. Degenerate dwarf binaries as promising, detectable sources of gravitational radiation. *Astrophysical Journal*, 323:129, (1987).

[41] M. B. Davies, H. Ritter, and A. King. Formation of the binary pulsars j11416545 and b2303+46. *Mon. Not. R. Astron. Soc.*, 335:369–376, (2002).

[42] D. Merritt. Dynamics of galaxy cores and supermassive black holes. *Rep. Prog. Phys.*, 69:2513–2579, (2006).

[43] C. L. Fryer and Warren M. S. Modeling core-collapse supernovae in three dimensions. *Astrophys. J.*, 574:L65, (2002).

[44] C. L. Fryer, D. E. Holz, and S. A. Hughes. Gravitational wave emission from core collapse of massive stars. *Astrophys. J.*, 565:430, (2002).

[45] L. Bildsten. *Astrophys. J. Lett.*, 501:L89, (1998).

[46] G. Ushomirsky, C. Cutler, and L. Bildsten. *Mon. Not. Roy. Astron. Soc.*, 319:902, (2000).

[47] N. J. Cornish. Detecting a stochastic gravitational wave background with the laser interferometer space antenna. *Phys. Rev. D*, 65:022004, (2001).

[48] J. Weber. Evidence for discovery of gravitational radiation. *Phys. Rev. Lett.*, 22:1320, (1972).

[49] J. P. Zendri. *Gravitational Waves, Third Edoardo Amaldi Conf ed S Meshkov (Melville, NY: AIP)*, pages 421–2, (2000).

[50] N. A. Robertson. Laser interferometric gravitational wave detectors. *Class. Quant. Grav.*, 17:R19, (2000).

[51] P. R. Saulson. *Fundamentals of Interferometric Gravitational Wave Detectors*. World Scientific Publishers Singapore, (1994).

[52] R. Weiss. Electromagnetically coupled broadband gravitational antenna. *Quart. Progr. Rep.*, 105, 54, (1972).

[53] R. L. Forward. Wideband laser-interferometer graviational-radiation experiment. *Phys. Rev. D*, 17:379–390, (1978).

[54] Abramovici et al. *Science*, 256:325, (1992).

[55] Bradaschia et al. *Nucl. Instrum. Methods A*, 289:518, (1990).

[56] B. Willke and et. al. The geo 600 gravitational wave detector. *Class. Quantum Grav.*, 19:1377–1387, (2002).

[57] K. Kawabe and TAMA collaboration. Status of tama project. *Class. Quantum Grav.*, 14:1477–1480, (1997).

[58] P. Fritschel. Second generation instruments for the laser interferometer gravitational wave observatory (ligo). *Gravitational-Wave Detection. Edited by Cruise, Mike; Saulson, Peter. Proceedings of the SPIE*, 4856:282–291, (2003).

[59] K. Danzmann and et al. Lisa: Laser interferometer space antenna for gravitational wave measurements. *Class. Quantum Grav.*, 13:A247–A250, (1996).

[60] R. W. P. J. Drever, J. L. Hall, F. V. Kowalski, J. Hough, G.M. Ford, A. J. Munley, and H. Ward. Laser phase and frequency stabilization using an optical resonator. *Appl. Phys. B*, 31:97, (1983).

[61] A. Buonanno and Y. Chen. Quantum noise in second generation, signal-recycled laser interferometric gravitational-wave detectors. *Phys. Rev. D*, 64:042006, (2001).

[62] A. Buonanno and Y. Chen. Optical noise correlations and beating the standard quantum limit in advanced gravitational-wave detectors. *Class. Quantum Grav.*, 18:L95, (2001).

[63] K.D Skeldon, K. A. Strain, A. I. Grant, and J. Hough. Test of an 18-m-long suspended modecleaner cavity. *Rev. Sci. Instrum.*, 67:2443, (1996).

[64] S. A. Hughes and K. S. Thorne. Seismic gravity-gradient noise in interferometric gravitational-wave detectors. *Phys. Rev. D*, 58:122002, (1998).

[65] K. S. Thorne and C. J. Winstein. Human gravity-gradient noise in interferometric gravitational-wave detectors. *Phys. Rev. D*, 60:082001, (1999).

[66] Y. Levin. Internal thermal noise in the ligo test masses: A direct approach. *Phys. Rev. D*, 57:659–663, (1998).

[67] Y. T. Liu and K. S. Thorne. Thermoelastic noise and homogeneous thermal noise in finite sized gravitational-wave test masses. *Phys. Rev. D*, 62:122002, (2000).

[68] D. H. Santamore and Y. Levin. Eliminating thermal violin spikes from ligo noise. *Phys. Rev. D*, 64:042002, (2001).

[69] P. R. Saulson. Thermal noise in mechanical experiments. *Phys. Rev. D*, 42:2437, (1990).

[70] C. W. Helstrom. *Statistical Theory of Signal Detection, 2nd ed.* Permagon, London, (1968).

[71] B. J. Owen and B. S. Sathyaprakash. Matched filtering of gravitational waves from inspiraling compact binaries: Computational cost and template placement. *Phys. Rev. D*, 60:022002, (1999).

[72] B. Allen, W. G. Anderson, P. R. Brady, D. A. Brown, and J. D. E. Creighton. Findchirp: an algorithm for detection of gravitational waves from inspiraling compact binaries. (2005), gr-qc/0509116.

[73] V. M. Lipunov, K. A. Postnov, and M. E. Prokhorov. First ligo events: binary black hole mergings. *New Astronomy*, 2:43–52, (1997), astro-ph/9610016.

[74] E. E. Flanagan and S. A. Hughes. Measuring gravitational waves from binary black hole coalescences. ii. signal to noise for inspiral, merger, and ringdown. *Phys. Rev. D*, 57:4535, (1998).

[75] E. E. Flanagan and S. A. Hughes. Measuring gravitational waves from binary black hole coalescences. ii. the waves information and its extraction, with and without templates. *Phys. Rev. D*, 57:4566, (1998).

[76] R. H. Price and J. Pullin. Colliding black holes: The close limit. *Phys. Rev. Lett.*, 72:3297–3300, (1994).

[77] J. G. Baker, B. Brügmann, M. Campanelli, C. O. Lousto, and R. Takahashi. Plunge waveforms from inspiralling binary black holes. *Phys. Rev. Lett.*, 87:121103, (2001).

[78] A. Einstein. Explanation of the perihelion motion of mercury from the general theory of relativity. *Sitzungber. Preuss. Akad. Wiss.*, 1915:831–839, (1915).

[79] H. A. Lorentz and J. Droste. The motion of a system of bodies under the influence of their mutual attraction, according to einsteins theory. *The Collected Papers of H.A. Lorentz, Vol. 5, 330355, (Nijhoff, The Hague, Netherlands, 1937).*

[80] A. Einstein, L. Infeld, and B. Hoffmann. The gravitational equations and the problem of motion. *Ann. Math.*, 39:65–100, (1938).

[81] S. Chandrasekhar. The post-newtonian equations of hydrodynamics in general relativity. *Astrophyical Journal*, 142:1488–1540, (1965).

[82] S. Chandrasekhar. Conservation laws in general relativity and in the post-newtonian approximations. *Astrophyical Journal*, 158:45, (1969).

[83] S. Chandrasekhar and Y. Nutku. The second post-newtonian equations of hydrodynamics in general relativity. *Astrophyical Journal*, 158:55–79, (1969).

[84] S. Chandrasekhar and F. P. Esposito. The 2 1/2 post-newtonian equations of hydrodynamics and radiation reaction in general relativity. *Astrophyical Journal*, 160:153–179, (1970).

[85] P. C. Peters and J. Mathews. Gravitational radiation from point masses in a keplerian orbit. *Phys. Rev. 131,435*, (1963).

[86] P. C. Peters. Gravitational radiation and the motion of two point masses. *Phys. Rev. 136,1224*, (1964).

[87] T. Mitchell and C. M. Will. Post-newtonian gravitational radiation and equations of motion via direct integration of the relaxed einstein equations. v. the strong equivalence principle to second post-newtonian order. *Phys. Rev. D*, (2007).

[88] C. M. Will. *Theory and Experiment in Gravitational Physics Revised Edition*. Cambridge University Press, (1993).

[89] T.W. Baumgarte, S.A. Hughes, and S.L. Shapiro. Evolving einstein's field equations with matter: The "hydro without hydro" test. *Phys. Rev. D*, 60:087501, (1999),gr-qc/9902024.

[90] S. Hahn and R. Lindquist. The two-body problem in geometrodynamics. *Annals of Physics*, 29:304, (1964).

[91] L. Smarr. *Sources of Gravitational Radiation*. Cambridge University Press, (1979).

[92] K. Eppley. *Phys. Rev. D*, 16:1609, (1975).

[93] J. Wilson. *in Sources of Gravitational Radiation*. Cambridge University Press, (1979).

[94] M. W. Choptuik. Universality and scaling in gravitational collapse of a massless scalar field. *Phys. Rev. Lett.*, 70:9, (1993).

[95] A. M. Abrahams and C. R. Evans. Critical behavior and scaling in vacuum axisymmetric gravitational collapse. *Phys. Rev. Lett.*, 70:2980, (1993).

[96] B. K. Berger. Numerical approaches to spacetime singularities. *Living Rev. Relativity 5, (2002), 1. URL (cited on 6-17-07): http://www.livingreviews.org/lrr-2002-1*, (2002).

[97] M. Shibata, K. Taniguchi, and K. Uryu. Merger of binary neutron stars of unequal mass in full general relativity. *Phys. Rev. D*, 68:084020, (2003).

[98] L. Lehner. Numerical relativity: A review. *Class. Quantum Grav.*, 18:R25–R86, (2001).

[99] T. W. Baumgarte and S. L. Shapiro. Numerical relativity and compact binaries. *Physics Reports*, 376:41–131, (2003), gr-qc/0211028.

[100] S. L. Shapiro. Numerical relativity at the frontier. *Progress of Theoretical Physics Supplement*, 163:100–119, (2005), gr-qc/0509094.

[101] M. Alcubierre. The status of numerical relativity. *arXiv:gr-qc/0412019v1*, (2004), gr-qc/0509116.

[102] G. B. Cook. Initial data for numerical relativity. *Living Rev. Relativity 3, (2000), 5. URL (cited on 5-23-07): http://www.livingreviews.org/lrr-2000-5*, (2000).

[103] J. M. Marti and E. Müller. Numerical hydrodynamics in special relativity. *"Numerical Hydrodynamics in Special Relativity", Living Rev. Relativity 6, (2003), 7. URL (cited on 5-23-07): http://www.livingreviews.org/lrr-2003-7*, (2003).

[104] J. A. Font. Numerical hydrodynamics in general relativity. *"Numerical Hydrodynamics in General Relativity", Living Rev. Relativity 6, (2003), 4. URL (cited on 5-23-07): http://www.livingreviews.org/lrr-2003-4*, (2003).

[105] F. A. Rasio and S. L. Shapiro. Coalescing binary neutron stars. *Class. Quantum Grav.*, 16:R1–R29, (1999).

[106] O. A. Reula. Hyperbolic methods for einstein's equations. *"Hyperbolic Methods for Einstein's Equations", Living Rev. Relativity 1, (1998), 3. URL (cited on 5-23-07): http://www.livingreviews.org/lrr-1998-3*, (1998).

[107] R. Arnowitt, S. Deser, and C. W. Misner. The dynamics of general relativity. *in "Gravitation: An Introduction to Current Research" ed. L. Witten (Wiley, New York)*, pages 227–265, (1962).

[108] C. R. Evans. Method for numerical relativity: simulation of axisymmetric gravitational collapse and gravitational radiation generation. *Dissertation*, (1984).

[109] J. W. York, Jr. *in Sources of Gravitational Radiation.* Cambridge University Press, (1979).

[110] Y. Choquet-Bruhat and J. York. *The Cauchy Problem.* Plenum, New York, (1998).

[111] D. S. Brill and R. W. Lindquist. Interaction energy in geometrostatics. *Phys. Rev.*, 131:471–476, (1963).

[112] S. Brandt and B. Brügmann. A simple construction of initial data for multiple black holes. *Phys. Rev. Lett.*, 78:3606–3609, (1997).

[113] A. Lichnerowicz. *J. Math. Pure Appl.*, 23:37, (1944).

[114] J. W. York, Jr. *Phys. Rev. Lett.*, 26:1656, (1971).

[115] J. W. York, Jr. *Phys. Rev. Lett.*, 28:1082, (1972).

[116] M. Hannam, C. R. Evans, G. B. Cook, and T. W. Baumgarte. Can a combination of the conformal thin-sandwich and puncture methods yield binary black hole solutions in quasiequilibrium? *Phys. Rev. D*, 68:064003, (2003).

[117] F. Pretorius. Evolution of binary black hole spacetimes. *Phys.Rev.Lett.*, 95:121101, (2005), gr-qc/0507014.

[118] F. Pretorius. Simulation of binary black hole spacetimes with a harmonic evolution scheme. *Class. Quant. Grav.*, 23:S529–S552, (2006), gr-qc/0602115.

[119] T. Nakamura, K. Oohara, and Y. Kojima. General relativistic collapse to black holes and gravitational waves from black holes. *Prog. Theor. Phys. Suppl.*, 90:1, (1987).

[120] M. Shibata and T. Nakamura. *Phys. Rev. D*, 52:5428, (1995).

[121] T. W. Baumgarte and S. L. Shapiro. On the numerical integration of einstein's field equations. *Phys. Rev. D*, 59:024007, (1999), gr-qc/9810065.

[122] B. Imbiriba, J. G. Baker, D. Choi, J. Centrella, D. R. Fiske, J. D. Brown, J. R. van Meter, and K. Olson. Evolving a puncture black hole with fixed mesh refinement. *Phys. Rev. D.*, 70:124025, (2004).

[123] B. Riemann and B. Brügmann. Maximal slicing for puncture evolutions of schwarzschild and reissner-nordström black holes. *Phys. Rev. D*, 69:044006, (2004).

[124] P.R. Brady, J.D.E. Creighton, and K.S. Thorne. Computing the merger of black-hole binaries: the ibbh problem. *Phys. Rev. D.*, 58:061501, (1998),gr-qc/9804057.

[125] B. Brügmann, W. Tichy, and N Jansen. Numerical simulation of orbiting black holes. *Phys. Rev. Lett.*, 92:211101, (2004).

[126] M. Alcubierre, B. Brügmann, P. Diener, F. S. Guzmn, I. Hawke, S. Hawley, F. Herrmann, M. Koppitz, D. Pollney, E. Seidel, and J. Thornburg. Dynamical evolution of quasicircular binary black hole data. *Phys. Rev.*, D72:044004, (2005), gr-qc/0411149.

[127] B. Brügmann. Binary black hole mergers in 3d numerical relativity. *Int. J. Mod. Phys. D*, 8:85, (1999).

[128] M. Alcubierre, W. Benger, B. Brügmann, G. Lanfermann, L. Nerger, E. Seidel, and R. Takahashi. 3d grazing collision of two black holes. *Phys. Rev. Lett.*, 87:271103, (2001).

[129] M. Campanelli, C. O. Lousto, P. Marronetti, and Y. Zlochower. Accurate evolutions of orbiting black-hole binaries without excision. *Phys. Rev. Lett.*, 96:111101, (2006), gr-qc/0511048.

[130] J. G. Baker, J. Centrella, D. I. Choi, M. Koppitz, and J. van Meter. Gravitational wave extraction from an inspiraling configuration of merging black holes. *Phys. Rev. Lett.*, 96:111102, (2006), gr-qc/0511103.

[131] M. Hannam, S. Husa, D. Pollney, B. Brügmann, and N. O'Murchadha. Geometry and regularity of moving punctures. *eprint arXiv:gr-qc/0606099*, (2006).

[132] M. Hannam, S. Husa, B. Brügmann, J. A. Gonzlez, U. Sperhake, and N. Ó. Murchadha. Where do moving punctures go? *Journal of Physics: Conference Series*, 66:012047, (2007).

[133] C. Bona, J. Massó, E. Seidel, and J. Stela. New formalism for numerical relativity. *Phys. Rev. D*, 56:3405–3415, (1997).

[134] M. Alcubierre, B. Brügmann, P. Diener, M. Koppitz, D. Pollney, E. Seidel, and R. Takahashi. Gauge conditions for long-term numerical black hole evolutions without excision. *Phys. Rev.*, D67:084023, (2003).

[135] J. D. Brown and L. L. Lowe. Multigrid elliptic equation solver with adaptive mesh refinement. *J. Comp. Phys.*, 209:582–598, (2005).

[136] R. A. Hulse and J. H. Taylor. Discovery of a pulsar in a binary system. *Astrophysical Journal 195,L51.*

[137] W. T. Ni. Theoretical frameworks for testing relativistic gravity. iv. a compendium of metric theories of gravity and their post-newtonian limits. *Astrophysical Journal 176:769-796*, 1972.

[138] K. Nordtvedt. Testing relativity with laser ranging to the moon. *Phys. Rev.*, 170:1186–1187, 1968.

[139] A. G. Wiseman. The central density of neutron stars in close binaries. *Phys. Rev. Lett.*, 79,1189-1192, (1997), gr-qc/9704018.

[140] S. A. Hughes. Trust but verify: The case for astrophysical black holes. (2005), hep-ph/0511217.

[141] Baker J. G., M. Campanelli, F. Pretorius, and Y. Zlochower. Comparisons of binary black hole merger waveforms. (2007), gr-qc/0701016.

[142] J. G. Baker, J. R. van Meter, S. T. McWilliams, J. Centrella, and B. J. Kelly. Consistency of post-newtonian waveforms with numerical relativity. (2006), gr-qc/0612024.

[143] T. Baumgarte, P. Brady, J. D. E. Creighton, L. Lehner, Pretorius F., and DeVoe R. Learning about compact binary merger: the interplay between numerical relativity and gravitational-wave astronomy. (2006), gr-qc/0612100.

[144] S. L. Shapiro and S. A. Teukolsky. Scalar gravitation: A laboratory for numerical relativity. *Phys. Rev. D*, 47:1529, 1993.

[145] K. Watt and C. W. Misner. Relativistic scalar gravity: A laboratory for numerical relativity. (1999),gr-qc/9910032.

[146] W. H. Press, S. A. Teukolsky, Vetterling W. T., and B. P. Flannery. *Numerical Recipes in C 2nd Ed.* Cambridge University Press, (1992).

[147] J. P. Boyd. *Chebyshev and Fourier Spectral Methods 2nd Ed.* Dover, (2001).

[148] H. A. Buchdahl. General relativistic fluid spheres. *Phys. Rev.*, 116:1027–1034, (1959).

[149] H. Bondi. Massive spheres in general relativity. *Proc. R. Soc. London*, 282:303, (1964).

[150] M. Abramowitz and I. A. Stegun. National Bureau of Standards, Washington, DC, (1972).

[151] J. R. Dricoll and D. M. Jr. Healy. Computing fourier transforms and convolutions on the 2-sphere. *Advan. App. Math,*, 15:202–250, (1994).

[152] B. K. Alpert and V. Rokhlin. A fast algorithm for the evaluation of legendre expansions. *SIAM J. Sci. Stat. Comp.*, 12:158–179, (1991).

[153] D. M. Jr. Healy, D. N. Rockmore, P. J. Kostelec, and S. Moore. Ffts for the 2-sphere-improvements and variations. *J. Four. An. App.*, 9:341–385, (2003).

[154] L. Bildsten and C. Cutler. Tidal interactions of inspiraling compact binaries. *Astrophys. J.*, 400:175, (1992).